공학박사학위논문

인공신경망을 이용한 아격자스케일 응력 모델링과 난류 채널 및 후향 계단 유동에의 적용

Modeling of the subgrid-scale stress with a neural network and its application to turbulent channel and backward-facing-step flows

2021 년 8 월

서울대학교 대학원

기계항공공학부

박 종 환

인공신경망을 이용한 아격자스케일 응력 모델링과 난류 채널 및 후향 계단 유동에의 적용

Modeling of the subgrid-scale stress with a neural network and its application to turbulent channel and backward-facing-step flows

지도교수 최 해 천

이 논문을 공학박사 학위논문으로 제출함

2021년 4월

서울대학교 대학원
기계항공공학부
박 종 환

박종환의 공학박사 학위논문을 인준함

2021년 6월

위 원 장 : 박 형 민

부위원장 : 최 해 천

위 원 : 황 원 태

위 원 : 이 창 훈

위 원 : 이 정 일

Modeling of the subgrid-scale stress with a neural network and its application to turbulent channel and backward-facing-step flows

Jonghwan Park
Department of Mechanical & Aerospace Engineering
Seoul National University

Abstract

A fully-connected neural network (NN) is used to develop a subgrid-scale model which maps the relation between the subgrid-scale stress and filtered flow variable in a turbulent channel (Part I) and backward-facing-step (Part II) flows.

For turbulent channel flow, DNS (direct numerical simulation) database of $Re_\tau = 178$ is used to develop an NN-based subgrid-scale (SGS) model, and *a priori* and *a posteriori* tests are performed to investigate its prediction performance. In *a priori* test, an NN-based SGS model with the input of filtered velocity gradient or strain rate tensor at multiple grid points provides high correlation coefficients between the true and predicted SGS stresses. However, this model provides an unstable solution in *a posteriori* test, as the model produces a non-negligible backscatter which is known to induce numerical instability in large eddy simulation (LES). To ensure a stable LES solution with this model, a special treatment like backscatter clipping is required. On the other hand, an NN-based SGS model with the input of filtered strain rate tensor at a single grid point shows an excellent prediction performance for the mean velocity and Reynolds shear stress in *a posteriori* test, although it gives low correlation coefficients be-

tween the true and predicted SGS stresses in *a priori* test. This NN-based SGS model trained at $Re_\tau = 178$ is applied to a turbulent channel flow at $Re_\tau = 723$ using the same grid resolution in wall units, providing fairly good agreements of the solutions with the filtered DNS data. When the grid resolution in wall units is different from that of trained data, this NN-based SGS model does not perform well. This is overcome by training an NN with the datasets having two filters whose sizes are larger and smaller than the grid size in large eddy simulation.

For turbulent flow over a backward-facing step (BFS), an NN-based SGS model is developed with the filtered DNS data at $Re_h = 5100$. Two input variables, the filtered strain rate and velocity gradient tensors at a single grid point, respectively, are adopted, where the NN-based SGS models with these inputs provide a stable LES solution in the turbulent channel flow without any special treatment. In the LES at $Re_h = 5100$, those NN-based SGS models show similar performance, and provide good predictions for the reattachment length and root-mean-square velocity fluctuations. Then, we assess the performance of the NN-based SGS model with the input of filtered strain rate tensor for the LES at $Re_h = 24000$, and this model provides fairly good results, compared to those from the LES with dynamic Smagorinsky model (DSM). Finally, we apply this model for LES of controlled BFS flow with multiple taps installed at the step edge. LES with this NN-based SGS model predicts the amount of reduction in the reattachment length better than by LES with DSM, showing that the NN-based model trained with uncontrolled BFS flow maintains its prediction performance in LES of controlled BFS flow.

Keywords: Large eddy simulation, subgrid-scale modeling, machine learning, neural network, turbulent channel flow, backward facing step flow

Student number: 2015-20699

Contents

List of Figures

Part I Modeling of the subgrid-scale stress with a neural network: application to turbulent channel flow

Appendix A

List of Tables

Part I Modeling of the subgrid-scale stress with a neural network: application to turbulent channel flow

Part I.

Modeling of the subgrid-scale stress with a neural network: application to turbulent channel flow

This part is based on "**Park, J.**, & Choi, H. 2021 Toward neural-network-based large eddy simulation: application to turbulent channel flow. *J. Fluid Mech.* **914**, A16".

Chapter 1

Introduction

In large eddy simulation (LES), the effect of the subgrid-scale (SGS) velocity fluctuations on the resolved one should be modeled, and thus the aim of SGS modeling is to find the relations between the resolved flow variables and SGS stresses. A conventional approach for SGS modeling is to approximate the SGS stresses with the resolved flow variables in an arithmetic form based on turbulence theory and hypothesis. For example, an eddy viscosity model is based on the Boussinesq hypothesis that linearly relates the SGS stress tensor $\boldsymbol{\tau}$ with the resolved strain rate tensor $\bar{\boldsymbol{S}}$, i.e., $\boldsymbol{\tau} - \frac{1}{3}\mathrm{tr}\,(\boldsymbol{\tau})\,\boldsymbol{I} = -2\nu_t\bar{\boldsymbol{S}}$, where $\boldsymbol{I}$ is the identity tensor, and ν_t is an eddy viscosity to be modeled with the resolved flow variables (see, for example, Smagorinsky 1963; Nicoud & Ducros 1999; Vreman 2004; Nicoud *et al.* 2011; Verstappen 2011; Rozema *et al.* 2015; Trias *et al.* 2015; Silvis *et al.* 2017). Some models dynamically determine the coefficients of the eddy viscosity models (Germano *et al.* 1991; Lilly 1992; Ghosal *et al.* 1995; Piomelli & Liu 1995; Meneveau *et al.* 1996; Park *et al.* 2006; You & Moin 2007; Lee *et al.* 2010; Verstappen *et al.* 2010). Other types of SGS model include the similarity model (Bardina *et al.* 1980; Liu *et al.* 1994; Domaradzki & Saiki 1997),

the mixed model (Bardina *et al.* 1980; Zang *et al.* 1993; Vreman *et al.* 1994; Liu *et al.* 1994, 1995; Salvetti & Banerjee 1995; Horiuti 1997; Akhavan *et al.* 2000), and the gradient model (Clark *et al.* 1979; Liu *et al.* 1994). These models have been successfully applied to various turbulent flows, but there are still drawbacks to overcome. For example, the eddy viscosity model always produces either the wrong SGS stresses or the wrong energy spectrum Jiménez & Moser (2000). In addition, the eddy viscosity model is purely dissipative, and thus the energy transfer from subgrid to resolved scales (i.e., backscatter) cannot be predicted. On the other hand, the scale similarity model provides the backscatter but does not dissipate energy sufficiently, and thus simulations often diverge or produce inaccurate results. Therefore, an additional eddy-viscosity term is introduced and usually coupled with the scale similarity model to properly dissipate the energy (Bardina *et al.* 1980; Liu *et al.* 1994; Langford & Moser 1999; Sarghini *et al.* 1999; Meneveau & Katz 2000; Anderson & Domaradzki 2012). The dynamic version of the eddy viscosity model can predict local backscatter with negative ν_t, but an averaging procedure or *ad hoc* clipping on negative ν_t is required in actual LES to avoid numerical instability (Germano *et al.* 1991; Lilly 1992; Ghosal *et al.* 1995; Meneveau *et al.* 1996; Park *et al.* 2006; Thiry & Winckelmans 2016).

An alternative approach for SGS modeling is to use high-fidelity DNS (direct numerical simulation) data. The optimal LES (Langford & Moser 1999; Völker, Moser & Venugopal 2002; Langford & Moser 2004; Zandonade, Langford & Moser 2004; Moser *et al.* 2009), based on the stochastic estimation (Adrian *et al.* 1989; Adrian 1990), is such an approach, where a prediction target, e.g., the SGS force (divergence of the SGS stress tensor), is expanded with input variables (velocity and velocity gradients). The coefficients of the input variables are found by minimizing the mean-squared error between the true and estimated values of the prediction target. Another example is to use a machine-learning algorithm

such as the fully connected neural network (FCNN). The FCNN is a nonlinear function that maps the predefined input variables and prediction target, where the target can be the SGS stresses or SGS force. Like the optimal LES, the weight parameters of the FCNN are found by minimizing a given loss function such as the mean-squared error. In the case of two-dimensional decaying isotropic turbulence, Maulik *et al.* (2018) applied an FCNN-based approximate deconvolution model (Stolz & Adams 1999; Maulik & San 2017) to LES, where the filtered vorticity and streamfunction at multiple grid points were the inputs of FCNNs and the corresponding prediction targets were the deconvolved vorticity and streamfunction, respectively. This FCNN-based LES showed a better prediction of the kinetic energy spectrum than LES with the dynamic Smagorinsky model (DSM, Germano *et al.* 1991; Lilly 1992). Maulik *et al.* (2019) used the same input together with eddy-viscosity kernels, but had the SGS force as the target. In *a posteriori* test, this FCNN model reasonably predicted the kinetic energy spectrum even though the prediction performance was not much better than those of the Smagorinsky and Leith models (Leith 1968) with the model coefficients of $C_s = 0.1 - 0.3$ in $\nu_t = (C_s\bar{\Delta})^2|\bar{S}|$, where $\bar{\Delta}$ is the grid spacing and $|\bar{S}| = \sqrt{2\bar{S}_{ij}\bar{S}_{ij}}$. Pawar *et al.* (2020) trained an FCNN to predict SGS stress directly with the inputs of $\bar{\boldsymbol{u}}$, $\nabla\bar{\boldsymbol{u}}$, and $\nabla^2\bar{\boldsymbol{u}}$, where $\bar{\boldsymbol{u}}$ is the filtered velocity. They only conducted *a priori* test, and showed that using inputs at multiple grid points provided better prediction performance for SGS stresses than using inputs at a point. In the case of three-dimensional forced isotropic turbulence, Vollant *et al.* (2017) used an FCNN with the target of the SGS scalar flux divergence $\nabla\cdot\left(\overline{\boldsymbol{u}\phi} - \bar{\boldsymbol{u}}\bar{\phi}\right)$ and the input of $\bar{\boldsymbol{S}}$, where $\bar{\phi}$ is the filtered passive scalar. They showed that the results from FCNN-based LES were very close to those from the filtered DNS. Zhou *et al.* (2019) reported that using the filter size as well as the velocity gradient tensor as the input variables was beneficial to predict

the SGS stresses for the flow having a filter size different from that of trained data. Xie *et al.* (2020*a*) used an FCNN to predict the SGS force with the input of $\nabla\bar{\boldsymbol{u}}$ at multiple grid points, and this FCNN performed better than DSM for the prediction of energy spectrum. In the case of three-dimensional decaying isotropic turbulence, Wang *et al.* (2018) adopted the velocity and its first and second derivatives for the input of FCNN to predict the SGS stresses, and showed better performance in *a posteriori* test than that of DSM. Beck *et al.* (2019) used a convolutional neural network (CNN) to predict the SGS force with the input of the velocity in whole domain, and showed in *a priori* test that the CNN-based SGS model predicted the SGS force better than an FCNN-based SGS model did. In the case of compressible isotropic turbulence, Xie *et al.* (2019*a*) used FCNNs to predict SGS force and divergence of SGS heat flux, respectively, with the inputs of $\nabla\tilde{\boldsymbol{u}}$, $\nabla^2\tilde{\boldsymbol{u}}$, $\nabla\tilde{T}$, $\nabla^2\tilde{T}$, $\bar{\rho}$, and $\nabla\bar{\rho}$ at multiple grid points, where ρ is the fluid density, and $\tilde{\boldsymbol{u}}$ and $\tilde{T}$ are the mass-weighting-filtered velocity and temperature, respectively. Xie *et al.* (2019*b*) applied FCNNs to predict the coefficients of a mixed model with the inputs of $|\tilde{\boldsymbol{\omega}}|$, $\tilde{\theta}$, $\sqrt{\tilde{\alpha}_{ij}\tilde{\alpha}_{ij}}$, $\sqrt{\tilde{S}_{ij}\tilde{S}_{ij}}$, $|\nabla\tilde{T}|$, where $|\tilde{\boldsymbol{\omega}}|$, $\tilde{\theta}$, $\tilde{\alpha}_{ij}$, and $\tilde{S}_{ij}$ are the mass-weighting-filtered vorticity magnitude, velocity divergence, velocity gradient tensor, and strain rate tensor, respectively. Xie *et al.* (2019*c*) trained FCNNs with $\nabla\tilde{\boldsymbol{u}}$, $\nabla^2\tilde{\boldsymbol{u}}$, $\nabla\tilde{T}$, and $\nabla^2\tilde{T}$ at multiple grid points as the inputs to predict SGS stresses and SGS heat flux, respectively. Xie *et al.* (2020*c*) used FCNNs to predict SGS stresses and SGS heat flux with the inputs of $\nabla\tilde{\boldsymbol{u}}$, $\nabla\hat{\tilde{\boldsymbol{u}}}$, $\nabla\tilde{T}$, and $\nabla\hat{\tilde{T}}$ at multiple grid points, where the filter size of $\hat{\Delta}$ is twice that of $\tilde{\Delta}$. They (Xie *et al.* 2019*a*,*b*,*c*, 2020*c*) showed that the FCNN-based LES provided more accurate kinetic energy spectrum and structure function of the velocity than those based on DSM and dynamic mixed model.

Unlike for isotropic turbulence, the progress in LES with an FCNN-based SGS model has been relatively slow for turbulent channel flow. Sarghini, de Fe-

lice & Santini (2003) trained an FCNN with the input of filtered velocity gradient and $\bar{u}_i'\bar{u}_j'$ to predict the model coefficient of the Smagorinsky model for a turbulent channel flow, where $\bar{u}_i'$ is the instantaneous filtered velocity fluctuations. Pal (2019) trained an FCNN to predict ν_t in the eddy viscosity model with the input of filtered velocity and strain rate tensor. In Sarghini *et al.* (2003) and Pal (2019), however, FCNNs were trained by LES data from traditional SGS models, i.e., mixed model (Bardina *et al.* 1980) and DSM, respectively, rather than by filtered DNS data. Wollblad & Davidson (2008) trained an FCNN with filtered DNS data to predict the coefficients of the truncated POD (proper orthogonal decomposition) expansion of the SGS stresses with the input of $\bar{u}_i'$, wall-normal gradient of $\bar{u}_i'$, filtered pressure ($\bar{p}$), and wall-normal and spanwise gradients of $\bar{p}$. They showed from *a priori* test that the predicted SGS stresses were in good agreements with those from filtered DNS data. However, the FCNN alone was unstable in *a posteriori* test, and thus the FCNN combined with the Smagorinsky model was used to conduct LES, i.e., $\tau_{ij} = c_b\tau_{ij}^{\mathrm{FCNN}} + (1 - c_b)\tau_{ij}^{\mathrm{Smag}}$, where $\tau_{ij}^{\mathrm{FCNN}}$ and $\tau_{ij}^{\mathrm{Smag}}$ were the SGS stresses from the FCNN and Smagorinsky model (with $C_s = 0.09$), respectively, and c_b was a weighting parameter needed to be tuned. Gamahara & Hattori (2017) used FCNNs to predict the SGS stresses with four input variable sets, $\{\nabla\bar{\boldsymbol{u}}, y\}$, $\{\nabla\bar{\boldsymbol{u}}\}$, $\left\{\bar{\boldsymbol{S}}, \bar{\boldsymbol{R}}, y\right\}$, and $\left\{\bar{\boldsymbol{S}}, y\right\}$, where $\bar{\boldsymbol{R}}$ is the filtered rotation rate tensor, and y is the wall-normal distance from the wall. They showed in *a priori* test that the correlation coefficients between the true and predicted SGS stresses from $\{\nabla\bar{\boldsymbol{u}}, y\}$ were highest among four input sets, and even higher than those from traditional SGS models (gradient and Smagorinksy models). However, *a posteriori* test (i.e., actual LES) with $\{\nabla\bar{\boldsymbol{u}}, y\}$ did not provide any advantage over the LES with the Smagorinsky model. Stoffer *et al.* (2020) used FCNNs to predict the SGS stresses with the input of $\bar{\boldsymbol{u}}$ at $5 \times 5 \times 5$ points. This FCNN provided SGS stresses highly correlated with the true one in *a priori*

test, but it produced numerically unstable results in actual LES. This kind of the inconsistency between *a priori* and *a posteriori* tests had been also observed during the development of traditional SGS models (Liu *et al.* 1994; Vreman, Geurts & Kuerten 1997; Park, Yoo & Choi 2005; Anderson & Domaradzki 2012).

Previous studies (Wollblad & Davidson 2008; Gamahara & Hattori 2017; Stoffer *et al.* 2020) showed that FCNN is a promising tool for modeling SGS stresses from *a priori* test, but it is unclear why FCNN-based LESs did not perform better for a turbulent channel flow than LESs with traditional SGS models. Thus, a more systematic investigation on the SGS variables such as the SGS dissipation and transport is required to diagnose the performance of FCNN. The input variables for the FCNN should be also chosen carefully based on the characteristics of the SGS stresses. Therefore, the objective of the present study is to develop an FCNN-based SGS model for a turbulent channel flow, based on both *a priori* and *a posteriori* tests, and to find appropriate input variables for the successful LES with FCNN. We train FCNNs with different input variables such as $\bar{\boldsymbol{S}}$ and $\nabla\bar{\boldsymbol{u}}$, and the target to predict is the SGS stress tensor. We also test $\bar{\boldsymbol{u}}$ and $\partial\bar{\boldsymbol{u}}/\partial y$ as the input for FCNN (note that these were the input variables of the optimal LES for a turbulent channel flow by Völker *et al.* (2002)). The input and target data are obtained by filtering the data from DNS of a turbulent channel flow at the bulk Reynolds number of $Re_b = 5600$ ($Re_\tau = u_\tau\delta/\nu = 178$), where u_τ is the wall-shear velocity, δ is the channel half height, and ν is the kinematic viscosity. In *a priori* test, we examine the variations of the predicted SGS dissipation, backscatter, and SGS transport with the input variables, which are known to be important variables for successful LES of a turbulent channel flow (Piomelli, Yu & Adrian 1996; Völker *et al.* 2002; Park *et al.* 2006). In *a posteriori* test, we perform LESs with FCNN-based SGS models at $Re_\tau = 178$ and estimate their prediction performance by comparing the results with those from

the filtered DNS data and LESs with DSM and scale similarity model (Liu *et al.* 1994). The details about DNS and FCNN are given in §2. The results from *a priori* and *a posteriori* tests at $Re_\tau = 178$ are given in §3. Applications of the FCNN trained at $Re_\tau = 178$ to LES of a higher Reynolds number flow ($Re_\tau = 723$) and to LES with a different grid resolution at $Re_\tau = 178$ are also discussed in §3, followed by conclusions in §4.

Chapter 2

Numerical details

2.1. Neural-network-based SGS model

The governing equations for LES are the spatially filtered continuity and Navier-Stokes equations,

$$\frac{\partial \bar{u}_i}{\partial x_i} = 0, \tag{2.1}$$

$$\frac{\partial \bar{u}_i}{\partial t} + \frac{\partial \bar{u}_i \bar{u}_j}{\partial x_j} = -\frac{\partial \bar{p}}{\partial x_i} + \frac{1}{Re}\frac{\partial^2 \bar{u}_i}{\partial x_j \partial x_j} - \frac{\partial \tau_{ij}}{\partial x_j}, \tag{2.2}$$

where $x_1(= x)$, $x_2(= y)$, and $x_3(= z)$ are the streamwise, wall-normal, and spanwise directions, respectively, $u_i(= u, v, w)$ are the corresponding velocity components, p is the pressure, t is time, the overbar denotes the filtering operation, and $\tau_{ij}(= \overline{u_i u_j} - \bar{u}_i \bar{u}_j)$ is the SGS stress tensor. We use a fully connected neural network (denoted as NN hereafter) with the input of the filtered flow variables to predict τ_{ij}. The database for training NN is obtained by filtering the instantaneous flow fields from DNS of a turbulent channel flow at $Re_\tau = 178$ (see §2.2). To estimate the performance of the present NN-based SGS model, we perform two additional LESs with the dynamic Smagorinsky (Germano *et al.* 1991; Lilly 1992) and scale similarity (Liu *et al.* 1994) models. For the dy-

namic Smagorinsky model (DSM), $\tau_{ij} - \frac{1}{3}\tau_{kk}\delta_{ij} = -2C^2 \left|\bar{S}\right| \bar{S}_{ij}$, where $C^2 = -\frac{1}{2}\langle L_{ij} M_{ij}\rangle_h / \langle M_{ij} M_{ij}\rangle_h$, $\left|\bar{S}\right| = \sqrt{2\bar{S}_{ij}\bar{S}_{ij}}$, $\bar{S}_{ij} = \frac{1}{2}\left(\partial\bar{u}_i/\partial x_j + \partial\bar{u}_j/\partial x_i\right)$, $L_{ij} = \widetilde{\bar{u}_i\bar{u}_j} - \tilde{\bar{u}}_i\tilde{\bar{u}}_j$, $M_{ij} = \left(\tilde{\Delta}/\bar{\Delta}\right)^2 \left|\tilde{\bar{S}}\right| \tilde{\bar{S}}_{ij} - \widetilde{\left|\bar{S}\right| \bar{S}_{ij}}$, $\bar{\Delta}$ and $\tilde{\Delta}(= 2\bar{\Delta})$ denote the grid and test filter sizes, respectively, and $\langle\rangle_h$ denotes averaging in the homogeneous (x and z) directions. For the scale similarity model (SSM), $\tau_{ij} = \widetilde{\bar{u}_i\bar{u}_j} - \tilde{\bar{u}}_i\tilde{\bar{u}}_j$, where $\tilde{k}_{cut} = 0.5\bar{k}_{cut}$ and k_{cut} is the cut-off wavenumber.

The NN adopted in the present study has two hidden layers with 128 neurons per hidden layer, and the output of the NN is the six components of τ_{ij} (figure 2.1). Previous studies used one (Gamahara & Hattori 2017; Maulik & San 2017; Maulik *et al.* 2018; Zhou *et al.* 2019; Stoffer *et al.* 2020) or two (Sarghini *et al.* 2003; Wollblad & Davidson 2008; Vollant *et al.* 2017; Wang *et al.* 2018; Maulik *et al.* 2019; Xie *et al.* 2019*a*,*b*,*c*, 2020*a*,*c*; Pawar *et al.* 2020) hidden layers, and Gamahara & Hattori (2017) showed that 100 neurons per hidden layer were sufficient for the accurate predictions of τ_{ij} for a turbulent channel flow in *a priori* test. We also tested NN with three hidden layers, but more hidden layers than two did not further improve the performance both in *a priori* and *a posteriori* tests (see figure 2.3).

In the present NN, the output of the mth layer, $\boldsymbol{h}^{(m)}$, is as follows:

$$
\begin{aligned}
&h_i^{(1)} = q_i \ (i = 1, 2, ..., N_q);\\
&h_j^{(2)} = \max[0, r_j^{(2)}],\ r_j^{(2)} = \gamma_j^{(2)} \left(\sum\nolimits_{i=1}^{N_q} W_{ij}^{(1)(2)} h_i^{(1)} + b_j^{(2)} - \mu_j^{(2)} \right) / \sigma_j^{(2)} + \beta_j^{(2)}\\
&\qquad (j = 1, 2, ..., 128);\\
&h_k^{(3)} = \max[0, r_k^{(3)}],\ r_k^{(3)} = \gamma_k^{(3)} \left(\sum\nolimits_{j=1}^{128} W_{jk}^{(2)(3)} h_j^{(2)} + b_k^{(3)} - \mu_k^{(3)} \right) / \sigma_k^{(3)} + \beta_k^{(3)}\\
&\qquad (k = 1, 2, ..., 128);\\
&h_l^{(4)} = s_l = \sum\nolimits_{k=1}^{128} W_{kl}^{(3)(4)} h_k^{(3)} + b_l^{(4)} \ (l = 1, 2, ..., 6),
\end{aligned}
$$

where q_i is the input, N_q is the number of input components, $\boldsymbol{W}^{(m)(m+1)}$ is the

weight matrix between the mth and $(m+1)$th layers, $\boldsymbol{b}^{(m)}$ is the bias of the mth layer, s_l is the output, and $\boldsymbol{\mu}^{(m)}$, $\boldsymbol{\sigma}^{(m)}$, $\boldsymbol{\gamma}^{(m)}$, and $\boldsymbol{\beta}^{(m)}$ are parameters for a batch normalization (Ioffe & Szegedy 2015). We use a rectified linear unit (Relu; Nair & Hinton 2010), $\boldsymbol{h}^{(m)} = \max[0, \boldsymbol{r}^{(m)}]$, as the activation function at the hidden layers. We also tested other typical activation functions such as sigmoid and hyperbolic tangent functions, but the convergence of the loss function (2.3) was faster with the Relu than with others. $\boldsymbol{W}^{(m)(m+1)}$, $\boldsymbol{b}^{(m)}$, $\boldsymbol{\gamma}^{(m)}$, and $\boldsymbol{\beta}^{(m)}$ are trainable parameters which are optimized to minimize the loss function defined as

$$L = \frac{1}{2N_b}\frac{1}{6}\sum_{l=1}^{6}\sum_{n=1}^{N_b}\left(s_{l,n}^{\mathrm{fDNS}} - s_{l,n}\right)^2 + 0.005\sum_{o} w_o^2, \qquad (2.3)$$

where $s_{l,\,n}^{\mathrm{fDNS}}$ is the SGS stresses obtained from filtered DNS data, N_b is the number of minibatch data (128 in this study following Kingma & Ba 2014), and w_o denotes the components of $\boldsymbol{W}^{(m)(m+1)}$. An adaptive moment estimation (Kingma & Ba 2014), which is a variant of gradient descent method, is applied to update the trainable parameters, and the gradients of the loss function with respect to those parameters are calculated through the chain rule of derivatives (Rumelhart, Hinton & Williams 1986; LeCun, Bengio & Hinton 2015). All training procedures are conducted using the python-opensource-library TensorFlow.

We choose five different input variables (corresponding to NN1 - NN5), as listed in table 2.1. Six components of $\bar{S}_{ij}$ and nine components of $\bar{\alpha}_{ij}(= \partial\bar{u}_i/\partial x_j)$ at each grid point are the inputs to NN1 and NN2, respectively, and the output is six components of τ_{ij} at the same grid location. The input $\bar{\alpha}_{ij}$ is selected for NN2 because τ_{ij} can be written as $\tau_{ij} = 2\gamma\bar{\alpha}_{ik}\bar{\alpha}_{jk} + O(\gamma^2)$, where $\gamma(\zeta) = \int_{-\infty}^{\infty}\xi^2 G(\xi,\zeta)\mathrm{d}\xi$ and $G(\xi,\zeta)$ is the kernel of the filter (Bedford & Yeo 1993). On the other hand, a general class of SGS model based on the local velocity gradient (Lund & Novikov 1992; Silvis *et al.* 2019) can be expressed as $\tau_{ij} = \sum_{k=0}^{5} c^{(k)} T_{ij}^{(k)}$, where $c^{(k)}$ is the model coefficient, $T_{ij}^{(0)} = \delta_{ij}$,

$T_{ij}^{(1)} = \bar{S}_{ij}$, $T_{ij}^{(2)} = \bar{S}_{ik}\bar{S}_{kj}$, $T_{ij}^{(3)} = \bar{R}_{ik}\bar{R}_{kj}$, $T_{ij}^{(4)} = \bar{S}_{ik}\bar{R}_{kj} - \bar{R}_{ik}\bar{S}_{kj}$, $T_{ij}^{(5)} = \bar{S}_{ik}\bar{S}_{kl}\bar{R}_{lj} - \bar{R}_{ik}\bar{S}_{kl}\bar{S}_{lj}$, and $\bar{R}_{ij}$ is the filtered rotation rate tensor. Thus, NN1 can be regarded as an SGS model including $T_{ij}^{(0)}$, $T_{ij}^{(1)}$ and $T_{ij}^{(2)}$, but it directly predicts τ_{ij} through a nonlinear process of NN rather than predicting $c^{(k)}$. In NN3 and NN4, a stencil of data at $3(x) \times 3(z)$ grid points are the input, and τ_{ij} at the center of this stencil is the output. In NN5, the filtered velocity and wall-normal velocity gradient at $3(x) \times 3(z)$ grid points are the input variables, and the output is the same as that of NN3 and NN4. The use of a stencil of data for NN3 - NN5 is motivated by the results of Xie *et al.* (2019*c*) that using a stencil of input variables ($\bar{\alpha}_{ij}$ and temperature gradient) predicted τ_{ij} better than using the same input only at one grid point. The choice of $\bar{u}_i$ and $\partial\bar{u}_i/\partial y$ as the input of NN5 is also motivated by the results of optimal LES by Völker *et al.* (2002), in which LES with the input of both $\bar{u}_i$ and $\partial\bar{u}_i/\partial y$ outperformed that with the input of $\bar{u}_i$ alone. We also considered an NN with the input of $\bar{u}_i$ at $n_x(x) \times 3(y) \times n_z(z)$ grid points, where $n_x = n_z = 3, 5, 7$, or 9. The results with these three-dimensional multiple input grid points were little different in *a priori* tests from that of NN5. As shown in §3, the results with NN3 - NN5 in *a priori* tests are better than those with NN1 and NN2 (single input grid point), but actual LES (i.e. *a posteriori* test) with NN3 - NN5 are unstable. Therefore, we did not seek to adopt more input grid points. Note also that we train a single NN for all y locations using pairs of the input and output variables. The relations between these variables are different for different y locations, and thus y locations are implicitly embedded in this single NN. One may train an NN at each y location, but this procedure increases the number of NNs and the memory size. On the other hand, Gamahara & Hattori (2017) provided y locations as an additional input variable for a single NN, but found that the result of *a priori* test with y location was only slightly better than that without y location. Therefore, we do not attempt to

include y location as an additional input variable in this study.

While training NN1 - NN5, the input and output variables are normalized in wall units, which provides successful results because the flow variables in turbulent channel flow are well scaled in wall units (see §3). Since the performance of an NN depends on the normalization of input and output variables (see, for example, Passalis *et al.* 2019), we considered two more normalizations: one was with the centerline velocity (U_c) and channel half height (δ), and the other was such that the input and output variables were scaled to have zero mean and unit variance at each y location, e.g., $\tau_{ij}^{*}(x,y,z,t) = \left(\tau_{ij}(x,y,z,t) - \tau_{ij}^{mean}(y)\right) / \tau_{ij}^{rms}(y)$ (no summation on i and j), where the superscripts of *mean* and *rms* denote the mean and root-mean-square values, respectively. The first normalization was not successful for the prediction of a higher Reynolds number flow with an NN trained at lower Reynolds number, because the near-wall flow was not properly scaled with this normalization. The second normalization requires *a priori* knowledge on $\tau_{ij}^{mean}(y)$ and $\tau_{ij}^{rms}(y)$ even for a higher Reynolds number flow to predict. Thus, we did not take the second normalization either.

Figure 2.2 shows the variations of the training error ϵ_τ with the epoch, and the correlation coefficients ρ_τ between true and predicted SGS stresses for NN1 - NN5, where ϵ_τ and ρ_τ are defined as

$$\epsilon_\tau = \frac{1}{2\mathrm{N_{data}}} \frac{1}{6} \sum_{l=1}^{6} \sum_{n=1}^{\mathrm{N_{data}}} \left(s_{l,n}^{\mathrm{fDNS}} - s_{l,n} \right)^2, \tag{2.4}$$

$$\rho_\tau = \sum_{l=1}^{6} \sum_{n=1}^{\mathrm{N_{data}}} \left(s_{l,n}^{\mathrm{fDNS}} s_{l,n} \right) \Bigg/ \left(\sqrt{\sum_{l=1}^{6} \sum_{n=1}^{\mathrm{N_{data}}} \left(s_{l,n}^{\mathrm{fDNS}} \right)^2} \sqrt{\sum_{l=1}^{6} \sum_{n=1}^{\mathrm{N_{data}}} \left(s_{l,n} \right)^2} \right). \tag{2.5}$$

Here, one epoch denotes one sweep through the entire training dataset (Hastie, Tibshirani & Friedman 2009), and $\mathrm{N_{data}}$ is the number of entire training data. The training errors nearly converge at 20 epochs (figure 2.3*a*). In terms of computational time using a single graphic process unit (NVIDIA GeForce GTX 1060),

about one minute is spent for each epoch. The correlation coefficients from the training and test datasets are quite similar to each other (figure 2.3*b*), indicating that severe overfitting is not observed for NN1 - NN5. The training error and correlation coefficient are smaller and bigger, respectively, for NN3 - NN5 than those for NN1 and NN2.

Sarghini *et al.* (2003) and Pal (2019) indicated that required computational time for their LESs with NNs was less than that with traditional SGS models. When an NN is used for obtaining the SGS stresses, its cost depends on the numbers of hidden layers and neurons therein as well as the choices of input and output variables. Actually, in the present study, the computational time required for one computational-time-step advancement with NN1 is approximately 1.3 times that with a traditional SGS model like DSM.

Figure 2.3 shows the effects of the number of hidden layers of NNs (NN1, NN3 and NN5) on the mean SGS and Reynolds shear stresses from *a priori* and *a posteriori* tests, respectively. The details of *a priori* and *a posteriori* tests are described in §3. The Reynolds shear stress from NN3 and NN5 are obtained from LES with clipping the backscatter (see equation (3.1)). For all NNs considered, one hidden layer is not sufficient for accurately predicting the mean SGS shear stress, and at least two hidden layers are required. In actual LES, one hidden layer seems to be sufficient for NN1 and NN3, and two hidden layers are required for NN5. Therefore, two hidden layers are taken for the present study for all NNs considered.

2.2. Details of DNS and input and output variables

A DNS of turbulent channel flow at $Re_b = 5600\,(Re_\tau = 178)$ is conducted to obtain the input and output of NN1 - NN5 (table 2.1), where Re_b is the bulk Reynolds number defined by $Re_b = U_b(2\delta)/\nu$, U_b is the bulk velocity, and

$Re_\tau = u_\tau \delta / \nu$ is the friction Reynolds number. The Navier-Stokes and continuity equations are solved in the form of the wall-normal vorticity and the Laplacian of the wall-normal velocity, as described in Kim *et al.* (1987). The dealiased Fourier and Chebyshev polynomial expansions are used in the homogeneous (x and z) and wall-normal (y) directions, respectively. A semi-implicit fractional step method is used for time integration, where a third-order Runge-Kutta and second-order Crank-Nicolson methods are applied to the convection and diffusion terms, respectively. A constant mass flux in a channel is maintained by adjusting the mean pressure gradient in the streamwise direction at each time step.

Table 2.2 shows the computational parameters of DNS, where N_{x_i}'s are the numbers of grid points in x_i directions, L_{x_i}'s are the corresponding computational domain sizes, Δx and Δz are the uniform grid spacings in x and z directions, respectively, and Δy^+_{min} is the smallest grid spacing at the wall in the wall-normal direction. Δ_x and Δ_z are the filter sizes in x and z directions, respectively, and they are used for obtaining filtered DNS (called fDNS hereafter) data. We apply the spectral cut-off filter only in the wall-parallel (x and z) directions as in the previous studies (Piomelli *et al.* 1991, 1996; Völker *et al.* 2002; Park *et al.* 2006). The use of only wall-parallel filters can be justified because small scales are efficiently filtered out by wall-parallel filters and wall-normal filtering through the truncation of the Chebyshev mode violates the continuity unless the divergence-free projection is performed (Völker *et al.* 2002; Park *et al.* 2006). The Fourier coefficient of a filtered flow variable $\hat{\bar{f}}$ is defined as

$$\hat{\bar{f}}\left(k_x, y, k_z, t\right) = \hat{f}\left(k_x, y, k_z, t\right) H\left(k_{x,cut} - \left|k_x\right|\right) H\left(k_{z,cut} - \left|k_z\right|\right), \quad (2.6)$$

where $\hat{f}$ is the Fourier coefficient of an unfiltered flow variable f, H is the Heaviside step function, and $k_{x,cut}$ and $k_{z,cut}$ are the cut-off wavenumbers in x

and z directions, respectively. The filter sizes in table 2.2, Δ_x^+ and Δ_z^+, are the same as those in Park *et al.* (2006), and the corresponding cut-off wavenumbers are $k_{x,cut} = 8\,(2\pi/L_x)$ and $k_{z,cut} = 8\,(2\pi/L_z)$, respectively. Figure 2.4 shows the mean velocity profile and turbulence intensities from the DNS and fDNS. Since the filtering is only applied in x and z directions, the mean velocity profile of fDNS is the same as that of DNS. The turbulence intensities of fDNS, however, are smaller than those of DNS, as the filtering smooths out velocity fluctuations.

We use the input and output database at $Re_\tau = 178$ to train NN1 - NN5. The training data are collected at every other grid point in x and z directions to exclude highly correlated data, and at all grid points in y direction from 200 instantaneous fDNS fields. Then, the number of training data from 200 fDNS fields is 1,241,600 ($= 200 \times N_x^{\mathrm{fDNS}}/2 \times N_z^{\mathrm{fDNS}}/2 \times N_y$), where $N_x^{\mathrm{fDNS}} = L_x k_{x,cut}/\pi$ and $N_z^{\mathrm{fDNS}} = L_z k_{z,cut}/\pi$. We have also tested 300 fDNS fields for training NNs, but their prediction performance for the SGS stresses is not further improved, so the number of training data used is sufficient for the present NNs. A DNS at a higher Reynolds number of $Re_\tau = 723$ is also carried out, and its database is used to estimate the prediction capability of the present NN-based SGS model for untrained higher Reynolds number flow.

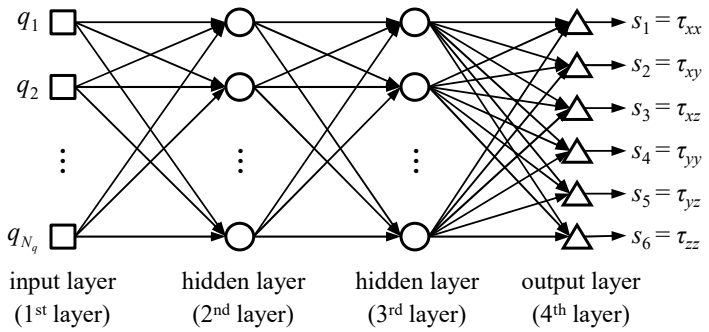

FIGURE 2.1. Schematic diagram of the present NN with two hidden layers (128 neurons per hidden layer). Here, $\boldsymbol{q}(= [q_1, q_2, ..., q_{N_q}]^T)$ is the input of NN, N_q is the number of input components (see table 2.1) and $\boldsymbol{s}(= [s_1, s_2, ..., s_6]^T)$ is the output of NN.

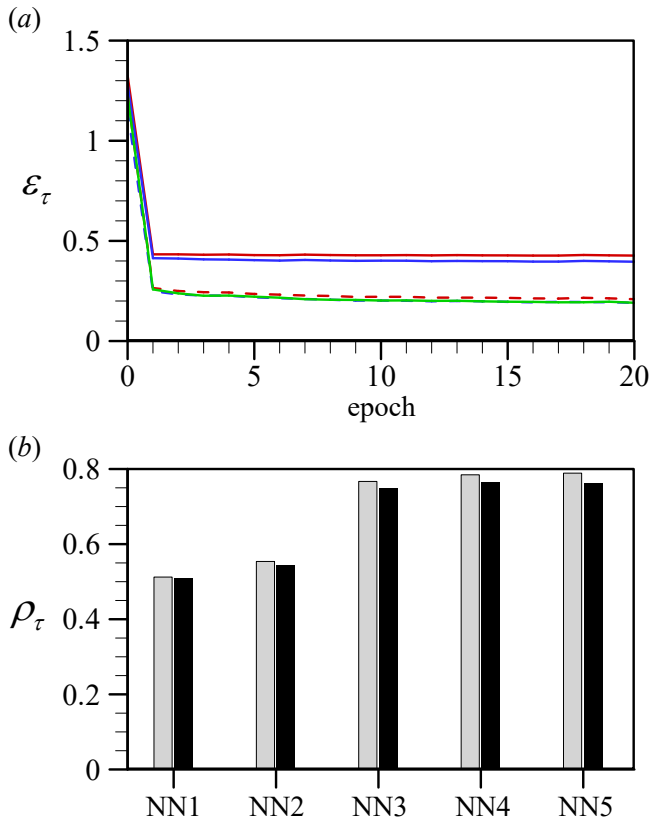

FIGURE 2.2. Training error and correlation coefficient by NN1 - NN5: (*a*) training error vs. epoch; (*b*) correlation coefficient. In (*a*), —, NN1; —, NN2; - - -, NN3; - - -, NN4; —, NN5. In (*b*), gray and black bars are the correlation coefficients for training and test datasets, respectively, where the number of test data is the same as that of the training data ($N_{data} = 1,241,600$ (§2.2)).

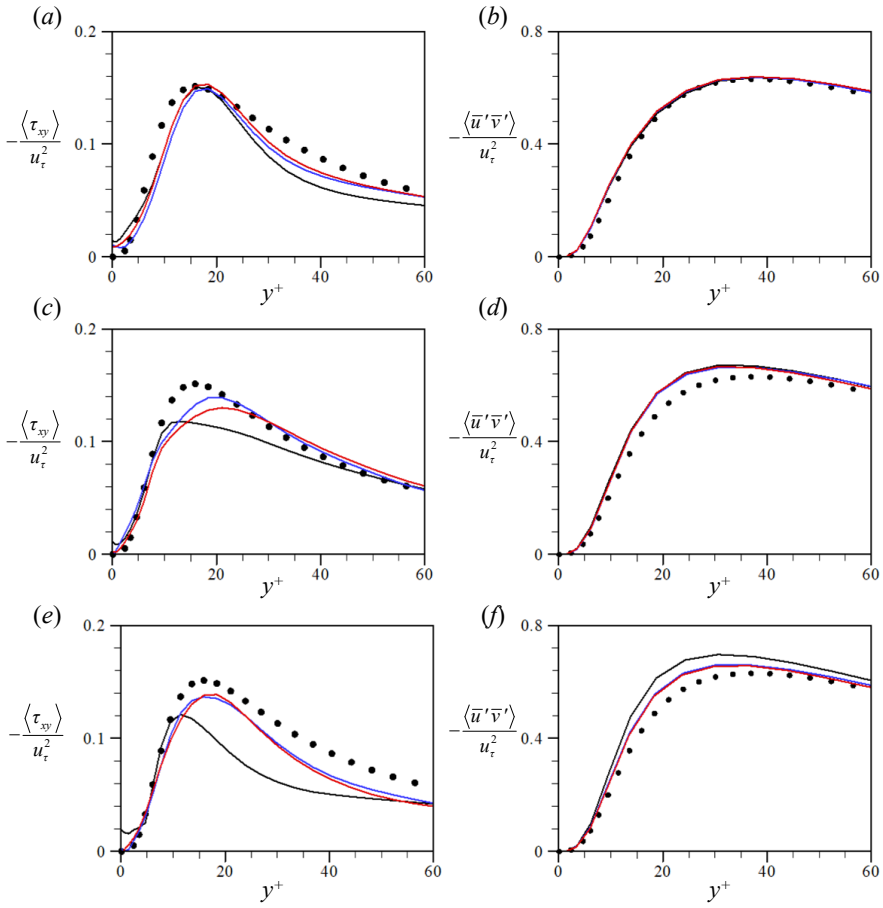

FIGURE 2.3. Effects of the number of hidden layers (N_{hl}): (a, c, e) the mean SGS shear stress (*a priori* test at $Re_\tau = 178$); (b, d, f) Reynolds shear stress (*a posteriori* test; LES178). (a, b) NN1; (c, d) NN3; (e, f) NN5. ●, fDNS; —, $N_{hl} = 1$; —, $N_{hl} = 2$; —, $N_{hl} = 3$.

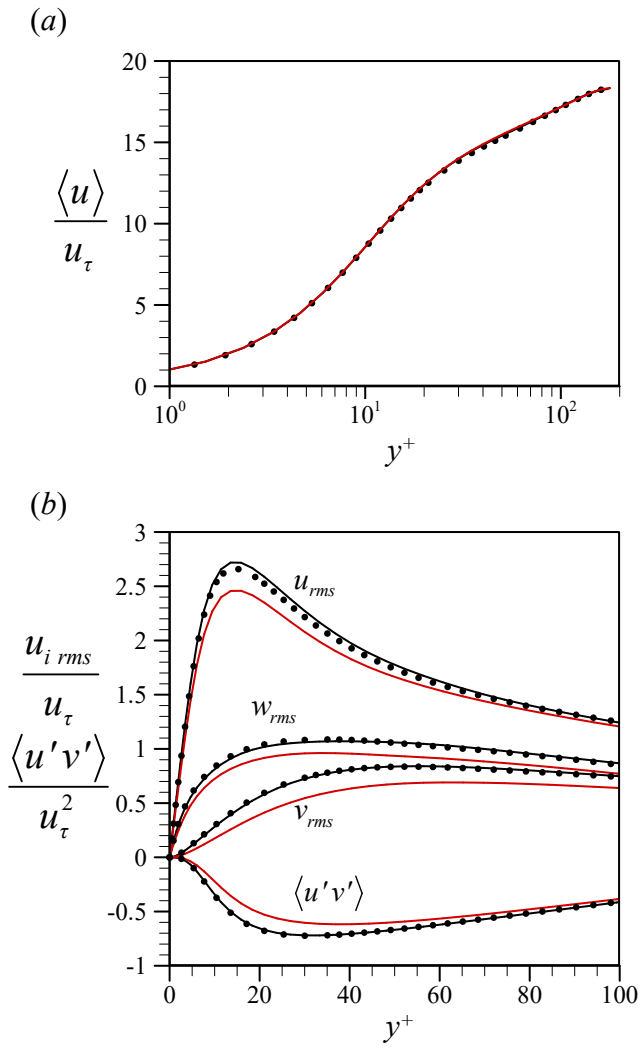

FIGURE 2.4. Results of DNS and fDNS at $Re_\tau = 178$: (*a*) Mean velocity profile; (*b*) root-mean-square velocity fluctuations and the Reynolds shear stress. ——, DNS; ——, fDNS; ●, previous DNS (Moser *et al.* 1999).

NN model	input variable(s)	input grid point(s)	N_q
NN1	$\bar{S}_{ij}$	1	6
NN2	$\bar{\alpha}_{ij}$	1	9
NN3	$\bar{S}_{ij}$	$3(x) \times 3(z)$	54
NN4	$\bar{\alpha}_{ij}$	$3(x) \times 3(z)$	81
NN5	$\bar{u}_i$ and $\partial \bar{u}_i / \partial y$	$3(x) \times 3(z)$	54

TABLE 2.1. Input variables of NN models. Here, N_q is the number of input components.

Re_b	Re_τ	N_x, N_y, N_z	$L_x/\delta, L_z/\delta$	$\Delta x^+, \Delta z^+, \Delta y^+_{min}$	ΔT^+	Δ^+_x, Δ^+_z
5600	178	96, 97, 96	$2\pi, \pi$	11.7, 5.8, 0.1	9.4	69.9, 35.0
27600	723	192, 193, 192	$\pi, 0.5\pi$	11.8, 5.9, 0.1	11.4	71.0, 35.5

TABLE 2.2. Computational parameters of DNS. Here, the superscript + denotes the wall unit, and ΔT is the sampling time interval of the instantaneous DNS flow fields for constructing the input and output database.

Chapter 3

Results

In §3.1, we perform *a priori* tests for two different Reynolds numbers, $Re_\tau = 178$ and 723, in which the SGS stresses are predicted by NN1 - NN5 with the input variables from fDNS at each Reynolds number, and compared with the SGS stresses from fDNS. Note that NN1 - NN5 are constructed at $Re_\tau = 178$, and $Re_\tau = 723$ is an untrained higher Reynolds number. The filter sizes used in *a priori* tests, Δ_x^+ and Δ_z^+, are given in table 2.2. In §3.2, *a posteriori* tests (i.e., actual LESs solving (2.1) and (2.2)) with NN1 - NN5 are performed for a turbulent channel flow at $Re_\tau = 178$ and their results are compared with those of fDNS. Furthermore, LES with NN1 (trained at $Re_\tau = 178$) is carried out for a turbulent channel flow at $Re_\tau = 723$ and its results are compared with those of fDNS. Finally, in §3.3, we provide the results when the grid resolution in LES is different from that used in training NN1, and suggest a way to obtain good results.

3.1. *A priori* test

Figure 3.1 shows the mean SGS shear stress $\langle \tau_{xy} \rangle$ and dissipation $\langle \varepsilon_{SGS} \rangle$ predicted by NN1 - NN5, together with those of fDNS and from DSM and SSM, where $\varepsilon_{SGS} = -\tau_{ij}\bar{S}_{ij}$ and $\langle\ \rangle$ denotes the averaging in the homogeneous directions and time. Predictions of $\langle \tau_{xy} \rangle$ by NNs (except that by NN2) are better than those by DSM and SSM, and NN5 provides an excellent prediction of $\langle \varepsilon_{SGS} \rangle$ albeit other NN models are also good in the estimation of $\langle \varepsilon_{SGS} \rangle$. Table 3.1 shows the correlation coefficients ρ between the true and predicted τ_{xy} and ε_{SGS}, respectively. τ_{xy}'s predicted by DSM and SSM have very low correlations with true τ_{xy}, as reported by Liu *et al.* (1994) and Park *et al.* (2005). On the other hand, NN1 - NN5 have much higher correlations of τ_{xy} and ε_{SGS} than those by DSM and SSM, indicating that instantaneous τ_{xy} and ε_{SGS} are relatively well captured by NN1 - NN5. These SGS variables are even better predicted by having the input variables at multiple grid points (NN3 - NN5) than at single grid point (NN1 and NN2). As we show below, however, high correlation coefficients of τ_{xy} and ε_{SGS} in *a priori* test do not necessarily guarantee excellent prediction performance in actual LES. Figure 3.2(a) shows the mean SGS transport $\langle T_{SGS} \rangle$, where $T_{SGS} = \partial(\tau_{ij}\bar{u}_i)/\partial x_j$. Völker *et al.* (2002) indicated that a good prediction of $\langle T_{SGS} \rangle$ is necessary for an accurate LES, and the optimal LES provided good representation of $\langle T_{SGS} \rangle$ in *a posteriori* test. Among NN models considered, NN5 shows the best agreement of $\langle T_{SGS} \rangle$ with that of fDNS, but NN1 and NN2 are not good at accurately predicting $\langle T_{SGS} \rangle$ although they are still better than SSM. Figure 3.2(b) shows the mean backward SGS dissipation (backscatter, i.e., energy transfer from subgrid to resolved scales), $\langle \varepsilon^{-}_{SGS} \rangle = \frac{1}{2}\langle \varepsilon_{SGS} - |\varepsilon_{SGS}| \rangle$. $\langle \varepsilon^{-}_{SGS} \rangle = 0$ for DSM due to the averaging procedure in determining the model coefficient. The mean backscatters from SSM and NN3 - NN5 show reasonable agreements with that of fDNS, but NN1 and NN2 severely underpredict the

backscatter. An accurate prediction of backscatter is important in wall-bounded flows, because it is related to the bursting and sweep events (Härtel *et al.* 1994; Piomelli *et al.* 1996). However, SGS models with non-negligible backscatter such as SSM do not properly dissipate energy and incur numerical instability in actual LES (Liu *et al.* 1994; Meneveau & Katz 2000; Akhavan *et al.* 2000; Anderson & Domaradzki 2012). For this reason, some NN-based SGS models suggested in the previous studies clipped the backscatter to be zero for ensuring stable LES results (Maulik *et al.* 2018, 2019; Zhou *et al.* 2019). Therefore, the accuracy and stability in the solution from LES with NN3 - NN5 may not be guaranteed, even if these models properly predict the backscatter and produce high correlation coefficients between the true and predicted SGS stresses.

Figure 3.3 shows the statistics from *a priori* test for $Re_\tau = 723$ with NN-based SGS models trained at $Re_\tau = 178$. The statistics predicted by NN1 - NN5 for $Re_\tau = 723$ show very similar behaviors to those for $Re_\tau = 178$, except for an underprediction of $\langle \tau_{xy} \rangle$ by NN1 (similar to that by DSM) which does not degrade its prediction capability in *a posteriori* test (see §2.2).

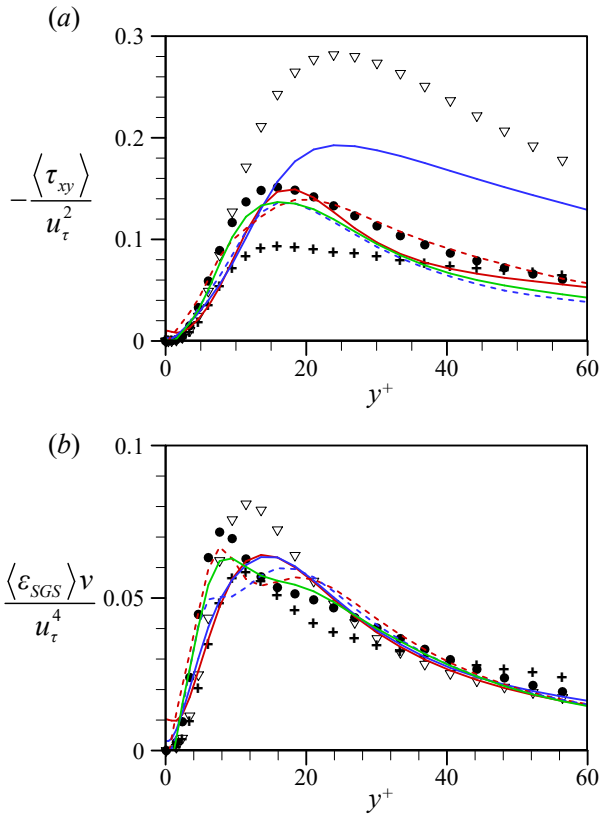

FIGURE 3.1. Mean SGS shear stress and dissipation predicted by NN1 - NN5 (*a priori* test at $Re_\tau = 178$): (*a*) mean SGS shear stress $\langle \tau_{xy} \rangle$; (*b*) mean SGS dissipation $\langle \varepsilon_{SGS} \rangle$. ●, fDNS; —, NN1; —, NN2; - - -, NN3; - - -, NN4; —, NN5; +, DSM; ▽, SSM.

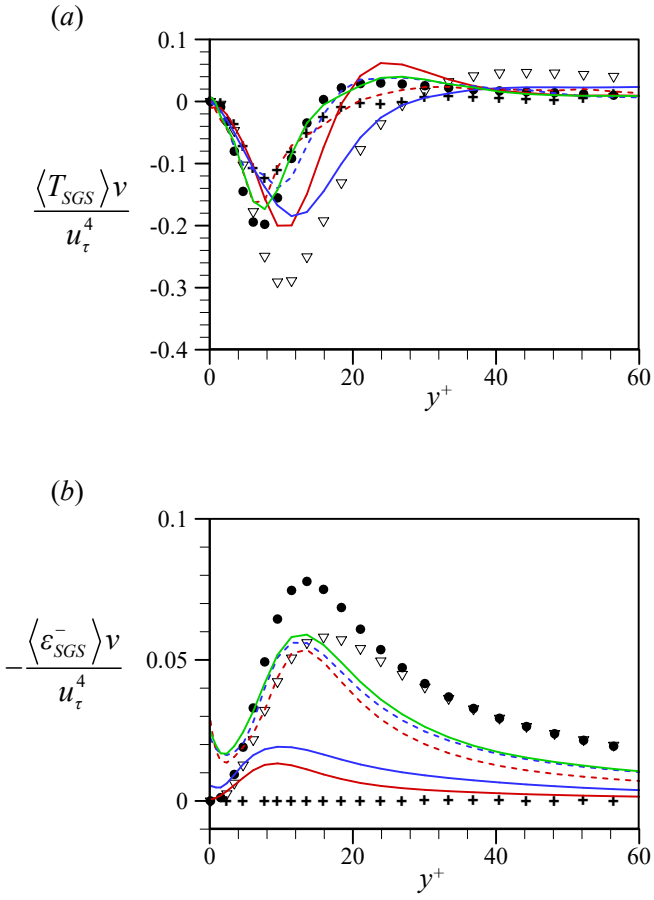

FIGURE 3.2. Mean SGS transport and backward SGS dissipation predicted by NN1 - NN5 (*a priori* test at $Re_\tau = 178$): (*a*) mean SGS transport $\langle T_{SGS} \rangle$; (*b*) mean backward SGS dissipation (backscatter) $\langle \varepsilon_{SGS}^- \rangle$. ●, fDNS; —, NN1; —, NN2; - - -, NN3; - - -, NN4; —, NN5; +, DSM; ▽, SSM.

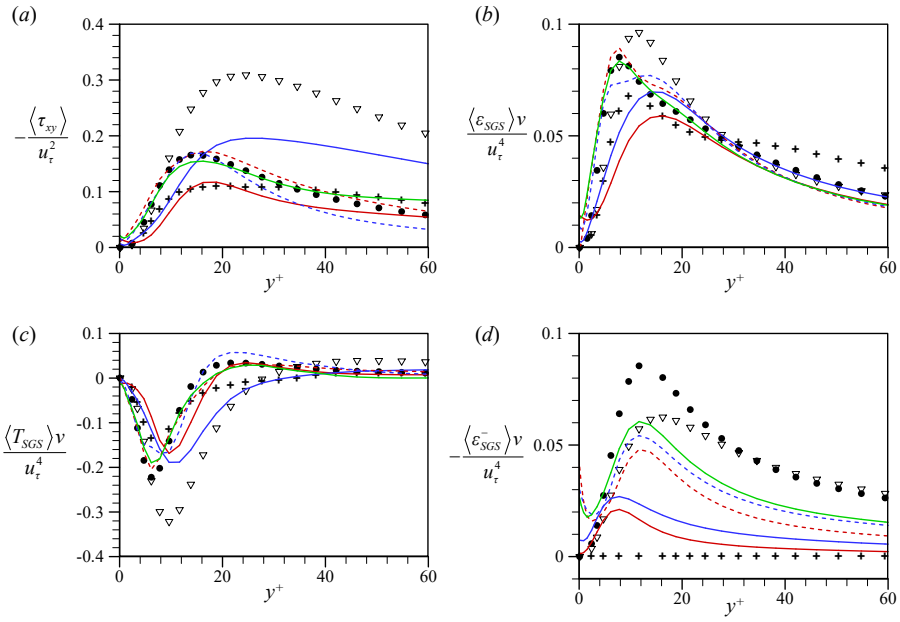

FIGURE 3.3. Statistics from *a priori* test at $Re_\tau = 723$: (a) mean SGS shear stress $\langle \tau_{xy} \rangle$; ($b$) mean SGS dissipation $\langle \varepsilon_{SGS} \rangle$; ($c$) mean SGS transport $\langle T_{SGS} \rangle$; (d) mean backscatter $\langle \varepsilon_{SGS}^- \rangle$. ●, fDNS; —, NN1; —, NN2; - - -, NN3; - - -, NN4; —, NN5; +, DSM; ▽, SSM. Here, NN1 - NN5 are trained with fDNS at $Re_\tau = 178$.

	NN1	NN2	NN3	NN4	NN5	DSM	SSM
$\rho_{\tau_{xy}}$	0.231	0.432	0.414	0.630	0.600	0.090	-0.016
$\rho_{\varepsilon_{SGS}}$	0.358	0.472	0.507	0.624	0.576	0.165	0.081

TABLE 3.1. Correlation coefficients between the true and predicted τ_{xy} and ε_{SGS}.

3.2. *A posteriori* test

In this section, *a posteriori* tests (i.e., actual LESs) with NN-based SGS models are conducted for a turbulent channel flow with a constant mass flow rate ($Re_b = 5600$ or 27600). Numerical methods for solving the filtered Navier-Stokes and continuity equations are the same as those of DNS described in §2.2. Table 3.2 shows the computational parameters of LES. The grid resolution for the cases of LES178 is the same as that of Park *et al.* (2006). The cases of LES178 have nearly the same grid resolutions in wall units (because of slightly different values of Re_τ's) in x and z directions as those of fDNS used in training NNs, and the cases of LES178c and LES178f use larger and smaller grid sizes in x and z directions than those of trained data, respectively. In the case of LES723 ($Re_\tau = 723$), the grid sizes in wall units in x and z directions are nearly the same as those of trained data.

In the present LESs with NN3 - NN5 and SSM, we clip the SGS stresses to be zero wherever backscatter occurs, i.e., $\tau_{ij} = 0$ when $\varepsilon_{SGS} < 0$, as done in the previous studies (Maulik *et al.* 2018, 2019; Zhou *et al.* 2019). Otherwise, the solution diverges. While removing the backscatter, we rescale the SGS stresses to maintain the net amount of SGS dissipation in the computational domain V as follows:

$$\tau_{ij}^{*} = \frac{1}{2}\left[1 + \mathrm{sign}(\varepsilon_{SGS})\right]\tau_{ij} \cdot \frac{\int_V \varepsilon_{SGS}\,\mathrm{d}V}{\frac{1}{2}\int_V \left(\varepsilon_{SGS} + |\varepsilon_{SGS}|\right)\mathrm{d}V}. \tag{3.1}$$

This backscatter clipping and rescaling on τ_{ij} is similar to that of Akhavan *et al.* (2000) in their development of dynamic two-component model. For the cases of LESs with NN1 and NN2, we obtain stable solutions without any special treatment such as the clipping, wall damping or averaging over homogeneous directions, and thus we perform LESs with and without clipping, respectively. In LES with DSM, an averaging procedure is included to determine the model

coefficient, as mostly done in previous studies. Since the present simulations are conducted for a constant mass flow rate in a channel, the wall-shear velocity or Re_τ changes depending on the choice of SGS models. Those Re_τ's are listed in table 3.3. For $Re_b = 5600$, Re_τ's from LES178 are well predicted by NN1 and NN2 even without clipping (less than 2 % error) and by NN3 - NN5 with clipping (less than 3% error). On the other hand, Re_τ from no SGS model has about 10 % error.

Figure 3.4 shows the mean velocity profiles from LES178 for various SGS models without and with clipping the backscatter, respectively. Without clipping, LESs with NN1 and NN2 show excellent predictions of the mean velocity, but those with NN3 - NN5 and SSM diverge. On the other hand, with clipping, LESs with all the SGS models considered provide very good predictions of the mean velocity, which clearly indicates that backscatter incurs numerical instability in LES. Therefore, in the following, we present the results of LESs with clipping for NN3 - NN5, and without clipping for NN1 and NN2, respectively.

Figure 3.5 shows the statistics of various turbulence quantities from LES178 with NN1 - NN5, together with those of fDNS and from LESs with DSM and SSM. All NNs considered show good predictions of the root-mean-square (rms) velocity fluctuations (figure 3.5*a*). While LES without SGS model (i.e., coarse DNS) fortuitously well predicts $\bar{u}_{rms}$ due to overpredicted friction velocity, LES with DSM overpredicts it (Park *et al.* 2006). Since DSM determines the model coefficient $C^2(y)$ to be uniform in the homogeneous directions ignoring the locality of $C^2(x, y, z)$, its prediction performance of local SGS dissipation is degraded and may result in the overprediction of $\bar{u}_{rms}$. For the predictions of the Reynolds shear stress and SGS shear stress, NN1 performs the best among all the SGS models considered (figures 3.5*b* and *c*). On the other hand, NN2 underpredicts the Reynolds shear stress and significantly overpredicts the SGS shear stress.

This result is consistent with that of *a priori* test (figure 3.1*a*). The overprediction of $\langle \tau_{xy} \rangle$ results in the underprediction of $-\langle \bar{u}'\bar{v}' \rangle$ from the total shear stress equation, $d\langle \bar{u}^+ \rangle / dy^+ - \langle \bar{u}'\bar{v}' \rangle / u_\tau^2 - \langle \tau_{xy} \rangle / u_\tau^2 = 1 - y/\delta$. NN3 - NN5 slightly overpredict the Reynolds shear stress but underpredict the SGS shear stress. These NN models (NN3 - NN5) are forced not to produce the backscatter due to the clipping as described before. NN1 and NN2 provide backscatter but underpredict it (figure 3.5*d*). Note that DSM and SSM also require an averaging over the homogeneous directions and clipping the backscatter, respectively, for stable solution, and thus $\varepsilon^-_{SGS} = 0$. Therefore, NN1 is the most promising SGS model for LES of turbulent channel flow among the NN models considered, even though NN3 - NN5 show better prediction performance in *a priori* test. NN1 also shows the best prediction of the mean SGS transport $\langle T_{SGS} \rangle$ (figure 3.5*e*), confirming that a good prediction of $\langle T_{SGS} \rangle$ is necessary for a successful LES (Völker *et al.* 2002). On the other hand, LESs with all SGS models underpredict the mean SGS dissipation $\langle \varepsilon_{SGS} \rangle$ (figure 3.5*f*), unlike the results of *a priori* test (figure 3.1*b*), indicating that an excellent prediction of $\langle \varepsilon_{SGS} \rangle$ is not a necessary condition for the accurate prediction of the turbulence statistics in LES of turbulent channel flow, as also reported by Park *et al.* (2006).

Figure 3.6 shows the instantaneous vortical structures identified by the isosurfaces of $\lambda_2 = -0.005 u_\tau^4 / \nu^2$ (Jeong & Hussain 1995). As compared to the flow field from DNS, the arches of the hairpin-like vortices disappear in the fDNS flow field, caused by the larger filter size in x direction ($\Delta_x^+ \approx 70$) than the diameter of the arch ($d^+ \approx 20$) (Park *et al.* 2006). The instantaneous flow fields from LESs with DSM and NN1 are similar to that of fDNS, whereas more vortical structures are observed from no SGS model due to insufficient dissipation. Since NN1 produces the best results among the NN models considered, we provide the results from NN1 hereafter. Figure 3.7 shows one-dimensional en-

ergy spectra of the velocity fluctuations at $y^+ = 15$ and 30 from LES with NN1, together with those of fDNS and from LES with DSM. Overall agreements of the velocity spectra from NN1 with those of fDNS are very good, like those from DSM.

Figures 3.8 and 3.9 show the probability density function (PDF) of streamwise and wall-normal velocity fluctuations, respectively, at four different wall-normal locations. For the streamwise component, NN1 shows similar predictions for PDF to that of DSM, but this NN model has better performance for the wall-normal component than that of DSM. Figure 3.10 shows the skewness $S(\bar{u}_i')$ and flatness $F(\bar{u}_i')$ of the velocity fluctuations, where $S\left(\bar{u}_i'\right) = \left\langle (\bar{u}_i')^3 \right\rangle / \bar{u}_{i,rms}^3$ and $F\left(\bar{u}_i'\right) = \left\langle (\bar{u}_i')^4 \right\rangle / \bar{u}_{i,rms}^4$. Overall, both statistics from NN1 have good agreements with those of fDNS for the streamwise and spanwise components. For the skewness of wall-normal component, NN1 slightly overpredicts it near the wall. This overprediction, however, is not significant to be detected in the PDF near the wall. In the case of the flatness of wall-normal component, NN1 shows better performance than that of DSM, as expected by PDF in figure 3.9.

Now, we apply NN1 to a turbulent channel flow at a higher Reynolds number of $Re_b = 27600$ ($Re_\tau = 723$ from DNS). LES is conducted at nearly the same resolution in wall units as that of trained data at $Re_\tau = 178$ (see table 3.2). The predictions of Re_τ from NN1 and DSM are excellent, showing about 0.8% and 2.2% errors, respectively, while the error from no SGS model is about 6%. Figures 3.11 and 3.12 show the turbulence statistics and energy spectra from LES723 with NN1, respectively, together with those of fDNS and from LESs with DSM and no SGS model. As shown, NN1 accurately predicts the turbulence statistics and energy spectra even at higher Reynolds number, even though the training is performed at a lower Reynolds number of 178. This result indicates that an NN-based SGS model trained at a lower Reynolds number flow maintains

their prediction performance for a higher Reynolds number flow, once the grid resolution in wall units is kept to be nearly the same (Gamahara & Hattori 2017).

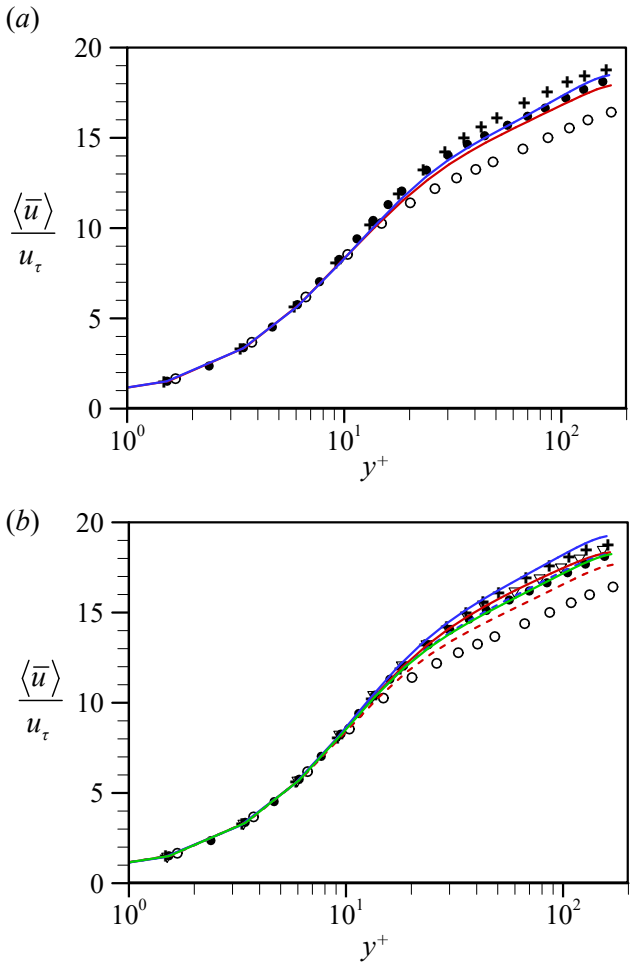

FIGURE 3.4. Mean velocity profiles from LES178 (*a posteriori* test): (*a*) without clipping the backscatter; (*b*) with clipping the backscatter. ●, fDNS; —, NN1; —, NN2; - - -, NN3; - - -, NN4; —, NN5; +, DSM; ▽, SSM; ○, no SGS model. LESs with NN3 - NN5 and SSM without clipping diverged.

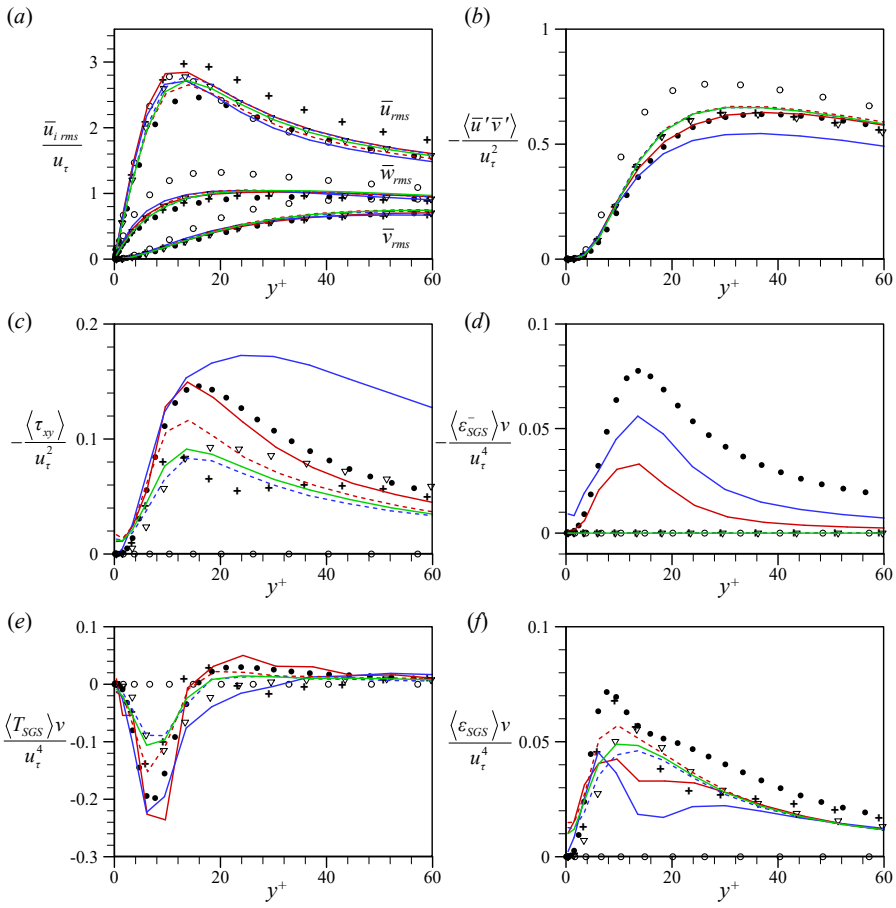

FIGURE 3.5. Turbulence statistics from LES178 (*a posteriori* test): (*a*) rms velocity fluctuations; (*b*) Reynolds shear stress; (*c*) mean SGS shear stress; (*d*) mean backscatter; (*e*) mean SGS transport; (*f*) mean SGS dissipation. ●, fDNS; —, NN1; —, NN2; - - -, NN3; - - -, NN4; —, NN5; +, DSM; ▽, SSM; ○, no SGS model. Note that the results of NN3 - NN5 and SSM are obtained with clipping the backscatter.

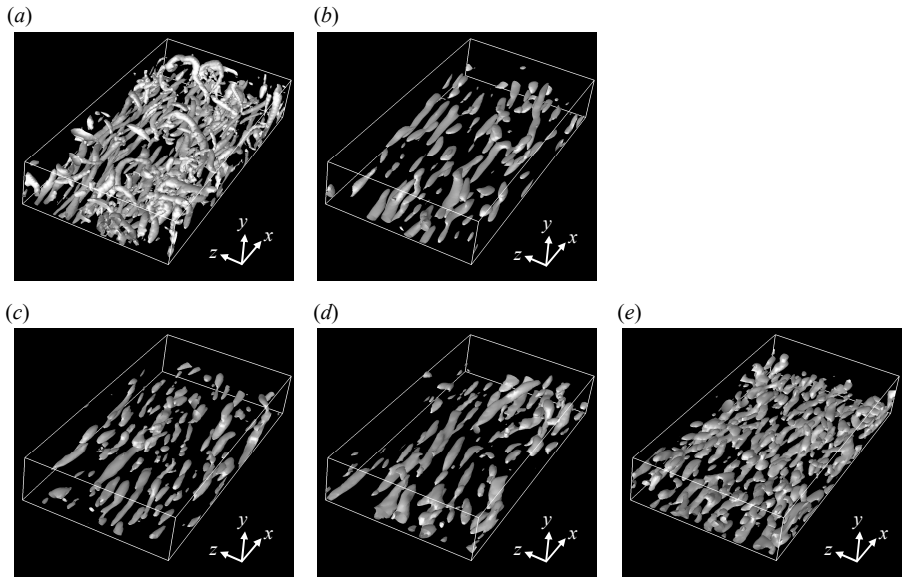

FIGURE 3.6. Instantaneous vortical structures from LES178 (*a posteriori* test): (*a*) DNS; (*b*) fDNS; (*c*) NN1; (*d*) DSM; (*e*) no SGS model. For the visual clarity, the vortical structures from fDNS and LES are plotted at the same grid resolutions in x and z directions as those of DNS by padding high wavenumber components of the velocity with zeros.

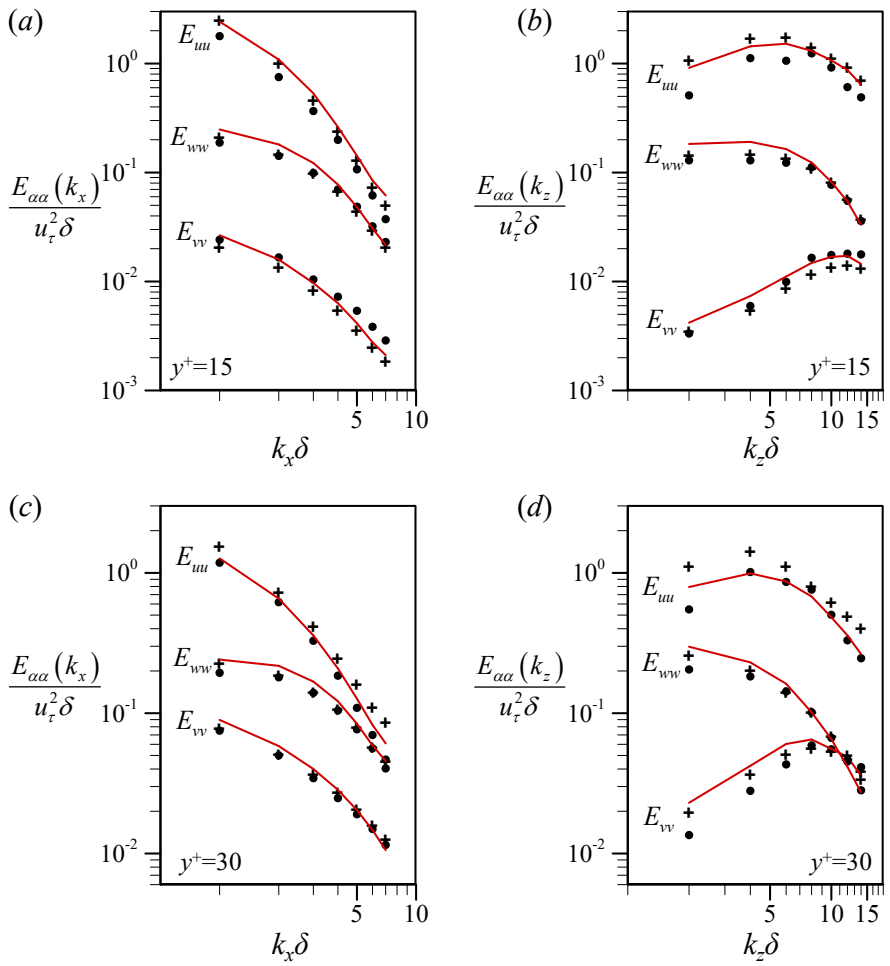

FIGURE 3.7. One-dimensional energy spectra of the velocity fluctuations at $y^+ = 15$ and 30 from LES178 (*a posteriori* test): (a, c) streamwise wavenumber; (b, d) spanwise wavenumber. ●, fDNS; —, NN1; +, DSM.

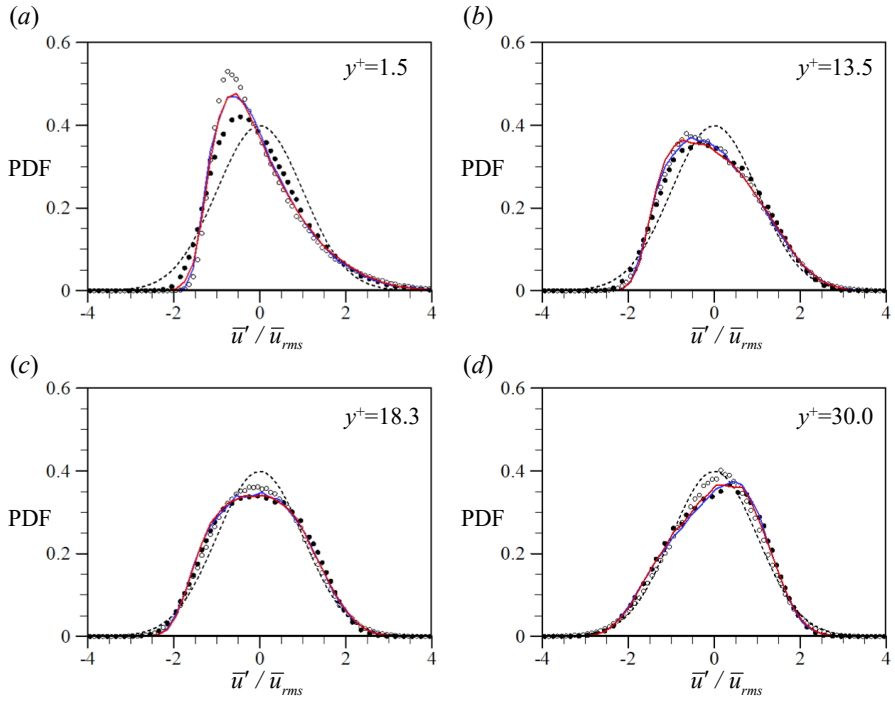

FIGURE 3.8. Probability density function of the streamwise velocity fluctuation from LES178 (*a posteriori* test): (*a*) $y^+ = 1.5$; (*b*) $y^+ = 13.5$; (*c*) $y^+ = 18.3$; (*d*) $y^+ = 30$. ●, fDNS; ○, no SGS model; ——, NN1; ——, DSM; - - -, Gaussian distribution.

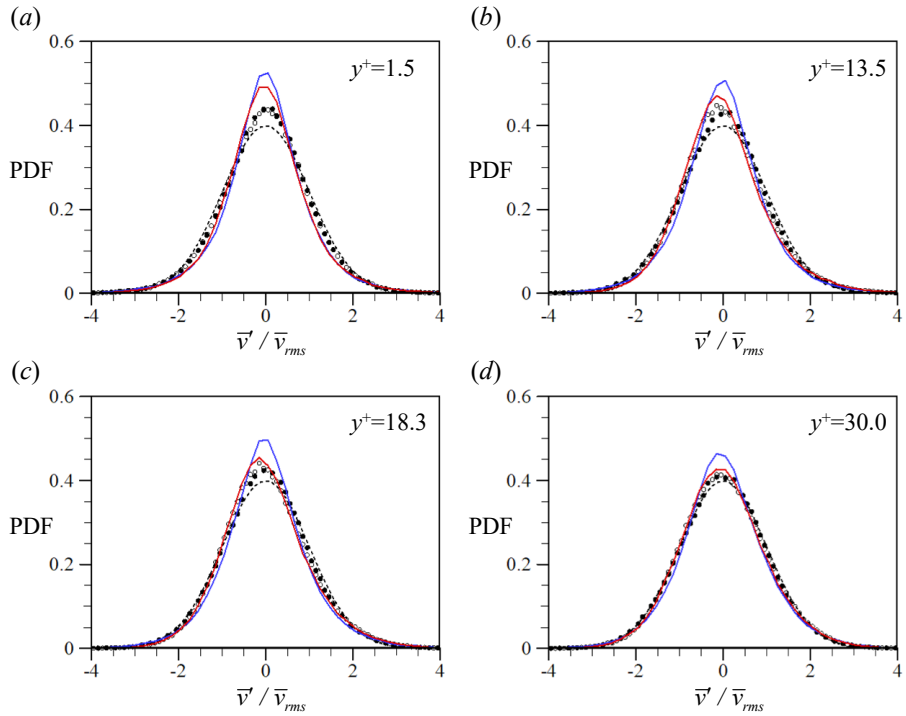

FIGURE 3.9. Probability density function of the wall-normal velocity fluctuation from LES178 (*a posteriori* test): (*a*) $y^+ = 1.5$; (*b*) $y^+ = 13.5$; (*c*) $y^+ = 18.3$; (*d*) $y^+ = 30$. ●, fDNS; ○, no SGS model; —, NN1; —, DSM; - - -, Gaussian distribution.

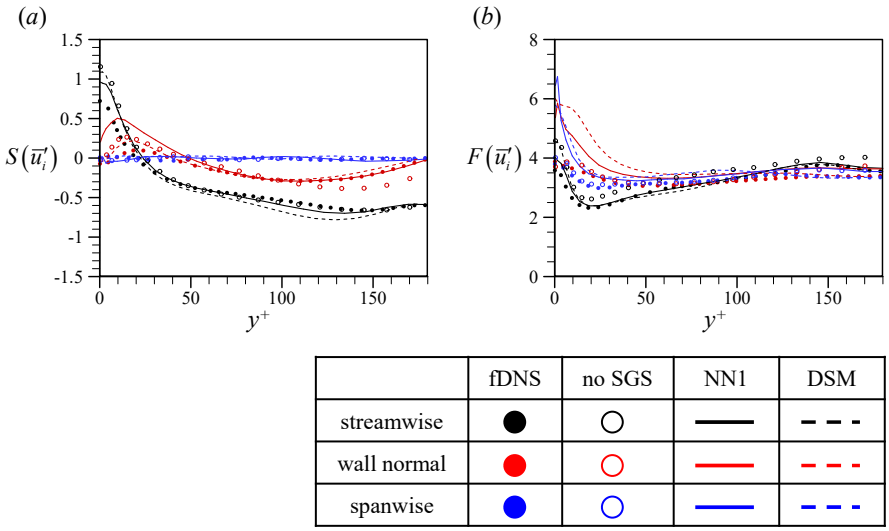

FIGURE 3.10. Skewness and flatness of the velocity fluctuations from LES178 (*a posteriori* test): (*a*) skewness; (*b*) flatness.

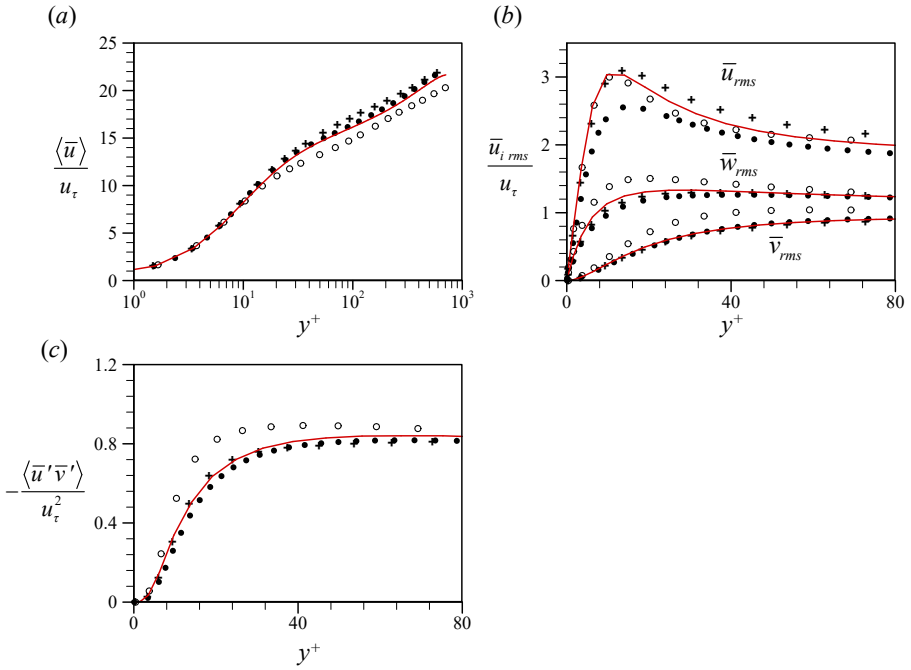

FIGURE 3.11. Turbulence statistics from LES723 (*a posteriori* test): (*a*) mean velocity; (*b*) rms velocity fluctuations; (*c*) Reynolds shear stress. ●, fDNS; —, NN1; +, DSM; ○, no SGS model.

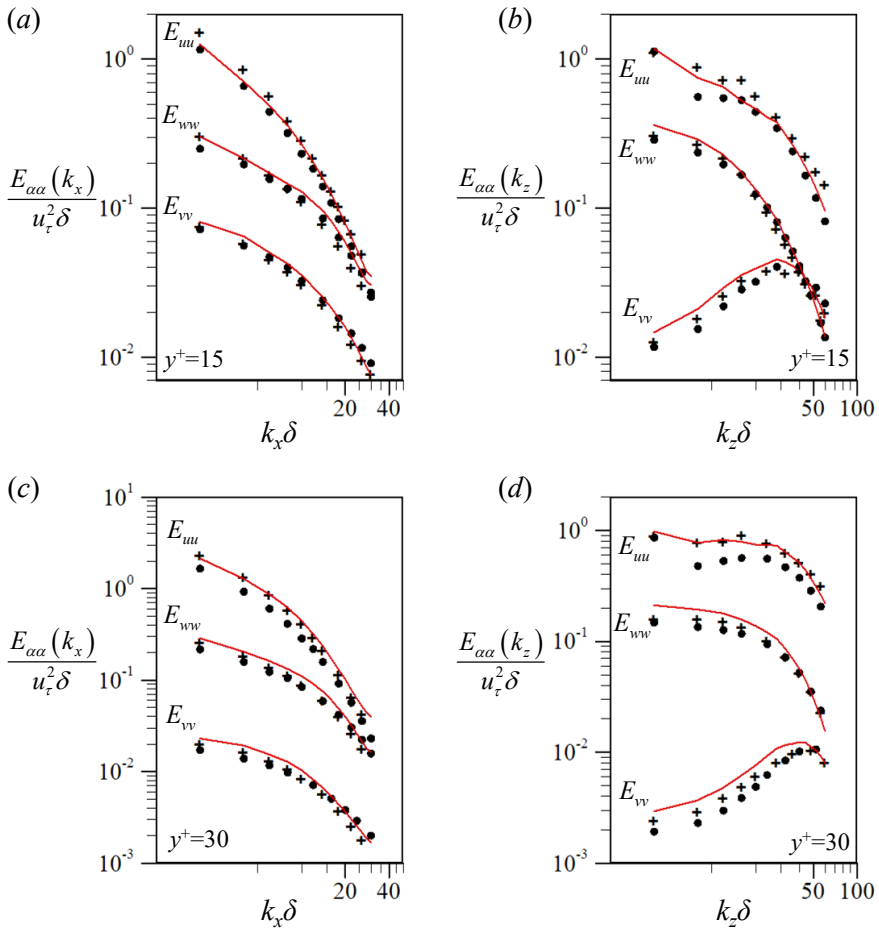

FIGURE 3.12. One-dimensional energy spectra of the velocity fluctuations at $y^+ = 15$ and 30 from LES723 (*a posteriori* test): (a, c) streamwise wavenumber; (b, d) spanwise wavenumber. ●, fDNS; —, NN1; +, DSM.

case	Re_b	(L_x, L_z)	(N_x, N_z, N_y)	$(\Delta x^+, \Delta z^+)$
LES178	5600	$(2\pi\delta, \pi\delta)$	(16, 16, 49)	(69.9, 35.0)
LES178c	5600	$(2\pi\delta, \pi\delta)$	(12, 12, 49)	(93.2, 46.6)
LES178f	5600	$(2\pi\delta, \pi\delta)$	(24, 24, 49)	(46.6, 23.3)
LES723	27600	$(\pi\delta, 0.5\pi\delta)$	(32, 32, 97)	(71.0, 35.5)

TABLE 3.2. Computational parameters of LES. Here, the computations are performed at constant mass flow rates (i.e., $Re_b = 5600$ and 27600). $\Delta y^+_{min} = 0.4$ for all simulations, and Δy^+_{min}, Δx^+ and Δz^+ in this table are computed with u_τ from DNS (table 2.2).

case	SGS model	Re_τ (w/o clipping)	Re_τ (with clipping)
LES178	NN1	181	175
	NN2	177	170
	NN3	diverged	183
	NN4	diverged	177
	NN5	diverged	178
	DSM	174	-
	SSM	diverged	176
	no	195	-
LES178c	NN1	175	175
	DSM	171	-
	no	190	-
LES178f	NN1	192	176
	DSM	177	-
	no	193	-
LES723	NN1	729	-
	DSM	707	-
	no	763	-

TABLE 3.3. Re_τ's ($Re_\tau = u_\tau \delta / \nu$) from LES.

3.3. LES with a grid resolution different from that of trained data

We test the performance of NN1 when the grid resolution in LES is different from that of trained data. We consider two different grid resolutions (LES178c and LES178f) as listed in table 3.2. LESs with NN1 are conducted without and with clipping the backscatter, respectively, to examine how the clipping affects the turbulence statistics for the cases with different resolutions. With LES178c, Re_τ is well predicted with and without clipping, whereas Re_τ is overpredicted with LES178f by about 8% without clipping but becomes closer to that of DNS with clipping (table 3.3). Predictions of Re_τ by DSM are not very good with coarser grids but become very good with denser grids, whereas no SGS model overpredicts Re_τ.

Figures 3.13 and 3.14 show the changes in the turbulence statistics from NN1 due to different grid resolutions, LES178c and LES178f, respectively, together with the statistics from fDNS and LES with DSM. When the grid resolution is coarser (LES178c) than that of trained data, NN1 predicts the mean velocity quite well, but significantly overpredicts the rms velocity fluctuations and Reynolds shear stress, which is similar to the results from DSM. The backscatter clipping does not improve the results. When the grid resolution is finer (LES178f) than that of trained data, NN1 without clipping significantly underpredicts the mean velocity due to the increased wall-shear velocity (Re_τ), but reasonably predicts the rms velocity fluctuations and Reynolds shear stress. Since NN1 is trained with $\bar{S}_{ij}$ and τ_{ij} at a given grid resolution, it provides a (trained) amount of energy transfer between the larger and smaller scales than the grid size. Although LES178f is performed at a finer grid resolution, NN1 still provides an amount of energy transfer trained at a coarser grid resolution. This may cause the increase in the amount of energy transfer and accordingly in the wall-shear velocity. On the other hand, when the grid resolution is coarser than that of trained

data, the trained amount of energy transfer given to the grid scale is smaller than the real one. For this reason, with clipping the backscatter, changes in the turbulence statistics including the mean velocity are notable for LES178f but not for LES178c.

From this result, it is clear that the NN-based LES requires a special treatment when the grid resolution is different from that of trained data. So, we consider an NN1 trained by two fDNS datasets from two different filter sizes with the input and output variables of $\bar{S}_{ij}$ and τ_{ij}. Here, we do not include the filter size as an additional input variable. Table 3.4 shows various NN1's considered in the present study. NN_{16} was already tested by LES178c and LES178f. NN_{12} and NN_{24} are trained using fDNS datasets having the same grid resolutions as those of LES178c and LES178f, respectively. On the other hand, $\mathrm{NN}_{8,16}$ is trained by both fDNS datasets with two filters corresponding to larger and smaller sizes ($N = 8$ and 16) than the grid resolution in LES178c ($N = 12$), and $\mathrm{NN}_{16,32}$ is trained by two fDNS datasets with $N = 16$ and 32 ($N = 24$ for LES178f), respectively.

We conduct LES178c's with NN_{12} and $\mathrm{NN}_{8,16}$, and LES178f's with NN_{24} and $\mathrm{NN}_{16,32}$, respectively, and compare the results with those of fDNS and from LESs with NN_{16} and DSM. All LESs with NNs are conducted without clipping the backscatter. Figure 3.15 shows the results of LES178c's. As shown, LES with $\mathrm{NN}_{8,16}$ provides much more accurate predictions of the rms velocity fluctuations and Reynolds shear stress than those from NN_{16} and DSM, showing the performance almost similar to that from NN_{12}. In the case of LES178f (figure 3.16), $\mathrm{NN}_{16,32}$ shows better prediction performance for the mean velocity, rms velocity fluctuations, and Reynolds shear stress than those from NN_{16}, and has similar predictions to those from NN_{24}. We have also tested $\mathrm{NN}_{8,16}$ for LES178f ($N = 24$) and $\mathrm{NN}_{16,32}$ for LES178c ($N = 12$), respectively. In these cases, LESs

with $NN_{8,16}$ and $NN_{16,32}$ do not show better performance than that with NN_{16}. Therefore, when the resolution in LES is not similar to that of trained data, it is suggested that the datasets having two different resolutions, coarser and finer than that of LES, should be constructed and used to train an NN for successful LES.

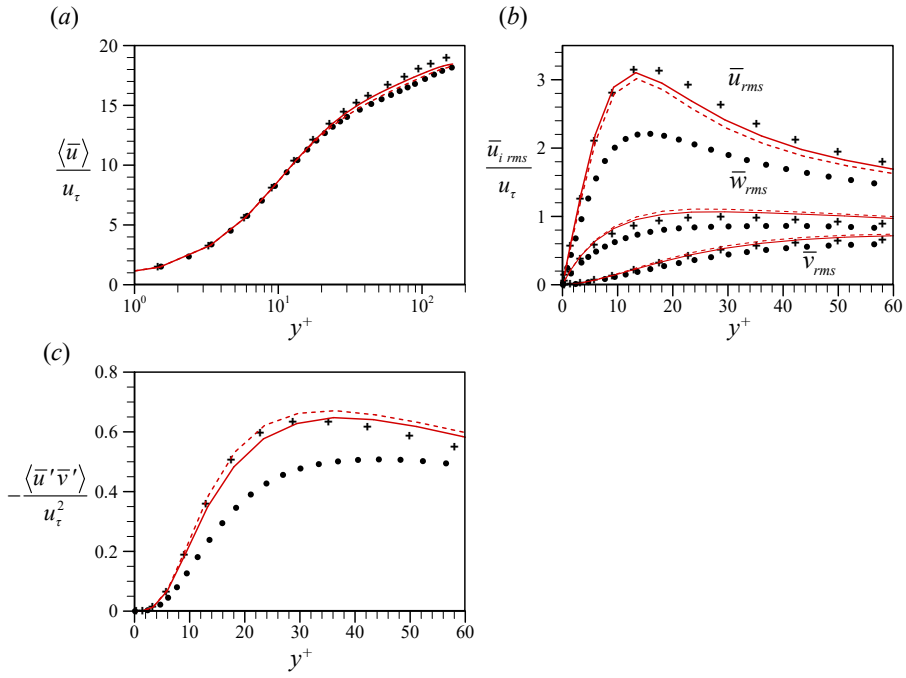

FIGURE 3.13. Changes in the turbulence statistics due to different grid resolution (LES178c) (*a posteriori* test): (*a*) mean velocity; (*b*) rms velocity fluctuations; (*c*) Reynolds shear stress. ●, fDNS; ——, NN1 without clipping the backscatter; - - -, NN1 with clipping the backscatter; +, DSM.

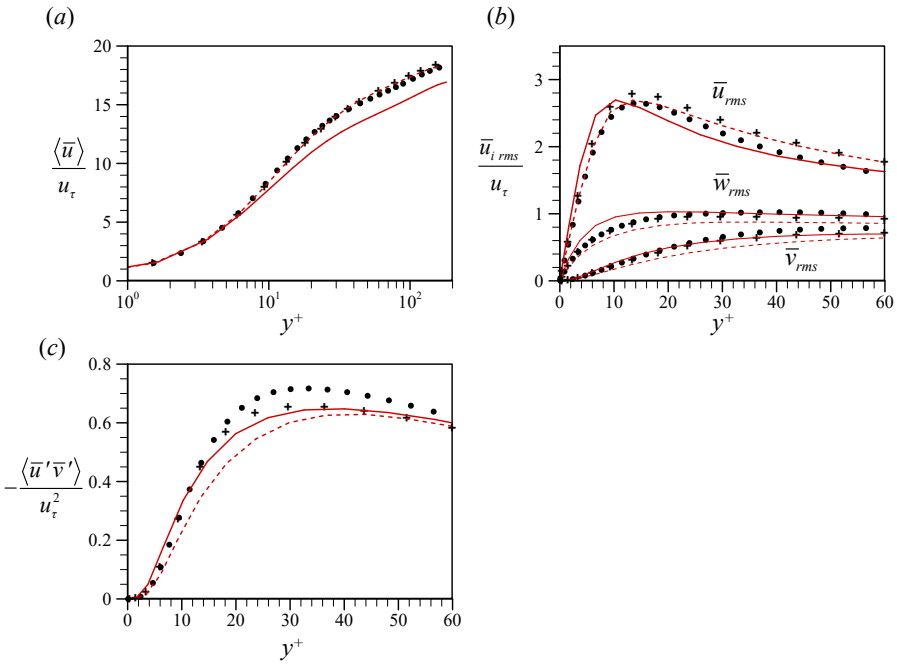

FIGURE 3.14. Changes in the turbulence statistics due to different grid resolution (LES178f) (*a posteriori* test): (*a*) mean velocity; (*b*) rms velocity fluctuations; (*c*) Reynolds shear stress. ●, fDNS; —, NN1 without clipping the backscatter; - - -, NN1 with clipping the backscatter; +, DSM.

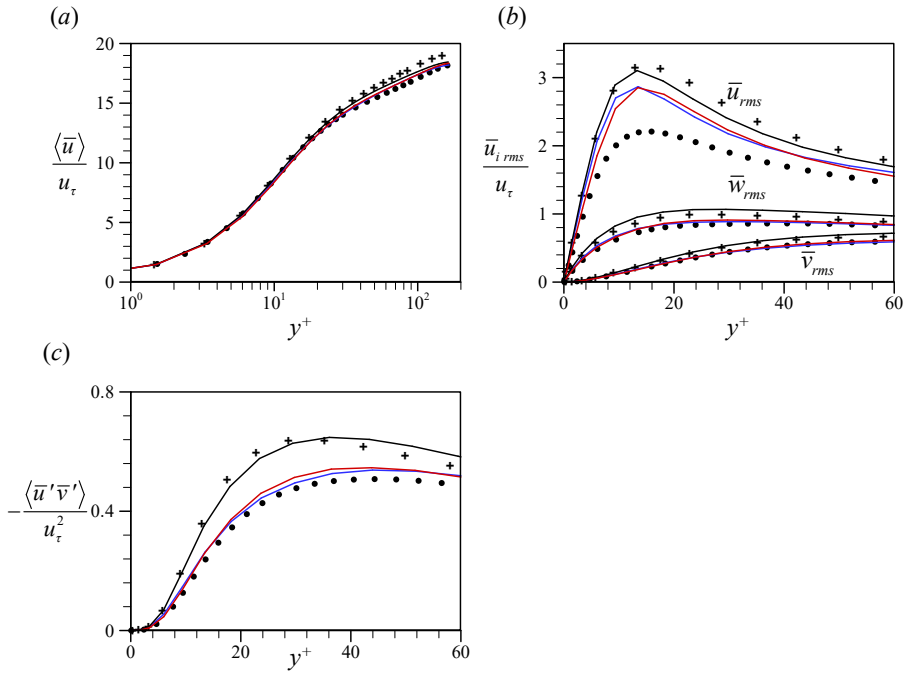

FIGURE 3.15. Turbulence statistics from LES178c (*a posteriori* test): (*a*) mean velocity; (*b*) rms velocity fluctuations; (*c*) Reynolds shear stress. ●, fDNS; —, NN_{16}; —, NN_{12}; —, $NN_{8,16}$; +, DSM.

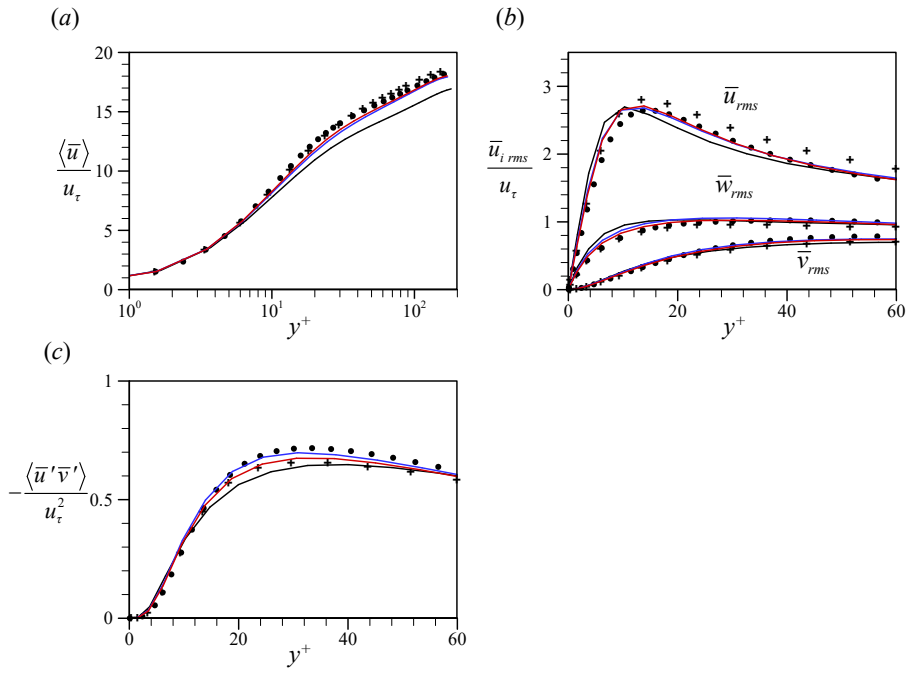

FIGURE 3.16. Turbulence statistics from LES178f (*a posteriori* test): (*a*) mean velocity; (*b*) rms velocity fluctuations; (*c*) Reynolds shear stress. ●, fDNS; —, NN_{16}; —, NN_{24}; —, $NN_{16,32}$; +, DSM.

NN1 model	fDNS(s) for trained data	LES(s)
NN_{16}	$fDNS_{16}$	LES178c and LES178f
NN_{12}	$fDNS_{12}$	LES178c
$NN_{8,16}$	$fDNS_8$ and $fDNS_{16}$	LES178c
NN_{24}	$fDNS_{24}$	LES178f
$NN_{16,32}$	$fDNS_{16}$ and $fDNS_{32}$	LES178f

TABLE 3.4. NN1 trained with different fDNS dataset(s). Here, $fDNS_N$ denotes the filtered DNS data with the number of grid points N ($= N_x = N_z$). Note that the numbers of grid points ($N_x \times N_z$) for LES178c and LES178f are 12×12 and 24×24, respectively, as listed in table 3.2.

Chapter 4

Conclusions

In the present study, we applied a fully connected neural network (NN) to the development of a subgrid-scale (SGS) model of predicting the SGS stresses for a turbulent channel flow, and conducted *a priori* and *a posteriori* tests to estimate its prediction performance. Five different NNs with different input variables were trained with filtered DNS data at $Re_\tau = 178$ using a spectral cut-off filter, where the input variables considered were the strain-rate tensor at single and multiple grid points (NN1 and NN3, respectively), velocity gradient tensor at single and multiple points (NN2 and NN4, respectively), and the velocity and wall-normal velocity gradient vectors at multiple points (NN5), respectively.

In *a priori* tests, the NN-based SGS models with the input variables at multiple grid points (NN3, NN4 and NN5) had higher correlations between the true and predicted SGS stresses, and better predicted backscatter than those with the input variables at single grid point (NN1 and NN2). However, actual LESs (i.e. *a posteriori* tests) with NN3 - NN5 were unstable unless a special treatment such as the backscatter clipping was taken. On the other hand, NN1 and NN2 showed excellent prediction performance without any *ad hoc* clipping or wall damping

function, although the correlations between the true and predicted SGS stresses were relatively low. Among NN models considered, NN1 (input of the strain-rate tensor at single grid point) performed best, and thus we applied NN1 (trained at $Re_\tau = 178$) to LES at a higher Reynolds number of $Re_\tau = 723$ with the same grid resolution in wall units, providing successful results. Finally, we applied NN1 to LESs at $Re_\tau = 178$ with coarser and finer grid resolutions, respectively. Although the results were generally good as compared to those from LES with the dynamic Smagorinsky model (DSM), they clearly showed a limitation in accurately predicting the turbulence statistics when LES was conducted with a resolution different from that used for training NN. To overcome this limitation, NN1 was trained by filtered DNS datasets with two filter sizes (larger and smaller than the grid size in LES), providing a successful result. Therefore, once multiple filtered datasets with various filter sizes are constructed and used to train an NN, one may expect a successful NN-based LES for turbulent channel flow, even if the grid resolution at hand is different from those used to construct the NN.

Part II.

Modeling of the subgrid-scale stress with a neural network: application to turbulent flow over a backward-facing step

Chapter 1

Introduction

Turbulent flow over a backward-facing step (BFS) contains a variety of flow phenomena such as flow separation, shear layer, reattachment, and turbulent boundary layer which are of great importance in many engineering applications. Because the flow is complex but the geometry is simple, extensive studies on the flow over BFS have been carried out both numerically and experimentally (Chen *et al.* 2018). In particular, as there are many available experimental data, this flow has been considered one of the most important problems in testing turbulence models (Eaton & Johnston 1981; Akselvoll & Moin 1995; Spalart *et al.* 2006).

In large eddy simulation (LES), the effect of subgrid-scale (SGS) flows on the dynamics of the resolved one is predicted through an SGS model. To test the performance of the SGS model, there have been studies that carried out LES of the flow over BFS. Friedrich & Arnal (1990) used the SGS model of Schumann (1975) for LES of BFS flow at $Re_h = 165000$ and $ER = 2$, where $Re_h(= U_0 h/\nu)$ is the step-height Reynolds number, U_0 is the free-stream velocity at the upstream of the step, h is the step height, $ER(= L_y/(L_y - h))$ is the expansion ratio, and L_y is the channel height at the downstream of the step.

They applied a wall-shear stress boundary condition at the wall, similar to that by Schumann (1975). The reattachment length X_r and turbulence intensities were not much agreed well with those found in experiments (Tropea 1982; Durst & Schmitt 1985), but they demonstrated the feasibility of LES for high-Reynolds-number separated flow. Note also that the discrepancy between the LES and the experiments appears to be due to the combination of coarse grid resolution, wall boundary condition, inflow condition, and the SGS model, not just a problem of the SGS model. Kobayashi *et al.* (1992) conducted the LES at $Re_h = 40000$ and $ER = 1.5$ using the Smagorinsky model (Smagorinsky 1963) with two different model coefficients ($C_s = 0.1$ and 0.15). Here, the Smagorinsky model is $\tau_{ij} = -2\nu_t \bar{S}_{ij}$ with $\nu_t = (C_s\bar{\Delta})^2\sqrt{2\bar{S}_{ij}\bar{S}_{ij}}$, where τ_{ij} is the SGS stress tensor, ν_t is the eddy viscosity, $\bar{S}_{ij}$ is the resolved strain rate tensor, and $\bar{\Delta}$ is the characteristic grid size. A two-layer wall function model was used for wall boundary condition. They showed that X_r was predicted better with $C_s = 0.15$ ($X_r = 8h$) than with $C_s = 0.1$ ($X_r = 9h$), where $X_r = 7h$ was found in the experiment (Kim *et al.* 1980). Neto *et al.* (1993) applied the structure-function SGS model by Métais & Lesieur (1992) to the LES at $Re_h = 6000$ ($ER = 5$) and at $Re_h = 38000$ ($ER = 1.67$), respectively. At solid walls, an approximate boundary condition based on the law of the wall was used. In the case of $Re_h = 38000$, the inflow boundary condition was imposed at the step edge, consisting of a mean velocity profile (found in the experiment by Eaton & Johnston 1980) with superimposed a white noise, whereas Friedrich & Arnal (1990) and Kobayashi *et al.* (1992) imposed a fully-developed turbulent flow at the upstream of the step by conducting a separate simulation of turbulent channel flow. The LES result from the structure-function SGS model did not agree much well with the experimental data (Eaton & Johnston 1980), but this SGS model predicted the turbulent kinetic energy and the Reynolds shear stress better than the Smagorin-

sky model with $C_s = 0.2$. Akselvoll & Moin (1995) conducted a wall-resolved LES at $Re_h = 5100$ ($ER = 1.2$) and $Re_h = 28000$ ($ER = 1.25$), respectively. They tested two different dynamic versions of the Smagorinsky model: one is the method by Germano *et al.* (1991) and Lilly (1992) and the other is the method by Ghosal *et al.* (1995), denoted as DSM and DLM hereafter, respectively. For $Re_h = 5100$, LES results with both SGS models showed an excellent agreement with the results of DNS (Le & Moin 1994) and experiment (Jovic & Driver 1994) for quantities such as skin-friction coefficient, mean velocity, and turbulence intensities. For $Re_h = 28000$, both SGS models provided also good predictions for the mean velocity and streamwise turbulence intensity compared to the experimental result (Adams *et al.* 1984). Later, the DSM has been the most widely used SGS model for the LES of BFS flow to investigate passive or active flow control methods (Kang & Choi 2002; Neumann & Wengle 2003), numerical schemes (Meri & Wengle 2002; Panjwani *et al.* 2009; Yang *et al.* 2020), and heat transfer characteristics (Avancha & Pletcher 2002; Keating *et al.* 2004). The DSM has been also the reference SGS model in developing a new SGS model. For example, Toschi *et al.* (2006), Inagaki *et al.* (2005) and Rasthofer & Gravemeier (2013) compared the performance of the new SGS model to that of the DSM for the LES of BFS flow, where the shear-improved Smagorinsky model, the mixed-time-scale model, and the multifractal model was the new SGS model in their studies, respectively.

Since there is no analytic solution for the SGS stress with resolved flow variables, the traditional SGS models have been based on certain simplifying assumptions or hypotheses. For example, the eddy viscosity SGS model is based on Boussinesq's hypothesis even though this hypothesis is almost not verified in real turbulence (Schmitt 2007). In this regard, an SGS model based on machine learning techniques, such as a neural network, has been developed so far.

The neural network (NN) is a nonlinear function that maps the SGS stress and the predefined input variables (e.g., strain rate), and the weight parameters of the NN are optimized by minimizing a given loss function such as the mean-squared error between the predicted and true SGS stresses. Therefore, the NN-based SGS model is intended to predict the realistic nature of SGS stress found in high-fidelity data better than the traditional SGS models. Previous studies have shown that an NN-based SGS model predicts the SGS stresses better than the traditional SGS models in *a priori* test (Wollblad & Davidson 2008; Gamahara & Hattori 2017; Beck *et al.* 2019; Pawar *et al.* 2020; Stoffer *et al.* 2020) and that LES using an NN-based SGS model has a good performance in predicting turbulence statistics such as the kinetic energy spectrum and velocity fluctuations (Maulik *et al.* 2018; Wang *et al.* 2018; Maulik *et al.* 2019; Zhou *et al.* 2019; Xie *et al.* 2019*a*,*b*,*c*, 2020*a*,*b*,*c*; Park & Choi 2021). However, the development of NN-based SGS model has been limited to two- and three-dimensional isotropic turbulence (Beck *et al.* 2019; Pawar *et al.* 2020; Stoffer *et al.* 2020; Maulik *et al.* 2018; Wang *et al.* 2018; Maulik *et al.* 2019; Zhou *et al.* 2019; Xie *et al.* 2019*a*,*b*,*c*, 2020*a*,*b*,*c*), and turbulent channel flow (Sarghini *et al.* 1999; Wollblad & Davidson 2008; Gamahara & Hattori 2017; Stoffer *et al.* 2020; Park & Choi 2021). Therefore, it is necessary to verify the performance of NN-based SGS model for the LES of more complex turbulent flows such as the flow over a backward-facing step.

To the best of our knowledge, there has been no attempt to conduct LES of BFS flow with an NN-based SGS model. Therefore, we apply the NN to the modeling of the SGS stress in the BFS flow, conduct LES of the BFS flow, and compare its performance with that of the traditional SGS model. Like the NN-based SGS model in part I, the NN in this part is the fully-connected neural network and predicts the SGS stress directly using the predefined input variables

which are strain rate or velocity gradient tensors. The input and target data are obtained by filtering the data from DNS of BFS flow at step-height Reynolds number of $Re_h = 5100$. The computational details for the DNS of BFS flow are presented in §2, together with the training details of the NN-based SGS model. In §3, the results from the LES of BFS flow at $Re_h = 5100$ are given, where the step-height Reynolds number and expansion ratio of the LES are the same as those of training data. Applications of the NN trained at $Re_h = 5100$ to LES of a higher Reynolds number flow ($Re_h = 24000$) and to LES of BFS flow having a passive control device are also discussed in §4, followed by conclusions in §5.

Chapter 2

Computational details

2.1. Outline of the NN-based SGS model

The governing equations for LES are the filtered Navier-Stokes and continuity equations:

$$\frac{\partial \bar{u}_i}{\partial x_i} - q = 0, \tag{2.1}$$

$$\frac{\partial \bar{u}_i}{\partial t} + \frac{\partial \bar{u}_i \bar{u}_j}{\partial x_j} = -\frac{\partial \bar{p}}{\partial x_i} + \frac{1}{Re_h}\frac{\partial^2 \bar{u}_i}{\partial x_j \partial x_j} - \frac{\partial \tau_{ij}}{\partial x_j} + f_i, \tag{2.2}$$

where t is time, $x_i(= x, y, z)$ is the Cartesian coordinates for the streamwise, wall-normal, and spanwise directions, respectively, $u_i(= u, v, w)$ are the corresponding velocity components, p is the pressure, the overbar denotes the filtering operation, and $\tau_{ij}(= \overline{u_i u_j} - \bar{u}_i \bar{u}_j)$ is the SGS stress tensor. In the present study, we use the immersed boundary method to describe the backward-facing step, and f_i and q are the momentum forcing and the mass source/sink terms, which are used to satisfy the no-slip boundary condition and the local mass conservation, respectively (for details, see Kim *et al.* 2001).

A fully-connected neural network is used to predict τ_{ij}, and we consider two different NNs having different input variables: NN with the input of filtered strain

rate $\bar{S}_{ij}$ (NN1) and NN with the input of filtered velocity gradient $\bar{\alpha}_{ij}$ (NN2), where $\bar{\alpha}_{ij} = \partial\bar{u}_i/\partial x_j$ and $\bar{S}_{ij} = 0.5(\bar{\alpha}_{ij} + \bar{\alpha}_{ji})$. Six components of $\bar{S}_{ij}$ and nine components of $\bar{\alpha}_{ij}$ at each grid point are the inputs to NN1 and NN2, respectively, and the output is six components of τ_{ij} at the same grid location. While it is possible to use those input variables at multiple grid points (Xie *et al.* 2019*c*, 2020*a*,*b*; Beck *et al.* 2019; Pawar *et al.* 2020; Park & Choi 2021), Park & Choi (2021) showed that the use of those inputs at multiple grid points provided unstable LES results in turbulent channel flow unless special treatment is applied to the predicted SGS stresses. Therefore, we only test those two inputs ($\bar{S}_{ij}$ and $\bar{\alpha}_{ij}$) at a grid point, considering the turbulent boundary layer at the upstream of step edge and at the downstream of the flow reattachment in the BFS flow.

The main hyperparameters of an NN are the numbers of hidden layers and neurons per hidden layer, N_{hl} and N_{nr}, respectively. We have conducted a parametric test for N_{hl} and N_{nr}, and the NN with $N_{hl} = 2$ and $N_{nr} = 32$ are used for LES of BFS flow (see §2.3). The database for training NN is obtained by filtering the instantaneous flow fields from DNS of BFS flow (see §2.2).

We also perform LES with the dynamic Smagorinsky model (Germano *et al.* 1991; Lilly 1992) to estimate the performance of the present NN-based SGS model. For the dynamic Smagorinsky model (DSM),

$$\tau_{ij} - \frac{1}{3}\tau_{kk}\delta_{ij} = -2\nu_t\bar{S}_{ij} = -2(C_s\bar{\Delta})^2\sqrt{2\bar{S}_{ij}\bar{S}_{ij}}\bar{S}_{ij},$$
$$(C_s\bar{\Delta})^2 = -\frac{1}{2}\frac{\langle L_{ij}M_{ij}\rangle_h}{\langle M_{ij}M_{ij}\rangle_h},$$
$$L_{ij} = \widetilde{\bar{u}_i\bar{u}_j} - \tilde{\bar{u}}_i\tilde{\bar{u}}_j,$$
$$M_{ij} = \left(\tilde{\Delta}/\bar{\Delta}\right)^2\left|\tilde{\bar{S}}\right|\tilde{\bar{S}}_{ij} - \widetilde{|\bar{S}|\bar{S}_{ij}}$$

where, $\bar{\Delta}$ and $\tilde{\Delta}$ ($\tilde{\Delta}/\bar{\Delta} > 1$) are the grid and test filter sizes, respectively, and $\langle\rangle_h$ denotes averaging in the homogeneous directions (spanwise direction in BFS

flow). Since the negative $(C_s\bar{\Delta})^2$ incurs the numerical instability (Akselvoll & Moin 1995), $(C_s\bar{\Delta})^2$ is forced to be zero wherever it is negative. The grid and test filter sizes are $\bar{\Delta}^2 = \bar{\Delta}_1\bar{\Delta}_3$ and $\tilde{\Delta}^2 = \tilde{\Delta}_1\tilde{\Delta}_3$, respectively, where $\bar{\Delta}_i$ and $\tilde{\Delta}_i$ are the grid and test filter sizes in each directions, respectively. The test filtering is conducted in both x and z directions using Simpson's rule, as suggested by Akselvoll & Moin (1995) who conducted LES of BFS flow at $Re_h = 5100, 28000$.

2.2. Details of DNS for training data

2.2.1. *Computational domain and grid spacing*

Figure 2.1 shows the schematic diagram of the computational domain used for the DNS of BFS flow, where the location of the step edge is $(x, y) = (0, h)$. The step-height Reynolds number Re_h and the expansion ratio ER are $Re_h = 5100$ and $ER = 1.2$, respectively. The BFS flow with those Re_h and ER has been widely used to test LES techniques (Akselvoll & Moin 1995; Kang & Choi 2002; Simons *et al.* 2002; Aider *et al.* 2007; Panjwani *et al.* 2009; Yang *et al.* 2020), since both DNS (Le *et al.* 1997) and experimental results (Jovic & Driver 1994) are available. Thus, we adopt this BFS flow for training and testing NN-based SGS models. The size of the computational domain is $-2.5 \leq x/h \leq 20$, $0 \leq y/h \leq 6$ and $0 \leq z/h \leq 4$, and the numbers of grid points used in DNS are $449 \times 193 \times 128$ in the streamwise, wall-normal and spanwise directions, respectively, where 70 and 64 computational cells are placed within $y < h$ and $x < 0$, respectively. Figure 2.2 shows the distribution of grid spacing in streamwise and wall-normal directions, and table 2.1 lists grid spacings in wall units. Non-uniform grid spacings are used in both the streamwise and wall-normal directions, where grids are dense near the wall. The uniform grid distribution is used in spanwise direction. The number of grid points in spanwise direction is twice that used in DNS by Le *et al.* (1997), since they pointed out that a higher

spanwise resolution was desirable to resolve the small-scale structures near the wall.

2.2.2. *Boundary conditions and numerical methods*

The inflow boundary condition at $x = -2.5h$ is the time series of fully-developed turbulent boundary-layer flow (TBL). To provide a realistic inlet turbulence, a separate DNS of TBL flow is conducted. With this inflow condition, a short inlet section (L_{xi}) could be used (Akselvoll & Moin 1995; Kang & Choi 2002), as compared to that used with a prescribed mean velocity and random fluctuations as the inflow (Le *et al.* 1997). The DNS of TBL flow is performed using the recycling method by Lund *et al.* (1998), where the inlet turbulent flow is generated using the velocity field at a downstream location based on empirical scaling laws. At the inlet of TBL simulation, $Re_\theta (= U_0\theta/\nu)$ and δ/h are approximately 670 and 1.25, where θ and δ are momentum and boundary layer thicknesses, respectively, and these parameters are similar to those of inflow in DNS by Le *et al.* (1997). The domain sizes for the DNS of TBL flow are $14.5h, 5h$ and $4h$ in streamwise, wall-normal and spanwise directions, respectively, and the recycling location is placed at $10.4h$ downstream of the inlet. The velocity fields at $7.5h$ downstream of inlet are stored in advance and provided in time at the inlet of the computational domain for the BFS flow.

The periodic boundary condition is used in the spanwise direction, and the no-slip boundary condition is used at the wall at ($y = 0$). The immersed boundary method by Kim *et al.* (2001) is used to satisfy the no-slip condition at the backward-facing step (gray colored in figure 2.1), i.e., the location of ($x \leq 0, y = h$) and ($x = 0, y \leq h$). At the upper boundary of the computational domain ($y = 6h$), the following no-stress condition is applied:

$$\frac{\partial u}{\partial y} = 0, v = 0, \frac{\partial w}{\partial y} = 0. \tag{2.3}$$

The boundary condition at the domain exit ($x = 20h$) is the convective boundary condition,

$$\frac{\partial u_i}{\partial t} + U_c \frac{\partial u_i}{\partial x} = 0, \tag{2.4}$$

where U_c is the plane-averaged streamwise velocity at the exit.

The governing equations of DNS for the backward-facing-step flow are the continuity and Navier-Stokes equations, i.e., the equations (2.1) and (2.2) without filtering operation and SGS stress term. A semi-implicit fractional step method is used to solve the governing equations, where a third-order Runge-Kutta and the Crank-Nicolson schemes are used for the convection and diffusion terms, respectively. For spatial derivatives, the second-order central difference scheme is used. we used the time step of $\Delta t = 0.002h/U_0$ which is similar to that used by Le *et al.* (1997). Initial flow fields for $400h/U_0$ are discarded, and then the flow fields are averaged over $400h/U_0$ to obtain the mean statistics.

2.2.3. *Filtered DNS flow fields*

A filtered flow variable $\bar{f}(x, y, z, t)$ based on the box filter is defined as

$$\bar{f}(x, y, z, t) = \frac{1}{\bar{\Delta}_1 \bar{\Delta}_2 \bar{\Delta}_3} \int_{-0.5\bar{\Delta}_3}^{0.5\bar{\Delta}_3} \int_{-0.5\bar{\Delta}_2}^{0.5\bar{\Delta}_2} \int_{-0.5\bar{\Delta}_1}^{0.5\bar{\Delta}_1} f\left(x + x', y + y', z + z', t\right) \mathrm{d}x' \mathrm{d}y' \mathrm{d}z', \tag{2.5}$$

where $f(x, y, z, t)$ is an unfiltered flow variable, $\bar{\Delta}_i$ is the filter width in each direction at the position of (x, y, z). To obtain filtered DNS (fDNS, hereafter) flow field, we first should set the filter width $\bar{\Delta}_i$, i.e., the distribution of grid spacings of the fDNS flow field. The number of grid points used for fDNS is $161 \times 57 \times 64$ in the streamwise, wall-normal and spanwise directions, respectively, where 24 and 40 computational cells are placed within $y < h$ and $x < 0$, respectively. The grid distributions of fDNS in streamwise and wall-normal directions are shown in figure 2.2, and grid spacings in wall units are given in table 2.1, together with

those used in previous LES studies. Note that the domain size of fDNS is the same as that of DNS.

Figure 2.3 shows the skin-friction coefficient C_f, the pressure coefficient C_p at the wall, and the mean streamwise velocity profiles. Here, C_f and C_p are defined as

$$C_f = \frac{\tau_w}{\frac{1}{2}\rho U_0^2}, \tag{2.6}$$

$$C_p = \frac{\langle p \rangle_{zt} - P_0}{\frac{1}{2}\rho U_0^2}, \tag{2.7}$$

respectively, where $\tau_w = \langle \mu \partial u/\partial y \rangle_{zt}$, $\langle \rangle_{zt}$ denotes averaging in time and z direction, and P_0 is a reference mean pressure. In the previous DNS (Le *et al.* 1997) and experiment (Jovic & Driver 1994), the reference pressure P_0 was the wall pressure at $x = -5h$, but this location does not exist in the present DNS. Therefore, P_0 in the present study is obtained so that C_p at $(x, y) = (-2h, h)$ is the same as that of previous DNS (Le *et al.* 1997). Figure 2.3 indicates that C_f, C_p and mean streamwise velocity have excellent agreements with those from previous DNS and experiment. Figure 2.4 shows the root-mean-square (rms) streamwise and wall-normal velocity fluctuations, and the Reynolds shear stress from DNS and fDNS, together with those from previous DNS and experiment. Those statistics from DNS have good agreement with those from previous studies (Jovic & Driver 1994; Le *et al.* 1997). In the case of fDNS, the magnitude of those statistics are reduced due to the filtering. For the Reynolds shear stress of fDNS, its maximum values are reduced by 17%, 14%, 14% and 22% at $x/h = 4, 6, 10$ and 19, respectively, compared to those from DNS. The order of magnitude of those reduction rates seems to be reasonable, as Akselvoll & Moin (1995) showed that the contribution of the SGS shear stress to the Reynolds shear stress was approximately 8-10% in LES of BFS flow at $Re_h = 5100$.

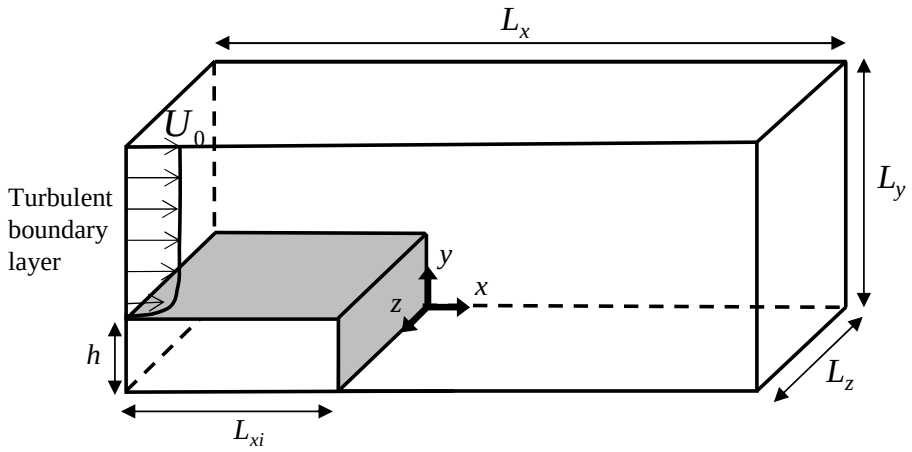

FIGURE 2.1. Computational domain for DNS of flow over a backward-facing step ($Re_h = 5100$, $ER = 2$).

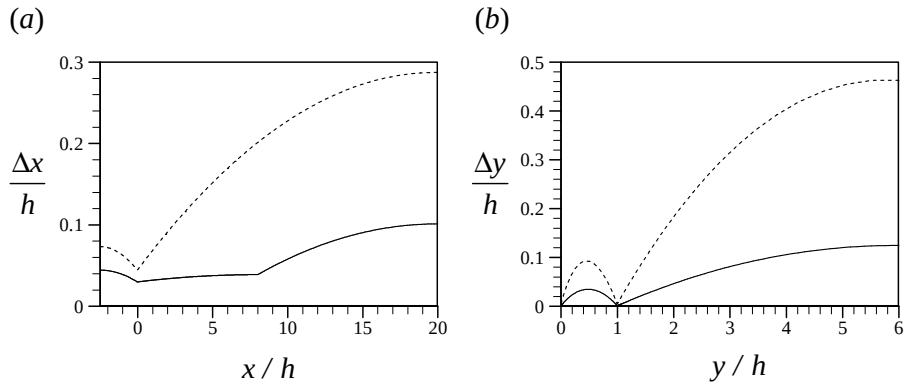

FIGURE 2.2. Grid spacing of DNS and fDNS (Re_h=5100): (*a*) streamwise direction; (*b*) wall-normal direction. ——, DNS; - - -, fDNS.

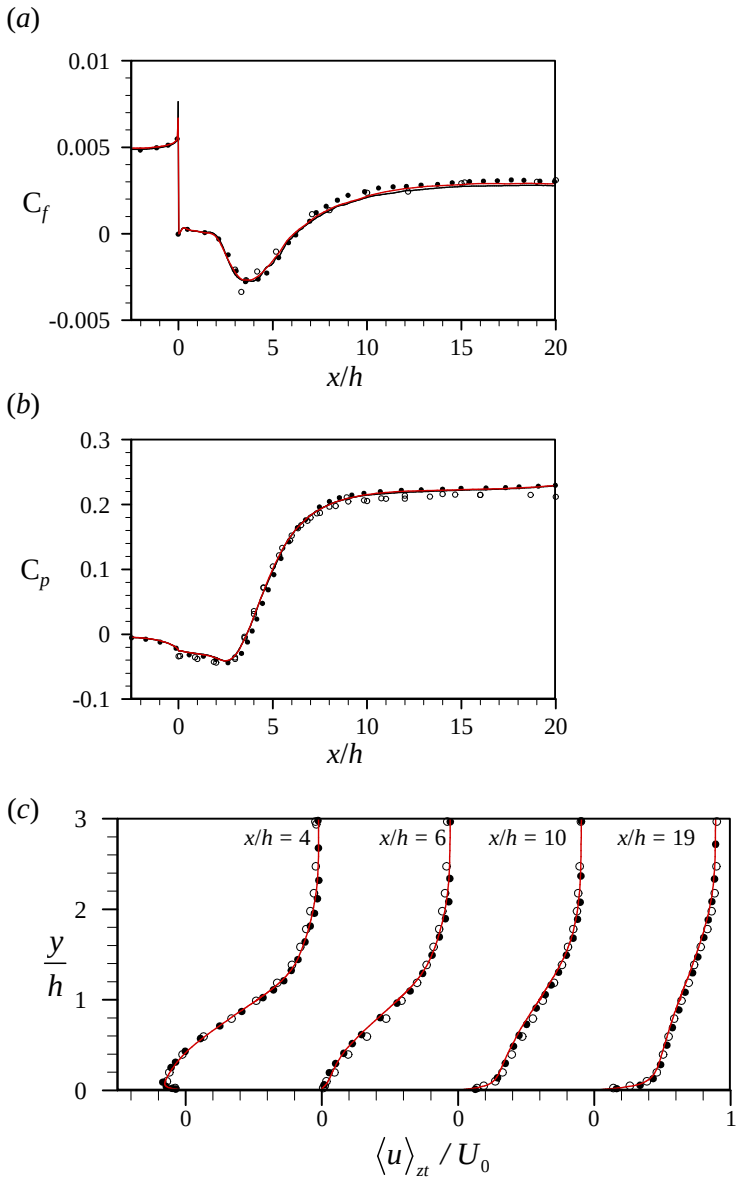

FIGURE 2.3. Results of DNS and fDNS (Re_h=5100): (*a*) skin-friction coefficient; (*b*) pressure coefficient at the wall; (*c*) mean streamwise velocity profiles at four different streamwise locations. ●, DNS (Le *et al.* 1997); ○, experiment (Jovic & Driver 1994); —, present DNS; —, present fDNS.

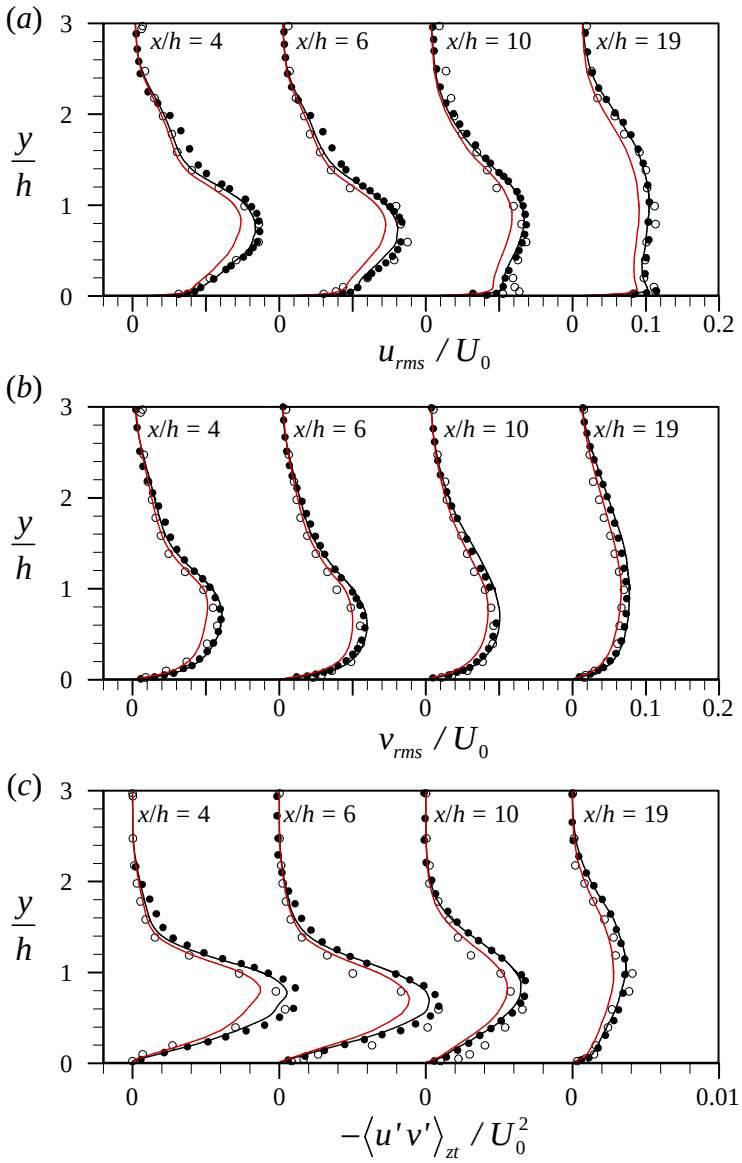

FIGURE 2.4. The rms streamwise and wall-normal velocity fluctuations (u_{rms} and v_{rms}, respectively) and the Reynolds shear stress from DNS and fDNS (Re_h=5100): (*a*) u_{rms}; (*b*) v_{rms}; (*c*) the Reynolds shear stress. ●, DNS (Le *et al.* 1997); ○, experiment (Jovic & Driver 1994); —, present DNS; —, present fDNS.

Case	Δx^+_{min}	Δx^+_{max}	Δy^+_{min}	Δy^+_{max}	Δz^+
present DNS	7.6	25.6	0.3	31.5	7.9
DNS (Le *et al.* 1997)	9.9	9.9	0.3	31.4	15.8
present fDNS	11.4	72.7	1.4	117.1	15.8
LES (Akselvoll & Moin 1995)	11.4	71.9	1.5	117.3	31.6
LES (Kang & Choi 2002)	11.4	72.3	1.4	117.0	15.8
LES (Simons *et al.* 2002)	11.4	71.1	1.5	117.8	31.6
LES (Aider *et al.* 2007)	4.0	66.7	1.3	50.5	16.9
LES (Yang *et al.* 2020)	39.5	39.5	4.6	75.9	31.6

TABLE 2.1. Grid spacings in wall units for DNS and fDNS (Re_h=5100), together with those used in previous DNS and LES studies. $\Delta x_i^+ = \Delta x_i u_\tau/\nu$, and the friction velocity u_τ at the inlet of the computational domain (DNS) is used ($u_\tau = 4.9619 \times 10^{-2} U_0$).

2.3. Training details and hyperparameter optimization

In this section, we describe the training details for an NN and the results of *a priori* test, in which the SGS stresses are predicted by NN1 and NN2 with the inputs from fDNS flow field of BFS flow at $Re_h = 5100$. We should mention that in *a priori* test, we do not focus on how well the NN works, but rather on whether the performance of the NN converges with varying N_{hl} and N_{nr}, because the performance of an SGS model in *a priori* test is not consistent with that in actual LES (Park *et al.* 2005).

The fDNS flow fields with the time interval of $5h/U_0$ are used to collect training data $(\bar{S}_{ij}, \bar{\alpha}_{ij}, \tau_{ij})$. It has been observed that the formation and detachment of coherent structures from the step edge causes the periodic oscillation in the reattachment location (Eaton & Johnston 1980; Le *et al.* 1997), and the frequency corresponding to this oscillation is approximately $0.06U_0/h$ (Le *et al.* 1997). Therefore, the sampling time interval of $5h/U_0$ corresponds to about a third of this oscillation period. The training data are collected at every 8th grid point in z direction (corresponding to $\Delta z = 0.5$) to exclude highly correlated data, and at all grid points in x and y directions from 40 instantaneous fDNS fields, excluding grid points inside the immersed boundary. The number of grid points outside the immersed boundary is 8,000 in one xy-plane, so the number of training data is 2,560,000 ($40 \times 8000 \times 64/8$). We have also tested 60 fDNS fields for training NN's (3,840,000 data), but their prediction performance for the SGS stresses is not further improved (see below), so the number of training data used is sufficient for the present NN's. All flow variables in training data are non-dimensionalized with U_0 and h.

The weight parameters of NN are optimized to minimize the loss function

L, defined as

$$L = \frac{1}{2N_b}\frac{1}{6}\sum_{j\geq i}\sum_{n=1}^{N_b}\left(\tau_{ij,n}^{\mathrm{fDNS}} - \tau_{ij,n}^{\mathrm{NN}}\right)^2 + 0.005\sum_{o} w_o^2, \qquad (2.8)$$

where $\tau_{ij,\,n}^{\mathrm{fDNS}}$ and $\tau_{ij,\,n}^{\mathrm{NN}}$ is the SGS stresses obtained from fDNS and predicted by the NN, respectively, N_b is the number of minibatch data (8000 in this study), and w_o denotes the components of trainable weight parameters in the NN. Note that $N_b = 8000$ is the same as the number of training data in one xy-plane of fDNS flow field. We use a rectified linear unit (Relu; Nair & Hinton 2010) as the activation function, and use a batch normalization (Ioffe & Szegedy 2015). An adaptive moment estimation (Kingma & Ba 2014) is applied to update the trainable parameters, and the gradients of the loss function with respect to those parameters are calculated through the chain rule of derivatives (Rumelhart *et al.* 1986; LeCun *et al.* 2015).

In the previous studies, a wide range of N_{nr} was used with $N_{hl} = 1$ (Gamahara & Hattori 2017; Maulik & San 2017; Maulik *et al.* 2018; Zhou *et al.* 2019) or $N_{hl} = 2$ (Sarghini *et al.* 2003; Wollblad & Davidson 2008; Vollant *et al.* 2017; Wang *et al.* 2018; Maulik *et al.* 2019; Xie *et al.* 2019*a*,*b*,*c*, 2020*a*,*c*; Park & Choi 2021), but the order of N_{nr} was roughly $N_{nr} = O(10) - O(10^3)$. We test both NN1 and NN2 for different N_{hl} and N_{nr}, where $N_{hl} = 1, 2, 3$ and $N_{nr} = 16, 32, 64, 128$ are considered. Here, we present only four representative cases for clarity, which are given in table 2.2.

Figure 2.5 shows the variations of the training error ϵ_τ with the epoch for NN1 and NN2, where ϵ_τ is defined as

$$\epsilon_\tau = \frac{1}{2\mathrm{N}_{\mathrm{data}}}\frac{1}{6}\sum_{j\geq i}\sum_{n=1}^{\mathrm{N}_{\mathrm{data}}}\left(\tau_{ij,n}^{\mathrm{fDNS}} - \tau_{ij,n}^{\mathrm{NN}}\right)^2. \qquad (2.9)$$

Here, one epoch denotes one sweep through the entire training dataset (Hastie *et al.* 2009), and $\mathrm{N}_{\mathrm{data}}$ is the number of data used to obtain ϵ_τ. The errors ϵ_τ

nearly converge with 100 epochs for both NN1 and NN2 regardless of N_{hl} and N_{nr}. The errors from the training and test datasets converge to nearly the same value, indicating that severe overfitting is not observed for both NN1 and NN2 for all cases considered. Since ϵ_τ alone does not represent the prediction performance of the NN, we investigate the mean SGS shear stress and dissipation. Figures 2.6 and 2.7 show the mean SGS shear stress $\langle \tau_{xy} \rangle_{zt}$ and dissipation $\langle \varepsilon_{SGS} \rangle_{zt}$, respectively, predicted by NN1 and NN2 with different N_{hl} and N_{nr}, where $\varepsilon_{SGS} = -\tau_{ij}\bar{S}_{ij}$. Here, 600 fDNS fields with the time interval of $0.5h/U_0$ are used for obtaining those statistics. Results show that one hidden layer (case CS1) even with $N_{nr} = 128$ is not sufficient for showing converged prediction performance. For $N_{hl} = 2$, performance of NN1 and NN2 with $N_{hl} = 16$ (case CS2) is not converged also. On the other hand, for both NN1 and NN2, $N_{hl} = 2$ and $N_{nr} = 32$ (case CR) are sufficient for showing converged prediction performance, as the performance of case CL is almost similar to that of case CR. Note that the case CL has more N_{hl}, N_{nr} and training data than those used for case CR. Therefore, two hidden layers with 32 neurons per hidden layer are used for both NN1 and NN2 in the present study.

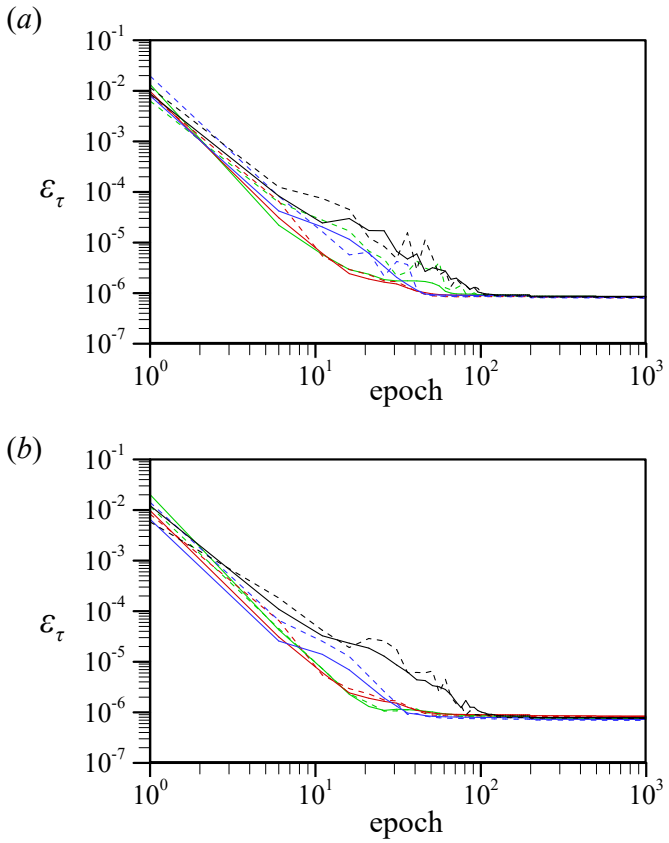

FIGURE 2.5. Training error ϵ_τ by different N_{hl} and N_{nr}: (*a*) NN1; (*b*) NN2. ——— and - - -, CS1; ——— and - - -, CS2; ——— and - - -, CL; ——— and - - -, CR. The solid and dashed lines are ϵ_τ for training and test datasets.

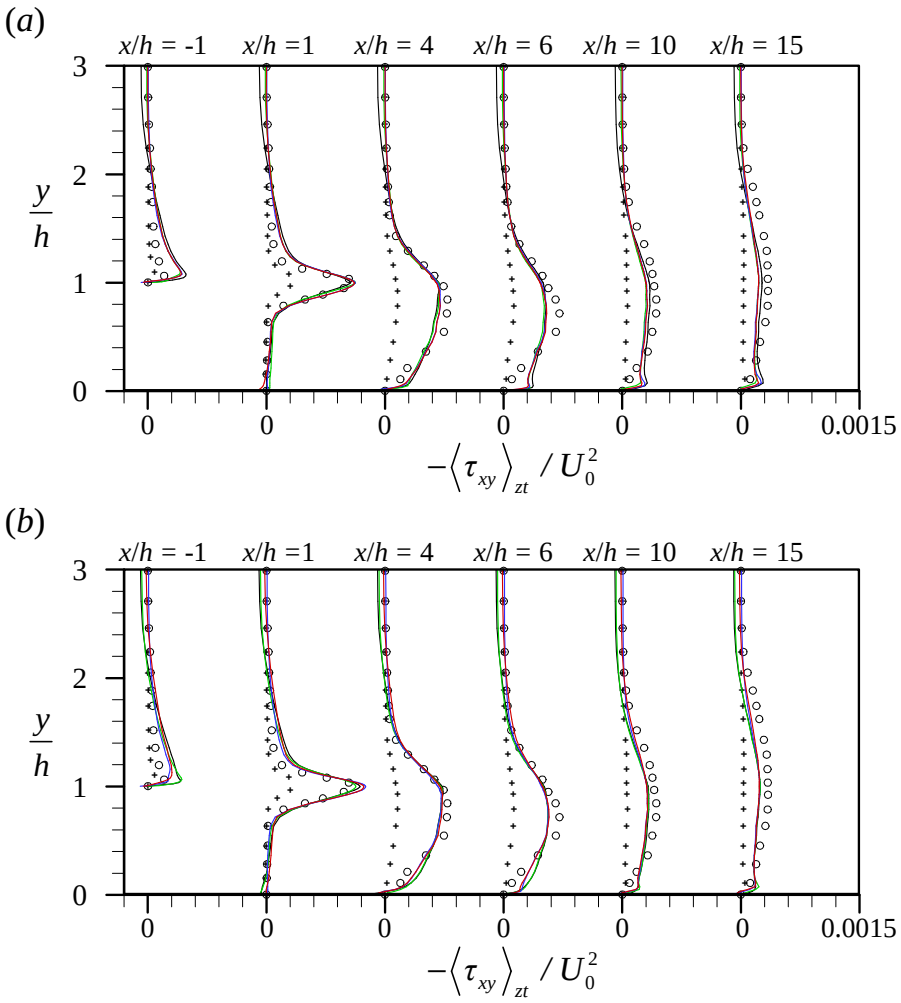

FIGURE 2.6. Mean SGS shear stress by different N_{hl} and N_{nr} (*a priori test*): (*a*) NN1; (*b*) NN2. ○, fDNS; +, DSM; —, CS1; —, CS2; —, CL; —, CR.

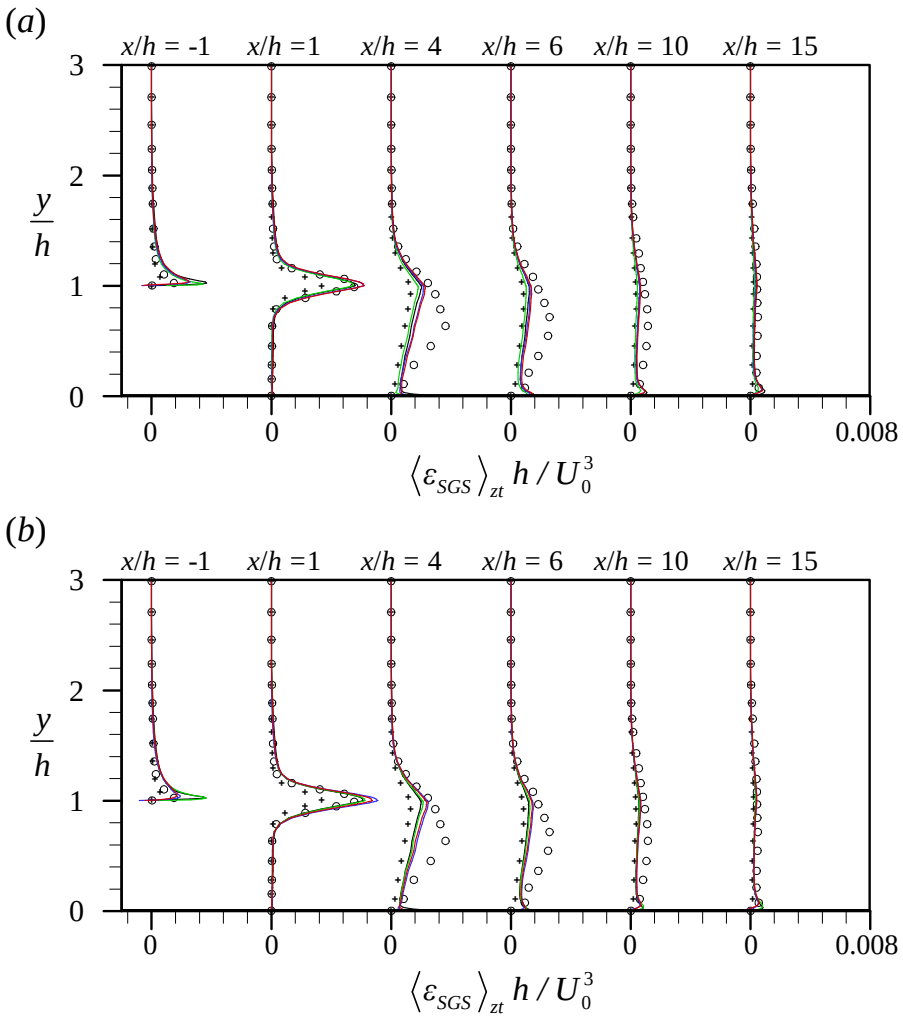

FIGURE 2.7. Mean SGS dissipation by different N_{hl} and N_{nr} (*a priori test*): (*a*) NN1; (*b*) NN2. ○, fDNS; +, DSM; —, CS1; —, CS2; —, CL; —, CR.

case	N_{hl}	N_{nr}	$\mathrm{N}_{\mathrm{data}}^{\mathrm{training}}$	$\mathrm{N}_{\mathrm{data}}^{\mathrm{test}}$
CR	2	32	2,560,000	256,000
CS1	1	128	2,560,000	256,000
CS2	2	16	2,560,000	256,000
CL	3	128	3,840,000	256,000

TABLE 2.2. Parametric-study cases for NN1 and NN2 to determine N_{hl} and N_{nr}. Here, CR is the reference case to be used in the LES of BFS flow. $\mathrm{N}_{\mathrm{data}}^{\mathrm{training}}$ and $\mathrm{N}_{\mathrm{data}}^{\mathrm{test}}$ are the numbers of training and test datasets, respectively, and those are used to obtain training error ϵ_τ for training and test datasets, respectively. The test dataset is collected from 4 instantaneous fDNS fields with the time interval of $5h/U_0$.

Chapter 3

LES of flow over a backward-facing step at $Re_h = 5100$

This chapter describes the results of *a posteriori* test (i.e., actual LES) with an NN-based SGS models. Two NN-based SGS models, NN1 and NN2, are tested, where $\bar{S}_{ij}$ and $\bar{\alpha}_{ij}$ at a grid point are the inputs of those models, respectively. We first test those NNs for the LES with the same grid resolution as that of trained data, and then test those NNs for the LES having coarser grid resolution than that of trained data. Computational details of the LES are given in §3.1, and the results of LES for two different grid resolutions are described in §3.2.

3.1. Computational details

Numerical methods for solving the filtered continuity and Navier-Stokes equations, eqs. (2.1) and (2.2), respectively, are the same as those for DNS. The computational domain sizes for LES in x, y and z directions are the same as those of DNS, and the computational time step is $\Delta t = 0.01h/U_0$ for the LES. Initial flow fields for $400h/U_0$ are discarded, and then the flow fields are averaged over $1200h/U_0$ to obtain the mean statistics. To provide realistic inlet turbulence, a

LES case	N_x, N_y, N_z	Δx^+_{min}	Δx^+_{max}	Δy^+_{min}	Δy^+_{max}	Δz^+
LES51GR	161, 57, 64	11.4	72.7	1.4	117.1	15.8
LES51GC	137, 41, 32	18.5	75.4	2.4	123.0	31.6

TABLE 3.1. Two LES cases having different grid resolutions (Re_h=5100). N_x, N_y and N_z are the numbers of grid points in streamwise, wall-normal and spanwise directions, respectively. Friction velocity u_τ at the inlet of the computational domain (DNS) is used ($u_\tau = 4.9619 \times 10^{-2} U_0$) for calculating grid spacing in wall units.

separate LES of TBL flow is conducted using DSM as the SGS model, and the other boundary conditions are the same as those used in DNS. The domain sizes for the LES of TBL and the recycling location are the same as those used in the DNS of TBL (see §2.2.2).

Table 3.1 shows two different grid resolutions for the LES of the backward-facing-step flow at $Re_h = 5100$. The grid resolution of LES51GR is the same as that of the fDNS used for training NN1 and NN2. On the other hand, the grid resolution of LES51GC is coarser than that of the trained data. For both LES51GR and LES51GC, we conduct four LESs with different SGS models: noSGS, DSM, NN1 and NN2, where the noSGS denotes the LES without SGS model. Unless otherwise mentioned, for the LES with NN1 and NN2, we do not use any special treatment such as the *ad hoc* clipping, wall damping or averaging over homogeneous directions.

3.2. Results and discussions

3.2.1. *LES51GR case*

Table 3.2 shows the reattachment lengths (X_r) from LES51GR, together with those from DNS, fDNS, and previous studies, where X_r in the present study is the distance from the step to the location of zero wall-shear stress. In the present study, X_r's from DNS and fDNS are $6.23h$ and $6.17h$, respectively, which are in good agreement with those from previous experiment (Jovic & Driver 1994) and DNS (Le *et al.* 1997). Here, the X_r of fDNS is obtained by filtering the mean velocity field from DNS, and it is smaller than that of DNS due to filtering in y direction near the wall. The X_r's from LES with NN1 and NN2 are well predicted, whereas the LES without SGS model overpredicts X_r.

Figure 3.1(a) shows the distribution of skin-friction coefficient along the wall from the LES, together with that of fDNS. All LES conducted provide similar minimum C_f (≈ -0.0035), which is lower than -0.0027 from fDNS, but is similar to -0.0034 from the experiment (Jovic & Driver 1994) (see figure 2.3). The discrepancy between LES and fDNS seems to be mainly due to the coarse grid resolution in LES together with the limitations of SGS models for the accurate predictions for C_f. On the other hand, the discrepancy may be also due to the difference in the inflow. In the present study, the recycling method of Lund *et al.* (1998) is used to generate inflow data for DNS and LES, respectively, but the inflow turbulence is not identical due to the difference in grid resolution. For example, the wall-normal and spanwise turbulence intensities of LES inflow are lower than those of DNS inflow (not shown here). Kang & Choi (2002) also pointed out that the difference in the inflow could contribute to the overprediction of minimum C_f. Figure 3.1(b) shows the distribution of pressure coefficient C_p at the wall. Both NN1 and NN2 show reasonable agreement with that fDNS,

and provide almost similar predictions to that of DSM. On the other hand, LES without the SGS model slightly underpredicts C_p at $x/h = 3 - 10$.

Figure 3.2 shows profiles of the mean streamwise velocity and rms streamwise velocity fluctuation at several x locations. For the mean streamwise velocity, a good agreement is found between fDNS and LESs with NN1 and NN2, whereas the LES without SGS model shows slightly different mean velocity near the wall at $x/h = 6$, expected by the large reattachment length. For the rms streamwise velocity, all LES conducted show similar predictions. On the other hand, for rms vertical and spanwise velocity fluctuations and the Reynolds shear stress, given in figure 3.3, the LES without SGS model overpredicts them near the step edge ($x/h = 1$), whereas LES with NN1, NN2 and DSM shows similar predictions for them. This overprediction for rms vertical velocity fluctuation near the step was also observed in the previous LES without SGS model (Akselvoll & Moin 1995). Figure 3.4 shows the one-dimensional energy spectra of the velocity fluctuations at three locations: $(x/h, y/h) = (1, 1.04), (4, 1.04)$ and $(6, 0.017)$. Overall agreements of the velocity spectra from NN1 and NN2 with those of fDNS are similar to those of DSM, whereas the noSGS overpredicts the spectra at high wavenumber indicating that dissipation is insufficient. Figure 3.5 shows the mean SGS dissipation $\langle \varepsilon_{SGS} \rangle_{zt}$ and the mean backscatter $\langle \varepsilon^{-}_{SGS} \rangle_{zt} = 0.5 \langle \varepsilon_{SGS} - |\varepsilon_{SGS}| \rangle_{zt}$. A reasonable agreement is found among the NN-based SGS models and fDNS for the SGS dissipation generated in the shear layer. For the backscatter, NN1 and NN2 provide non-negligible backscatter compared to that of fDNS. It has been pointed out that the non-negligible backscatter incurs the numerical instability in actual LES (Liu *et al.* 1994; Akhavan *et al.* 2000; Meneveau & Katz 2000; Anderson & Domaradzki 2012; Park & Choi 2021). For the filtered DNS of the turbulent channel flow at $Re_\tau \approx 180$, Park & Choi (2021) showed that the magnitude of the backscatter was compara-

ble to that of the mean SGS dissipation, but figure 3.5 indicates that, for the BFS flow at $Re_h = 5100$, the backscatter is approximately 10% of the mean SGS dissipation. Therefore, although NN1 and NN2 provide non-negligible backscatter, this does not incur the numerical instability in the LES of BFS flow. In this regard, the NN1 and NN2 have the advantages over the DSM that those NN models can predict backscatter in the LES, whereas the DSM does not provide it due to the averaging procedure for obtaining C_s. Note also that the LESs with NN1 and NN2 do not require special treatments such as the *ad hoc* clippings, wall damping, and averaging over homogeneous directions, which is another advantage over the DSM.

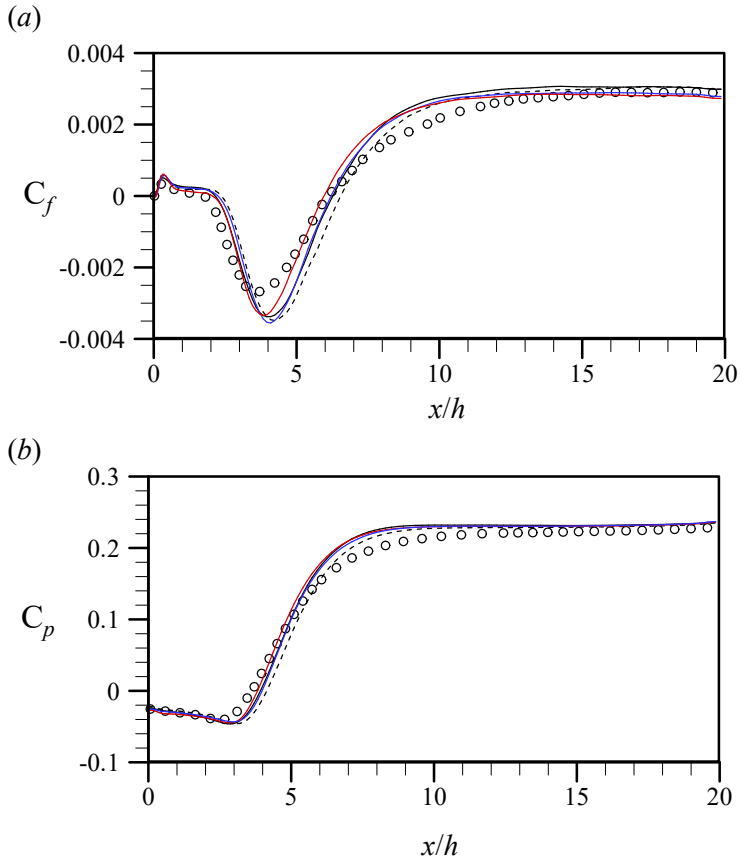

FIGURE 3.1. Coefficients of skin friction and wall pressure, C_f and C_p, respectively, from LES51GR: (*a*) skin-friction coefficient; (*b*) wall-pressure coefficient. ○, fDNS; - - -, noSGS; ——, DSM; ——, NN1; ——, NN2.

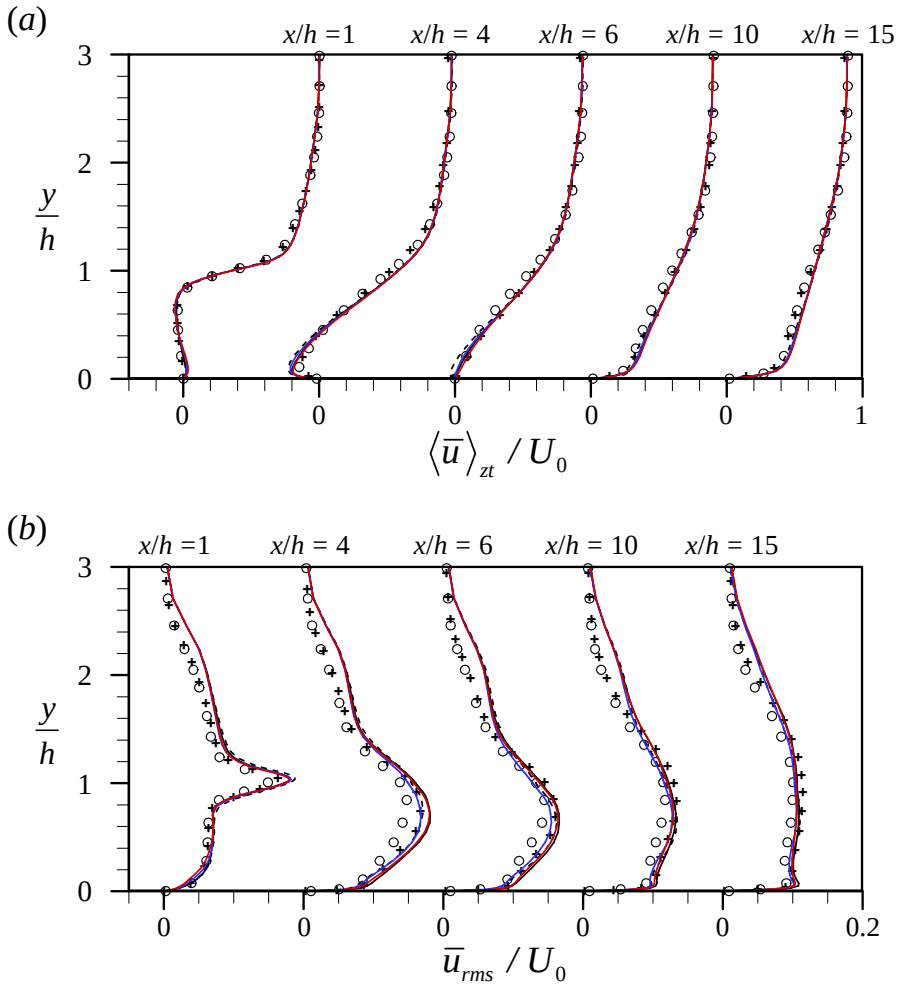

FIGURE 3.2. (*a*) Mean streamwise velocity and (*b*) rms streamwise velocity fluctuation from LES51GR. +, DNS; ○, fDNS; - - -, noSGS; ——, DSM; ——, NN1; ——, NN2.

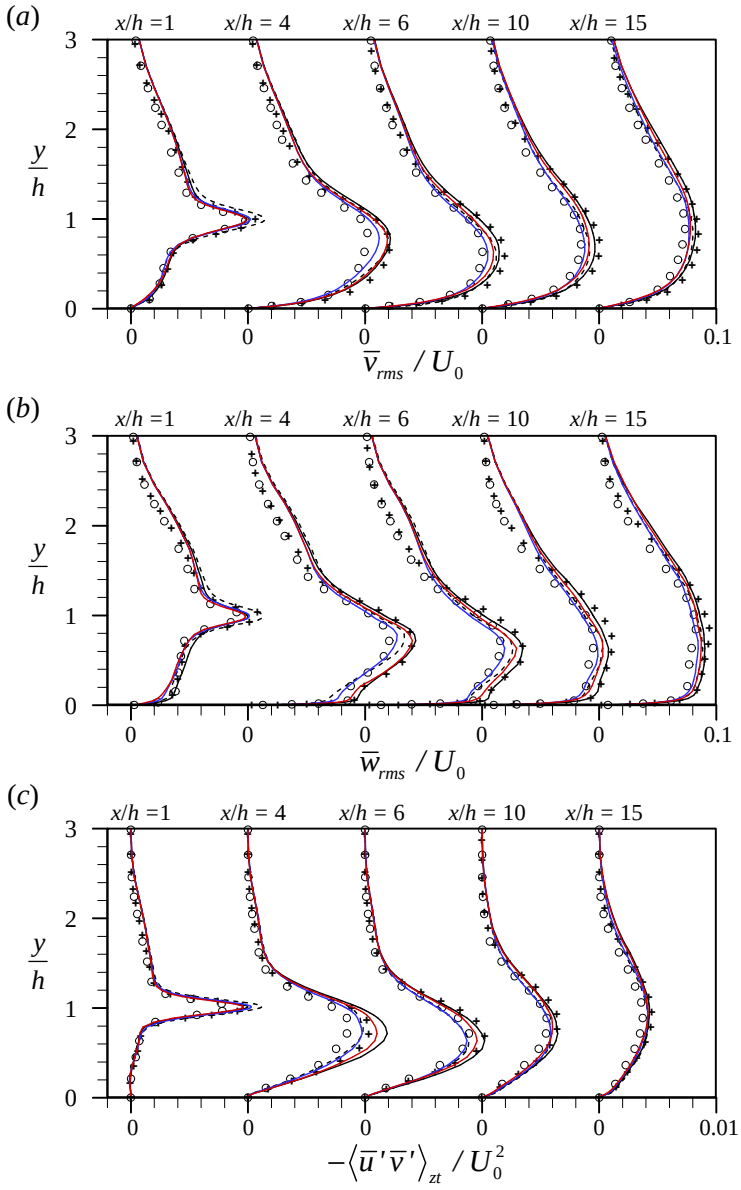

FIGURE 3.3. The rms wall-normal and spanwise velocity fluctuations and the Reynolds shear stress from LES51GR: (*a*) rms wall-normal velocity fluctuation; (*b*) rms spanwise velocity fluctuation; (*c*) the Reynolds shear stress. +, DNS; ○, fDNS; - - -, noSGS; ——, DSM; ——, NN1; ——, NN2.

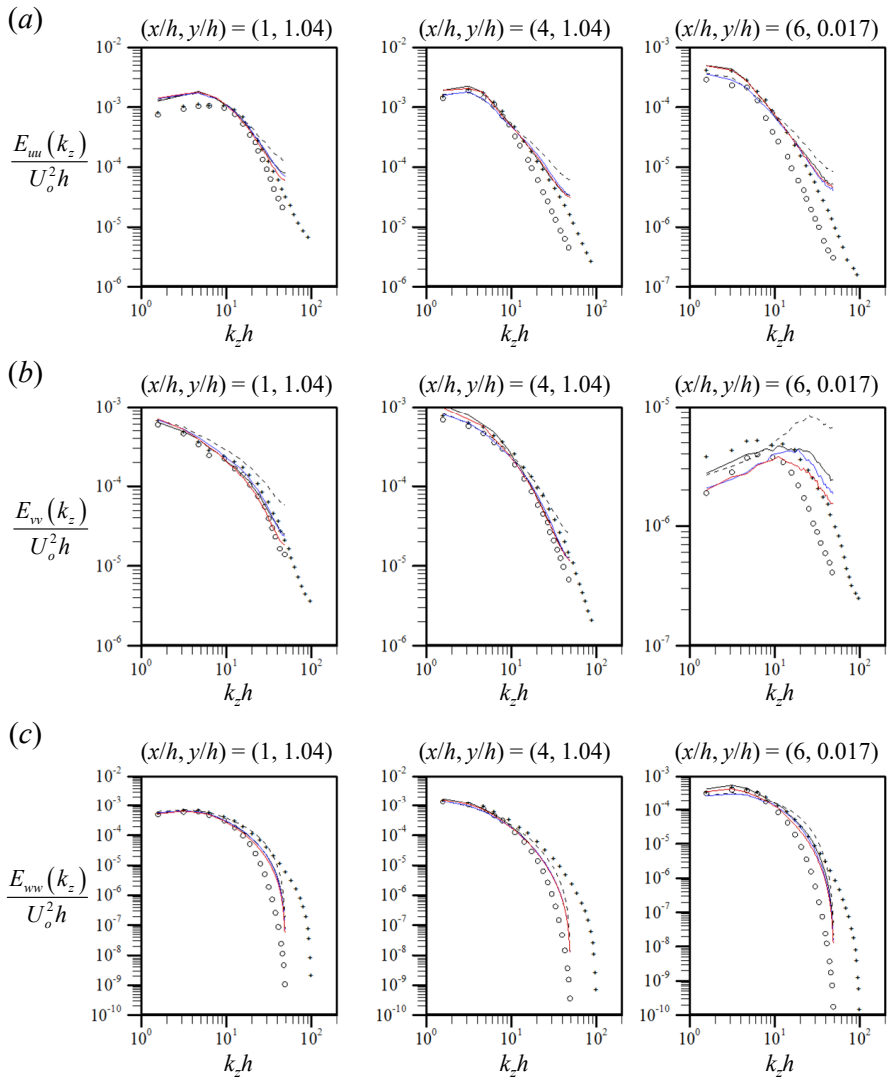

FIGURE 3.4. One-dimensional energy spectra of the velocity fluctuations from LES51GR: (*a*) streamwise (*b*) wall-normal; (*c*) spanwise. Here, the first, second and third columns are $(x/h, y/h) = (1, 1.04)$, $(4, 1.04)$ and $(6, 0.017)$, respectively. +, DNS; ○, fDNS; - - -, noSGS; ——, DSM; ——, NN1; ——, NN2.

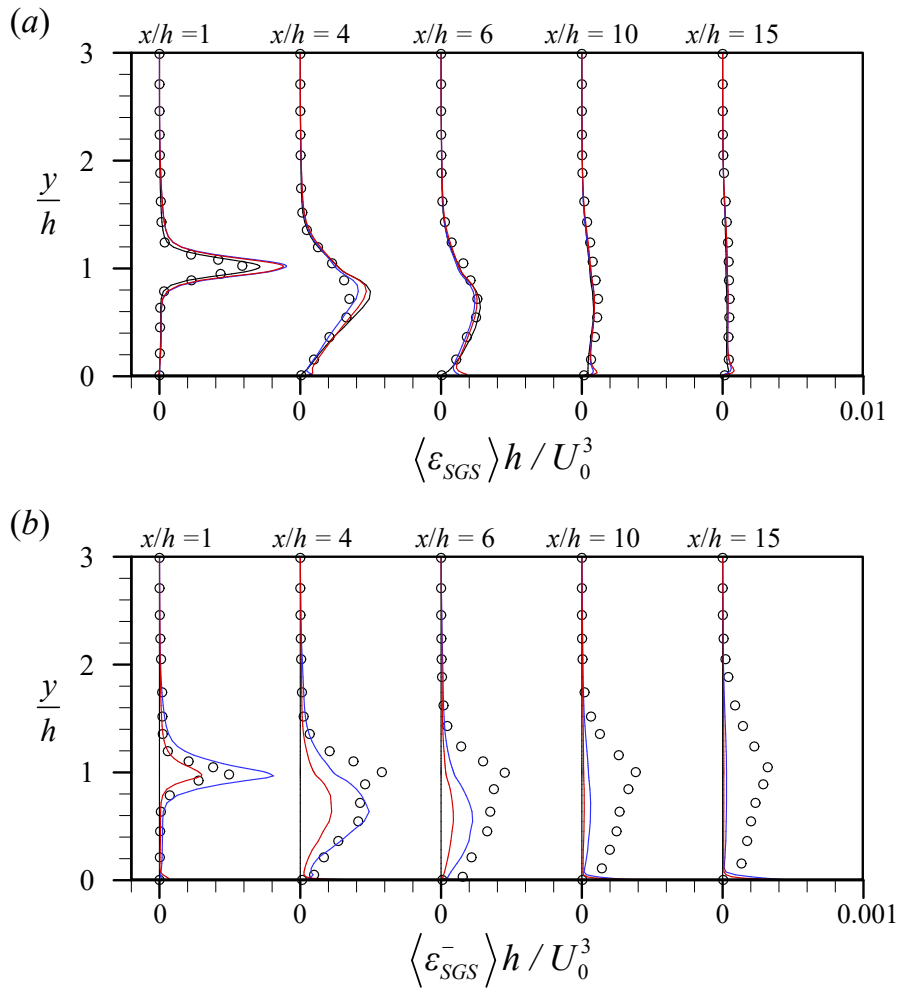

FIGURE 3.5. Mean SGS dissipation and backscatter from LES51GR: (*a*) mean SGS dissipation $\langle \varepsilon_{SGS} \rangle_{zt}$; (*b*) mean backscatter $\langle \varepsilon^{-}_{SGS} \rangle_{zt}$. ○, fDNS; - - -, noSGS; ——, DSM; ——, NN1; ——, NN2.

Data from	method	SGS model	X_r/h
present study	DNS	-	6.23
present study	fDNS	-	6.17
present study	LES	noSGS	6.54
present study	LES	DSM	6.27
present study	LES	NN1	5.96
present study	LES	NN2	6.21
Jovic & Driver (1994)	Experiment	-	6 ± 0.15
Le *et al.* (1997)	DNS	-	6.28
Akselvoll & Moin (1995)	LES	DSM	6.36
Kang & Choi (2002)	LES	DSM	6.20
Simons *et al.* (2002)	LES	SM	6.6
Aider *et al.* (2007)	LES	SFM	5.29 -5.80
Panjwani *et al.* (2009)	LES	DSM, SFM	7.2 - 7.4
Yang *et al.* (2020)	LES	DSM	6.64

TABLE 3.2. Reattachment length (X_r) of BFS flow at $Re_h = 5100$ and $ER = 1.2$. Here, LES of the present study is the LES51GR case. For the SGS model, SM is the Smagorinsky model with constant model coefficient, SFM is the structure function model. Note that a large scatter in X_r's from previous LES studies is due to the combination of different computational setups such as numerical schemes, inflow boundary condition, grid resolutions, and the SGS model.

3.2.2. *LES51GC case*

Figure 3.6 shows the coefficients of skin-friction and wall pressure from the LES51GC, together with those from DNS and fDNS. Here, fDNS is the filtered DNS with the same grid resolution as that of LES51GC. Both NN1 and NN2 show better predictions for C_f and C_p than noSGS and DSM, especially in the regions of $x/h < 3$ and near the reattachment location. The reattachment lengths from fDNS, NN1 and NN2 are $X_r = 6.12h, 6.18h$ and $5.97h$, respectively, whereas reattachment lengths are $5.68h$ and $6.82h$ from noSGS and DSM, respectively. The X_r's from NN1 and NN2 are quite well predicted, even though those models are trained by using fDNS data whose grid sizes are different from that of LES51GC. On the other hand, the LES without SGS model significantly underpredicts X_r. The prediction for X_r with DSM is also poor, and this may be attributed to the limitation of the eddy-viscosity model in the LES with coarse grid resolution, where Jiménez & Moser (2000) indicated that the grid resolution should be high enough for most of the SGS stresses to be carried by the resolved scales in application of the eddy-viscosity model.

Figure 3.7 shows the mean streamwise velocity and the Reynolds shear stress, and figure 3.8 shows the rms velocity fluctuations. For the mean streamwise velocity, a good agreement is found between fDNS and LESs with NN1 and NN2, whereas the DSM shows negative velocity at $x/h = 6$, expected by its large reattachment length. For prediction of the Reynolds shear stress and rms streamwise velocity fluctuation, the difference between SGS models are small. For the rms vertical and spanwise velocity fluctuations, the LES without SGS model significantly overpredicts those statistics near the step edge ($x/h = 1$) and in the recirculation regions ($x/h = 4$), whereas LESs with NN1 and NN2 overpredict them compared to those of fDNS. The DSM shows good agreement of those statistics with those of fDNS, but this may not much meaningful since the DSM does

not predict well the mean streamwise velocity near the reattachment location. To improve the performance of NN models, we have trained another NNs using two different fDNS datasets together whose grid sizes are bigger and smaller than the grid size of LES51GC, as suggested by Park & Choi (2021), where they showed significant improvement on the performance an NN for the LES having different grid resolution from that of trained data. Figure 3.9 shows the rms vertical and spanwise velocity fluctuations, with this new NN. Here, only NN1 is shown for clarity. The predictions of this new NN1 (NN1n) are slightly better than that of the previous NN1 (NN1o) for those statistics, but the difference in predictions is not significant. Note that Park & Choi (2021) applied the spectral-cutoff filter in the streamwise and spanwise directions with only one filter size for making one fDNS dataset in the turbulent channel flow, where the filter sizes are uniform in those directions, respectively. On the other hand, for the BFS flow in the present study, the box filter is applied in all x, y and z directions, where the filter sizes are different by location. Therefore, various filter sizes are already used for making one fDNS dataset, and this may be a reason for quite good performance of the NN1o for the LES having different grid resolution from that of trained data.

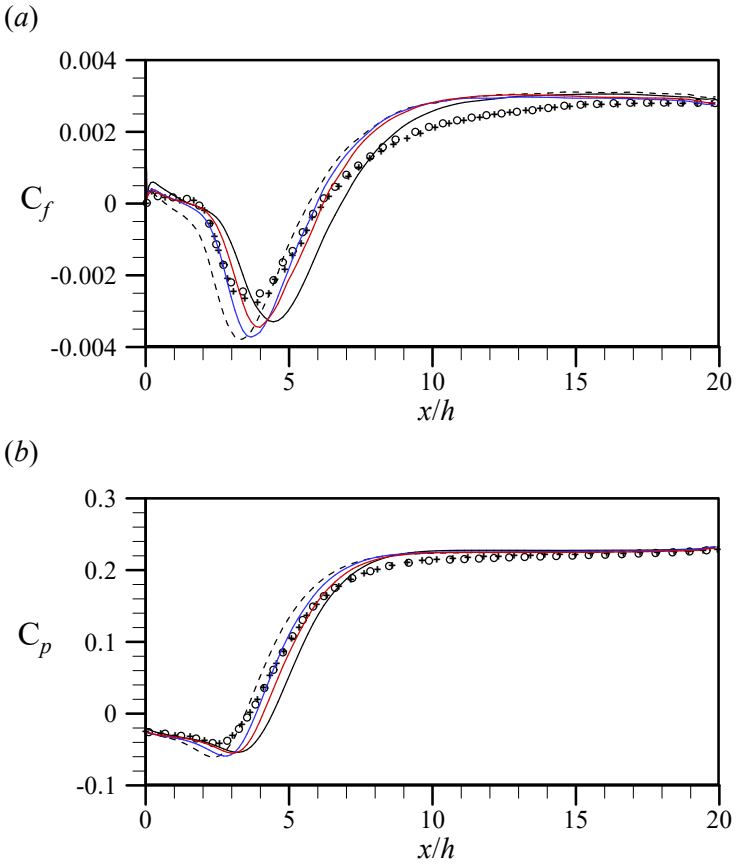

FIGURE 3.6. Coefficients of skin friction and wall pressure, C_f and C_p, respectively, from LES51GC: (*a*) skin-friction coefficient; (*b*) wall-pressure coefficient. +, DNS; ○, fDNS; - - -, noSGS; ——, DSM; ——, NN1; ——, NN2.

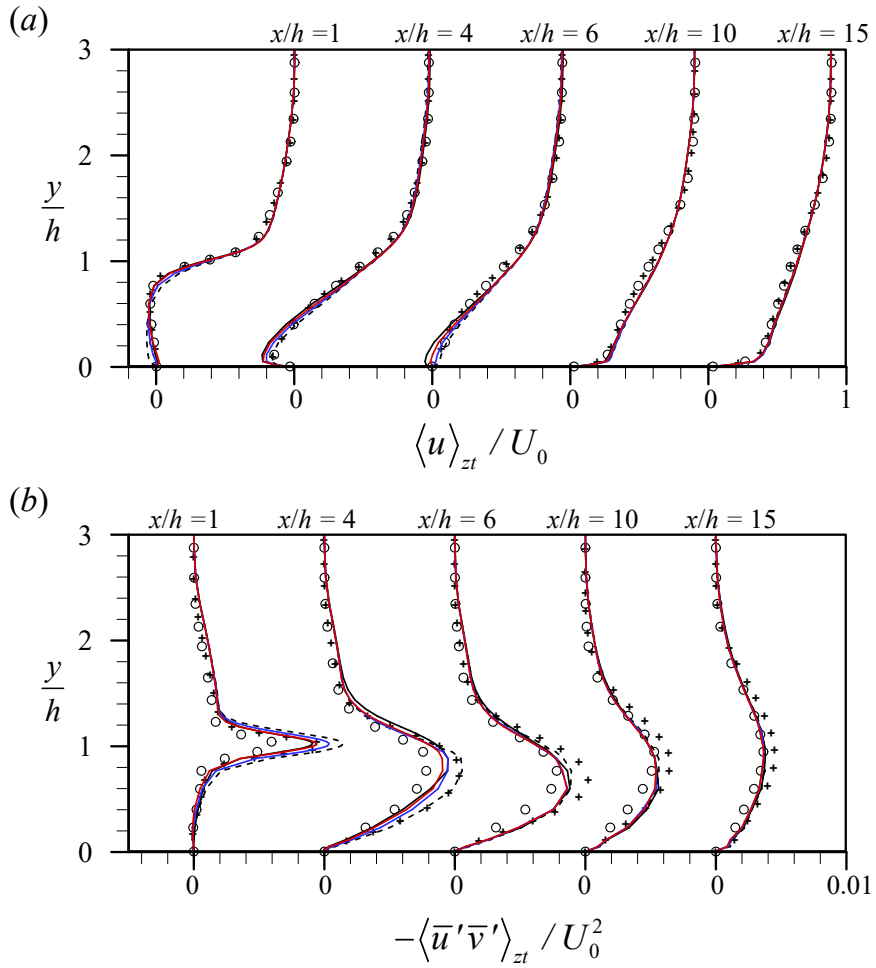

FIGURE 3.7. (*a*) Mean streamwise velocity and (*b*) the Reynolds shear stress from LES51GC. +, DNS; ○, fDNS; - - -, noSGS; ——, DSM; ——, NN1; ——, NN2.

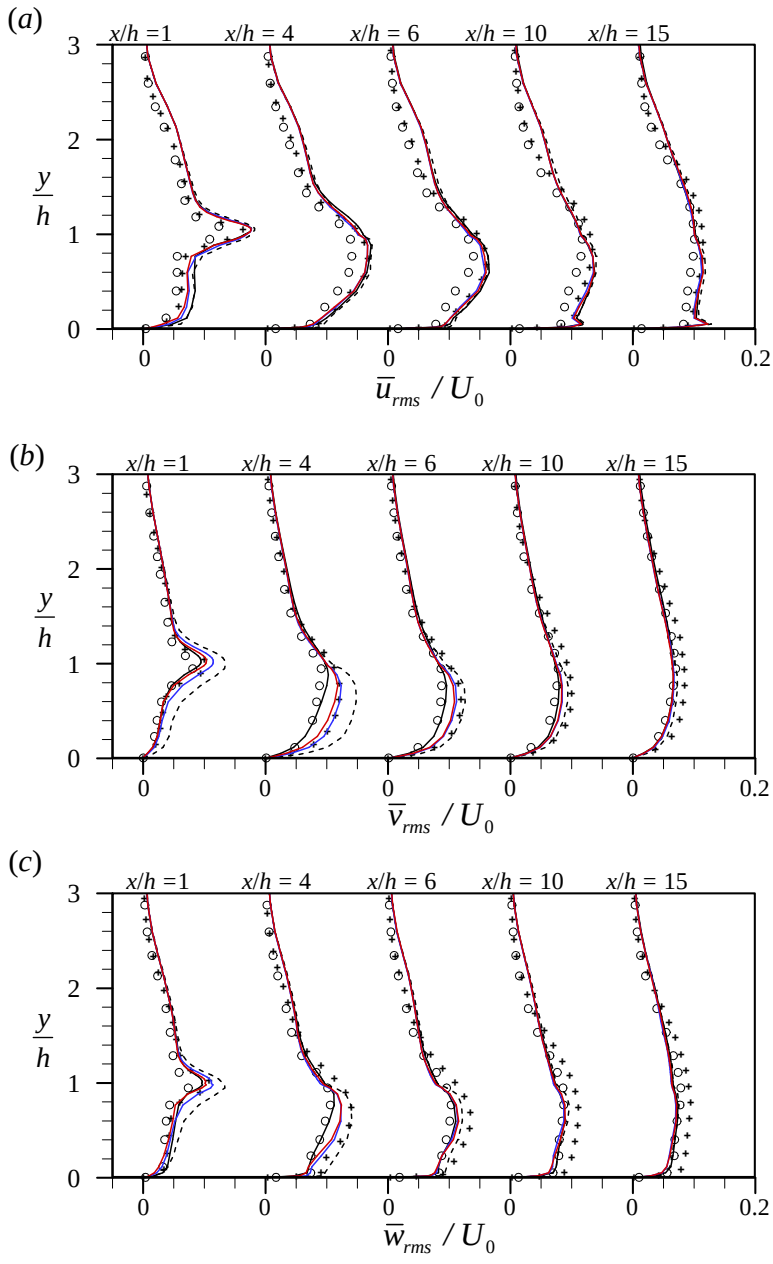

FIGURE 3.8. The rms velocity fluctuations from LES51GC: (*a*) streamwise; (*b*) wall normal; (*c*) spanwise. +, DNS; ○, fDNS; - - -, noSGS; ——, DSM; ——, NN1; ——, NN2.

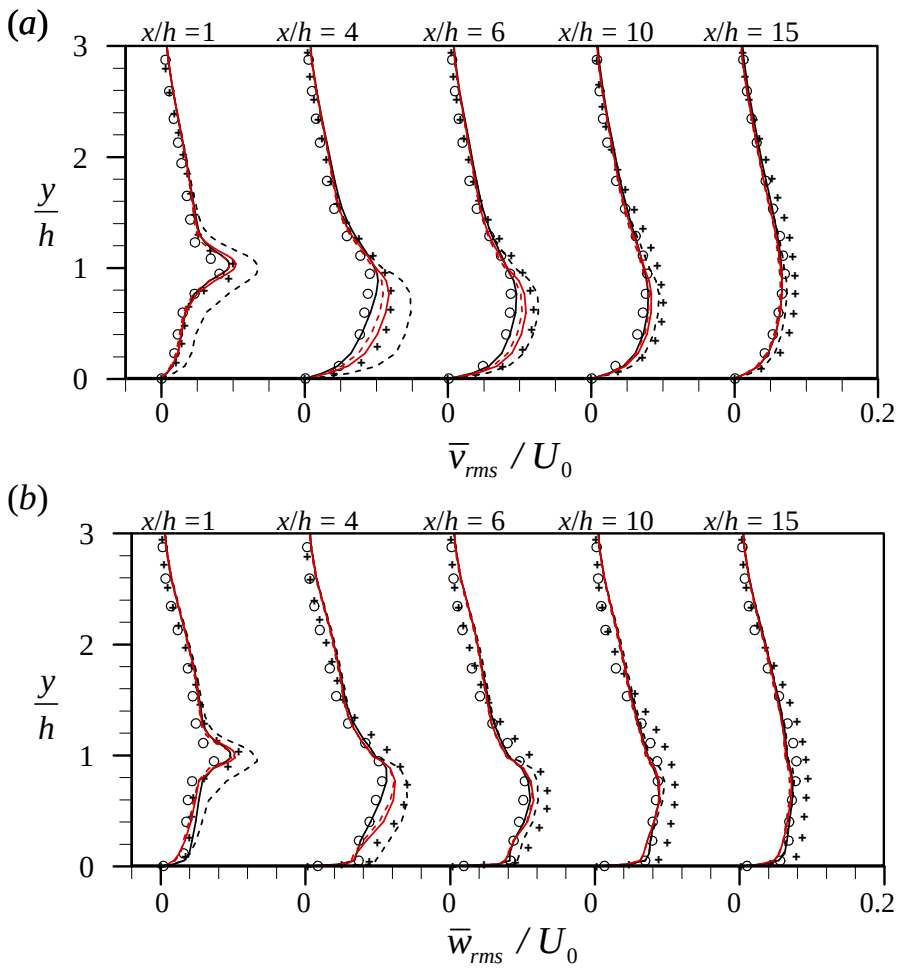

FIGURE 3.9. The rms wall-normal and spanwise velocity fluctuations from LES51GC: (*a*) wall-normal; (*b*) spanwise. +, DNS; ○, fDNS; - - -, noSGS; ——, DSM; ——, NN1o; - - -, NN1n. The numbers of grid points of fDNS for training NN1o are $161(x) \times 57(y) \times 64(z)$, whereas the numbers of two different fDNS for training NN1n are $145(x) \times 45(y) \times 48(z)$ and $129(x) \times 37(y) \times 24(z)$, respectively. The numbers of grid points used in LES51GC are $137(x) \times 41(y) \times 32(z)$.

Chapter 4

LES of controlled backward-facing-step flow by multiple taps

One of the essential issues in research of turbulent flow over a backward-facing step is the flow-separation control to increase mixing (or to enhance the heat and mass transfer) behind the step, where the reduction of the reattachment length has been an indirect measure of the mixing increase. Many control devices have been investigated to enhance the mixing in an active or passive manner. For the active control, the blowing/suction is imposed at the step edge, for example, with a specific blowing/suction frequency (Bhattacharjee *et al.* 1986; Roos & Kegelman 1986; Hasan & Khan 1992; Chun & Sung 1996) or by the feedback control theory (Kang & Choi 2002; Neumann & Wengle 2003; Gautier & Aider 2013). Those active control methods, however, are difficult to install and require additional energy input, so in terms of practical use, a passive control device may be preferable to those active ones (Park *et al.* 2007). Various passive control devices have been suggested so far; for example, segmented step face (Gai & Sharma 1984), upstream cavity or rod (Isomoto & Honami 1989), surface rib or groove (Selby *et al.* 1990; Kim & Chung 1995), upstream fence (Neumann & Wengle

2003) and fence at the step edge (Park *et al.* 2007). Park *et al.* (2007) indicated that the three-dimensional disturbance on the flow separation has been more efficient for the mixing enhancement than the two-dimensional one, and one of the most successful devices for the three-dimensional disturbance is the small taps (Zaman *et al.* 1994; Foss & Zaman 1999; Park *et al.* 2006, 2007). Meanwhile, Park *et al.* (2007) conducted experimental study for the BFS Flow with single tap or multiple taps at $Re_h = 24000$ and $ER = 1.12$, and showed that multiple taps were more effective on the mixing increase than the single tap. They showed that the multiple taps could reduce the reattachment length by 51% from that of the uncontrolled flow, where vertical height and spanwise width of the tap were $l_y = 0.3h$ and $l_z = 0.3h$, respectively, and the spanwise spacing between two adjacent taps was $\lambda = 2.33h$ (see figure 4.1*a* for the schematic of the taps).

Having confirmed the successful application of an NN-based SGS model for the BFS flow at $Re_h = 5100$, the performance of NN-based SGS model is assessed for the LES of BFS flow having multiple taps, where the flow and tap parameters are similar to those used in the experiment by Park *et al.* (2007). Here, we only assess the performance of the NN1, because NN1 performs better than NN2 in turbulent channel flow (part I), even though the difference between the two models in the LES of BFS flow at $Re_h = 5100$ is not significant. The NN1 is trained using the filtered DNS at $Re_h = 5100$, as described in §2. The numerical methods for solving the filtered Navier-Stokes equations are the same as those used in §3, and other computational details are given in §4.1, followed by the LES results in §4.2.

4.1. Computational details

The schematic of the computational domain is the same as figure 2.1, and the size of the computational domain is $-2.5 \leq x/h \leq 20$, $0 \leq y/h \leq 9.33$

and, $0 \leq z/h \leq 4.67$. The step-height Reynolds number and the expansion ratio are $Re_h = 24000$ and $ER = 1.12$, respectively, which are same as those of the experiment (Park *et al.* 2007). We consider three configurations of the backward-facing step: 1) without tap (uncontrolled), 2) with taps having $\lambda = 4.67h$, and 3) with taps having $\lambda = 2.335h$. The taps are applied at the step edge, as shown in figure 4.1, where the vertical height and the spanwise width of the tap are $l_y = 0.3h$ and $l_z = 0.3h$, respectively. The streamwise thickness of the tap is set to be $l_x = 0.05h$, to adequately describe the tap by the immersed boundary method. This l_x is greater than that used in the experiment ($l_x = 0.03h$ in Park *et al.* 2007), but this difference in l_x's may not much affect the flow disturbance generated by the tap, since the l_y and l_z are still much larger than l_x. The numbers of grid points used are $241 \times 129 \times 128$ in the streamwise, wall-normal and spanwise directions, respectively. For the grid resolution, we refer to the grid resolution used in the previous LES for the high-Reynolds BFS flow (Akselvoll & Moin 1995). The grid spacings normalized by h and in wall units, respectively, are given in table 4.1, together with those of training data for the NN1 and with those of previous LES by Akselvoll & Moin (1995). The numbers of grid points located inside a tab are $3 \times 33 \times 9$ in the streamwise, vertical and spanwise directions, respectively. The computational time step is $\Delta t = 0.003h/U_0$. Initial flow fields for $210h/U_0$ are discarded, and then the flow fields are averaged over $1500h/U_0$ to obtain the mean statistics. The LESs for each BFS configuration are conducted with noSGS, DSM and NN1, and for the NN1, the backscatter is forced to be zero by eq. (3.1) in part I to ensure the stable LES for this high-Reynolds number BFS flow. For the DSM, we keep using the averaging in z direction for obtaining the model coefficient in the LES of BFS flow with taps, even though it is no longer homogeneous in the z direction with the taps. This is based on the previous observation (Park *et al.* 2006) that

the LES result was not sensitive to the detailed averaging procedure. They also indicated that this insensitivity may be attributed to the self-adjusting mechanism of dynamic model described in Park *et al.* (2005).

In the experiment (Park *et al.* 2007), inflow was the full-developed turbulent boundary layer, where $\delta/h = 0.6$ and $Re_\theta = 1230$ at $0.5h$ upstream of the step edge. To provide realistic turbulence at the domain inlet for the LES of BFS flow, a separate LES of TBL flow is conducted using DSM, where Re_θ at the inlet of this simulation is $Re_\theta = 1000$. The domain size is $0 \leq x/h \leq 12$, $0 \leq y/h \leq 8.33$ and , $0 \leq z/h \leq 2.335$ and the numbers of grid points are $192 \times 81 \times 64$ in streamwise, wall-normal and spanwise directions, respectively. Since the inlet is located at $2.5h$ upstream of the step edge in the LES of BFS flow, the TBL flow fields at $2h$ upstream of the location having $Re_\theta = 1230$ are stored. Note also that the spanwise domain size of this TBL simulation is half of that used in the LES of BFS flow, so the flow fields are combined in the spanwise direction based on the periodic boundary condition. The resulting boundary layer thickness and Re_θ of the inflow are $\delta/h = 0.5$ and $Re_\theta = 1140$, respectively. Figure 4.2 shows the mean velocity and the turbulence intensities from the LES of TBL flow, together with DNS data (Schlatter & Örlü 2010). The LES result show reasonable agreement with that of DNS data for the mean velocity. For the turbulence intensities and the Reynolds stress, the LES results show reasonable predictions, as the over- and under predictions for the streamwise and the cross flow components, respectively, are commonly observed in the LES of wall-bounded flows with a coarse grid resolution (Bae *et al.* 2018).

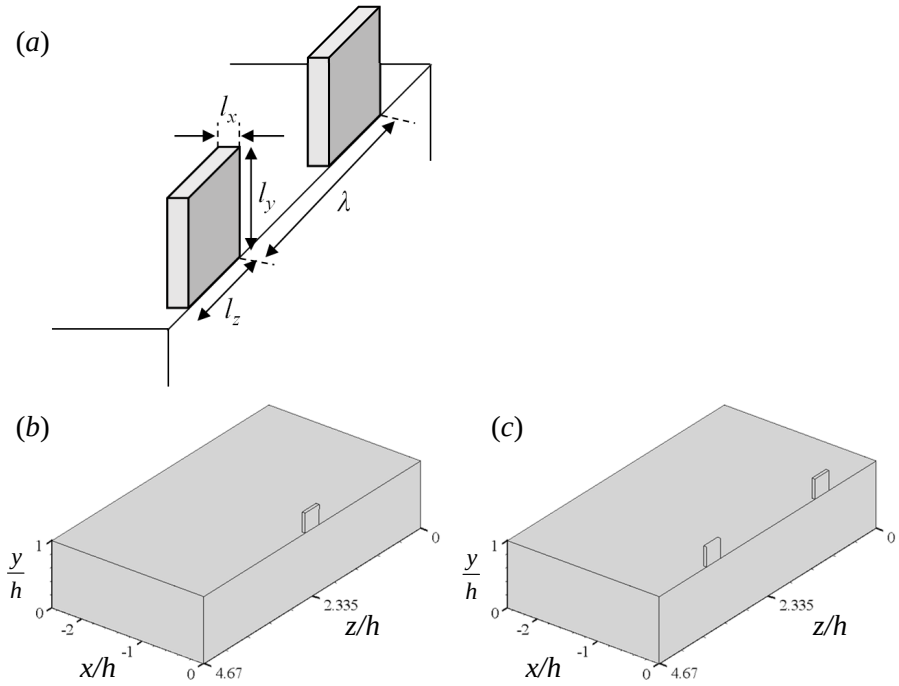

FIGURE 4.1. Tap configurations: (*a*) parameters of multiple taps; (*b*) taps on BFS with $\lambda = 4.67h$; (*c*) taps on BFS with $\lambda = 2.335h$. In (*b*), the location of the tap center is $z = 2.335h$, and in (*c*), the locations of the tap centers are $z = 1.1675h$ and $3.5025h$, respectively.

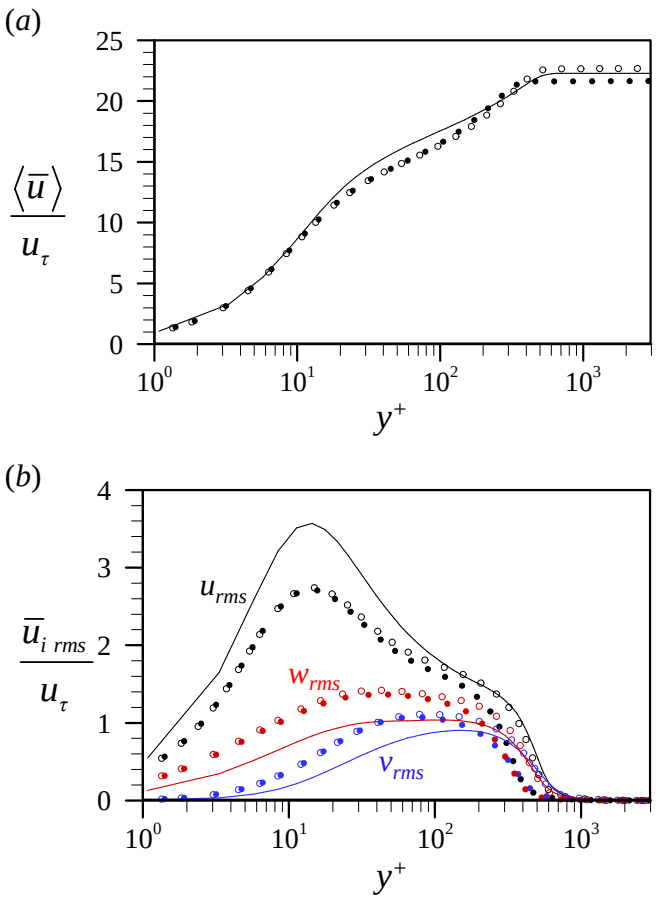

FIGURE 4.2. Inflow statistics from LES of TBL flow: (*a*) mean velocity; (*b*) rms velocity fluctuations. The Re_θ of the inflow is 1140. In (*a*, *b*), the solid line denotes the present LES, whereas the closed and open circles denote the previous DNS results by Schlatter & Örlü (2010) at $Re_\theta = 1000$ and $Re_\theta = 1410$, respectively. In (*b*), black, blue and red colors denote the rms velocity fluctuations in streamwise, wall-normal and spanwise directions, respectively.

Case	$L_x/h, L_{xi}/h, L_y/h, L_z/h$	N_x, N_y, N_z	$\Delta x_{\min}/h$, $\Delta y_{\min}/h$, $\Delta z/h$	$\Delta x^+_{\min}$, $\Delta y^+_{\min}$, Δz^+
LES24000	22.5, 2.5, 9.33, 4.67	241, 129, 128	0.015, 0.0020, 0.0365	16.2, 2.2, 39.3
LESAM	30, 10, 5, 3	244, 96, 96	0.015, 0.0016, 0.0313	16.6, 1.8, 34.6
training data	22.5, 2.5, 6, 4	161, 57, 65	0.045, 0.0055, 0.0625	11.4, 1.4, 15.8

TABLE 4.1. Domain sizes and grid resolutions of the present LES at $Re = 24000$ (LES24000 case), together with those used in the LES at $Re_h = 28000$ (Akselvoll & Moin 1995) (LESAM case), and those of training data for the NN1. Here, the training data is the fDNS of the BFS flow at $Re_h = 5100$, described in §2.2.3. The friction velocity u_τ for obtaining the grid spacing in wall units are $0.04492U_0$ and $0.04962U_0$ for LES24000 and training data, respectively, which are u_τ's from the inflow data. For the LESAM, $u_\tau = 0.03952U_0$ is used, which is the friction velocity at $x = -3.8h$ from the experiment by Vogel & Eaton (1985) at $Re_h = 28000$.

4.2. Results

In the experiment (Park *et al.* 2007), the reattachment length of the uncontrolled flow (i.e., without taps) was $X_r = 5.8h \pm 0.25h$, and the NN1 well predicts the reattachment length showing $X_r = 6.02h$. The DSM and noSGS provide the reattachment lengths of $X_r = 6.45h$ and $X_r = 6.66h$, respectively, which are larger than those of the experiment and NN1. Figure 4.3 shows the profiles of mean streamwise velocity and rms streamwise velocity fluctuation for the uncontrolled flow, together with those from the experiment. For both statistics, the difference between DSM and NN1 is not significant, but the DSM shows the backflow at $x = 6h$, as expected by the overpredicted X_r. On the other hand, the noSGS severely overpredicts the rms streamwise velocity fluctuation albeit showing similar performance for the mean velocity to that of the DSM. The LES results for the uncontrolled flow indicate that the NN1 provides fairly good predictions for a higher Reynolds number, even though the training is performed at a lower Reynolds number of $Re_h = 5100$. This may indicate that the relation between the SGS stress and strain rate which are non-dimensionalized by h and U_0 is not much varied by the Reynolds number in the BFS flow (especially near the flow separation and shear layer). Meanwhile, the grid spacings for the LES at $Re_h = 24000$ also differ from those of the training data. In §3.2.2, the NN1 for LES51GC has shown fairly good predictions for the reattachment length and the turbulence statistics, even though the grid resolution of the LES51GC is coarser than that of the training data. For the LES at $Re_h = 24000$, the grid spacings in wall units are similar to those of the LES51GC (see tables 3.1 and 4.1), and this could also be one of the reasons that the NN1 works well in the LES of a higher Reynolds number.

Figures 4.4 and 4.5 show the profiles of mean streamwise velocity and rms streamwise velocity fluctuation for the controlled flow with $\lambda = 2.335h$, at the

tap center ($z^* = 0$) and at the middle of two adjacent tabs ($z^* = 0.5$), respectively, where $z^* = |z - z_c|/\lambda$ and z_c is the location of tap center. For those statistics, the predictions of noSGS are significantly different from those of DSM and NN1, clearly indicating that the contribution of the SGS model is of great importance in the LES of the controlled flow. On the other hand, the NN1 shows almost similar predictions to those of DSM for those statistics, even though a slight difference in the predictions is observed for u_{rms} at $z^* = 0.5$. Figure 4.6 shows the variation of the wall-pressure coefficient C_p along the spanwise direction at several streamwise locations. Here, the results of noSGS are not shown for clarity. In the cases of NN1 and DSM, the reference pressures are obtained so that the C_p's of NN1 and DSM at $(x/h, z/h) = (1, 4.67)$ are the same as those of the experiment. Both NN1 and DSM show qualitatively good predictions for the spanwise variation of the C_p, where the C_p is relatively low at the tap-center z locations for both controlled cases.

Figure 4.7 shows the variations of X_r in the spanwise direction for controlled flows, together with those from the experiment. The NN1 shows the best prediction performance for the spanwise variation of X_r among considered SGS models. For example, the NN1 could capture the local minimum of X_r for the case of $\lambda = 4.67h$ albeit the z location for this minimum is different from that of the experiment. For the controlled flow with $\lambda = 4.67h$, the spanwise-averaged reattachment lengths, $\bar{X}_r$'s, are $5.70h, 5.18h$ and $4.77h$ from noSGS, DSM and NN1, respectively. Since the experiment did not present $\bar{X}_r$ for $\lambda = 4.67h$, we have numerically integrated the X_r along the spanwise direction, and this $\bar{X}_r$ is 3.90. The $\bar{X}_r$'s for the case of $\lambda = 2.335h$ are $4.75h, 4.60h$ and $3.78h$ from noSGS, DSM and NN1, respectively, where $\bar{X}_r = 2.84h$ from the experiment. The $\bar{X}_r$'s from the NN1 are closer to the experimental results than those from the noSGS and DSM, but the $\bar{X}_r$'s have a large deviation from those of the ex-

periment. This deviation is greater for $\lambda = 2.335h$ than for $\lambda = 4.67h$, and this may be originated from insufficient spanwise domain size, where we use a much smaller domain size ($L_z = 4.67h$) than that of the experiment ($L_z = 14h$) for the BFS with multiple taps. Although the periodic boundary condition is used to describe the periodicity over the taps, an artificial effect on the controlled flow may have increased as the number of taps increases, resulting in the different prediction for the spanwise variation of X_r to that of the experiment. Besides the spanwise domain size, the grid resolutions near the tap may also be insufficient to accurately resolve flow there, as the grid resolutions are the same as those of the uncontrolled flow. Nevertheless, the present LES with NN1 could capture the qualitative behaviors of the controlled flows, and this LES result would be enough to estimate the performance of NN1 for the LES of the controlled flows. Therefore, we have not further attempted to accurately reproduce the experimental data, and we investigate the performance of NN1 for other flow statistics by comparing it with that of the DSM.

Figure 4.8 shows the Reynolds shear stress from the LES with NN1 and DSM for three BFS configurations. This quantity is calculated to check the similarity between NN1 and DSM, as there is no available experimental data. At $z^* = 0$, NN1 and DSM provide nearly identical results, whereas non-negligible differences are observed at $z^* = 0.5$ where the X_r is smaller than that at $z^* = 0$. For both cases of controlled flow, the DSM provides a larger Reynolds shear stress at $z^* = 0.5$ (especially at $x/h = 2$ and 4) than that of the NN1, and this may result in a larger X_r from DSM than that from the NN1. Figures 4.9 and 4.10 show the mean SGS shear stress and SGS dissipation, respectively, from the LES with NN1 and DSM. Both SGS models yield the highest SGS shear stress and SGS dissipation near the separation point. For the SGS shear stress, significant differences are observed between NN1 and DSM, where DSM produces much

smaller stress than that of the NN1. Although the magnitude of SGS stress is much smaller than that of the Reynolds stress, the contribution of the SGS model in BFS flow is of great importance, considering the poor performance of noSGS (as shown in figures 4.3-4.5). Therefore, the different performances of NN1 and DSM for the LES of controlled flow shall be based on the different predictions for the SGS stress. For the SGS dissipation, the NN1 and DSM have similar predictions at $z^* = 0$, but non-negligible differences are observed at $z^* = 0.5$. For example, the peak value from NN1 at $x/h = 0.05$ for the controlled flow with $\lambda = 2.335h$ are 70% of that from the DSM, but the NN1 produces bigger SGS dissipation than that of the DSM further downstream locations. Figure 4.11 shows the ratio of the SGS dissipation to molecular dissipation, where the molecular dissipation is defined as $\epsilon_M = 2\nu\bar{S}_{ij}\bar{S}_{ij}$, as also used by Akselvoll & Moin (1995) in the LES of BFS flow at $Re_h = 28000$. The ratios from the NN1 and DSM show significantly different behavior for all streamwise locations, clearly indicating that the NN1 has a different prediction performance from that of the DSM. It is also noticeable that the kinks near $y = h$ are observed for NN1, which are also observed in the LES with the Smagorinksy model in the previous LES by Akselvoll & Moin (1995). They pointed out that these kinks were originated from the small grid sizes in the wall-normal direction, which is directly used for calculating the eddy viscosity, as $\nu_t = (C_s\Delta)^2|\bar{S}|$, resulting in very sensitive changes in this ratio. Although the grid size in wall-normal direction is not the input variable of the NN1, the relation between SGS stress and the grid size seems to be implicitly included in the NN1, resulting in those kinks as the Smagorinsky model. On the other hand, Akselvoll & Moin (1995) showed that the DSM does not have these kinks, because the $(C_s\Delta)^2|\bar{S}|$ is obtained by the dynamic procedure which uses the ratio of test- to grid-filter sizes, not the grid-filter size itself.

Figure 4.12 shows the instantaneous vortical structures identified by the iso-surfaces of $\lambda_2 = -10U_0^2/h^2$ (Jeong & Hussain 1995) from LESs with noSGS, DSM and NN1. More vortical structures are observed from the noSGS due to insufficient dissipation, as the LES without SGS model has only the molecular dissipation. On the other hand, the instantaneous flow fields from LESs with DSM and NN1 show similar vortical structures to each other, because the magnitudes of the SGS dissipation from DSM and NN1 are similar to each other albeit having different predictions for the SGS dissipation in detail.

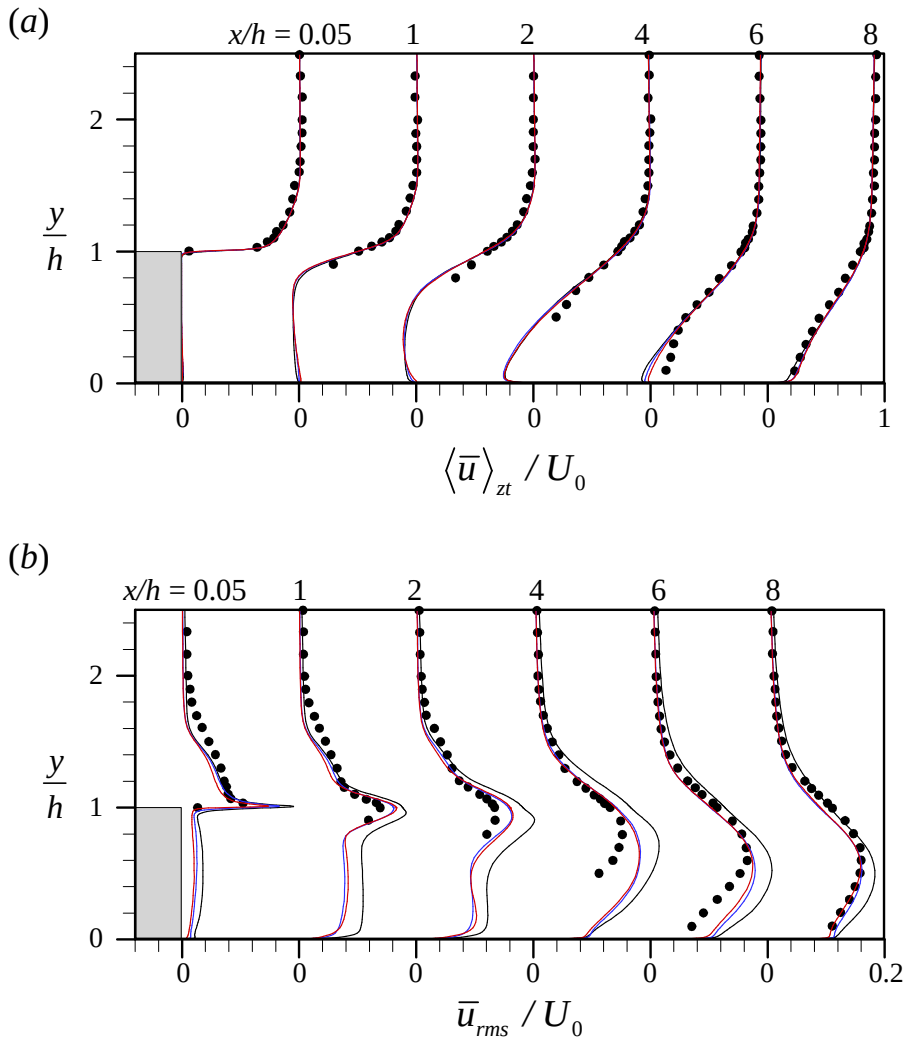

FIGURE 4.3. LES results for the uncontrolled flow at $Re_h = 24000$: (*a*) mean streamwise velocity; (*b*) rms streamwise velocity fluctuation. ●, experiment (Park *et al.* 2007); —, noSGS; —, DSM; —, NN1.

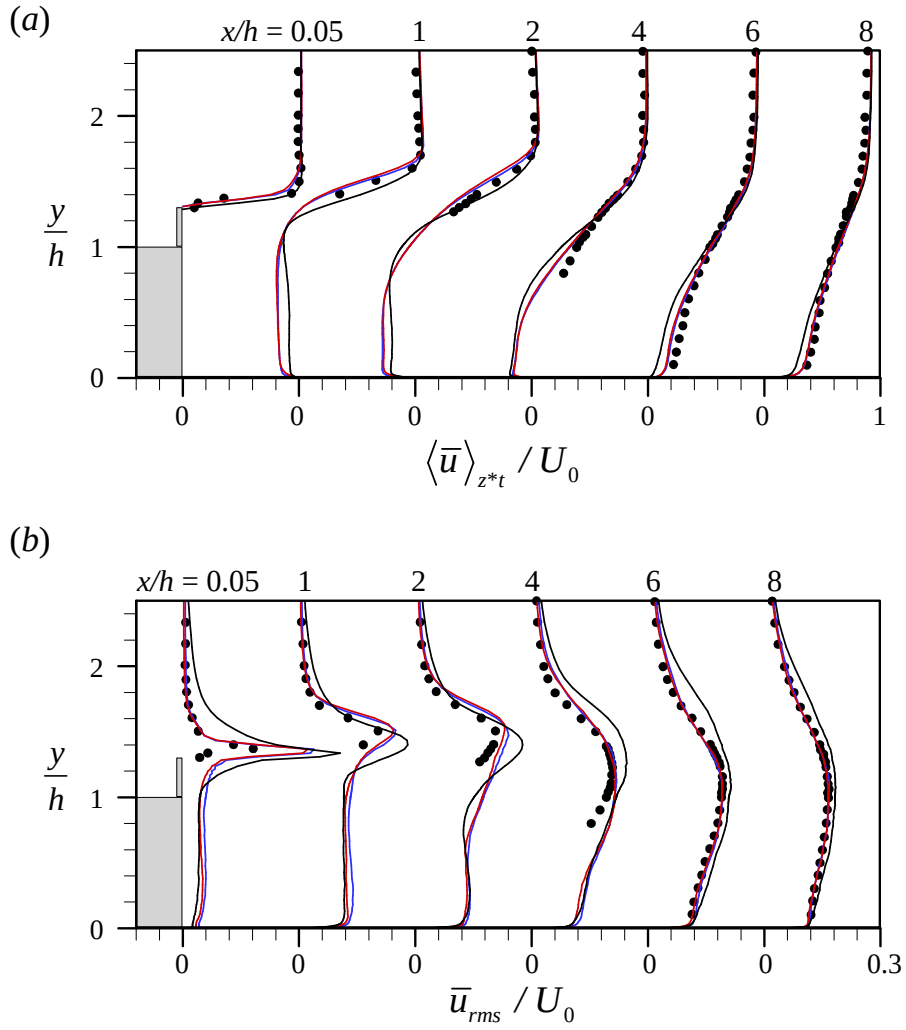

FIGURE 4.4. LES results for the controlled flow with $\lambda = 2.335h$ at the center of the tap ($z^* = 0$): (*a*) mean streamwise velocity; (*b*) rms streamwise velocity fluctuation. ●, experiment (Park *et al.* 2007); —, noSGS; —, DSM; —, NN1. Here, $\langle\rangle_{z^*t}$ denotes the averaging over the same z^* position and time.

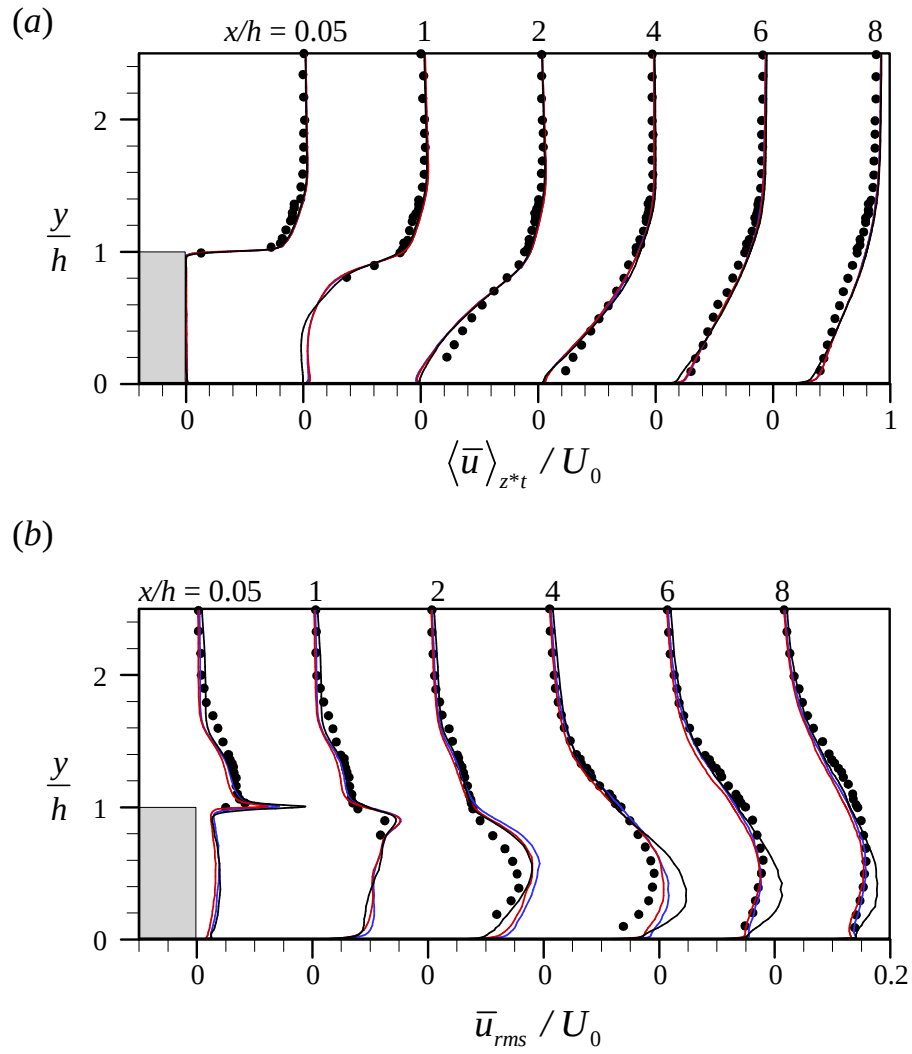

FIGURE 4.5. LES results for the controlled flow with $\lambda = 2.335h$ at middle of two adjacent tabs ($z^* = 0.5$): (*a*) mean streamwise velocity; (*b*) rms streamwise velocity fluctuation. ●, experiment (Park *et al.* 2007); —, noSGS; —, DSM; —, NN1.

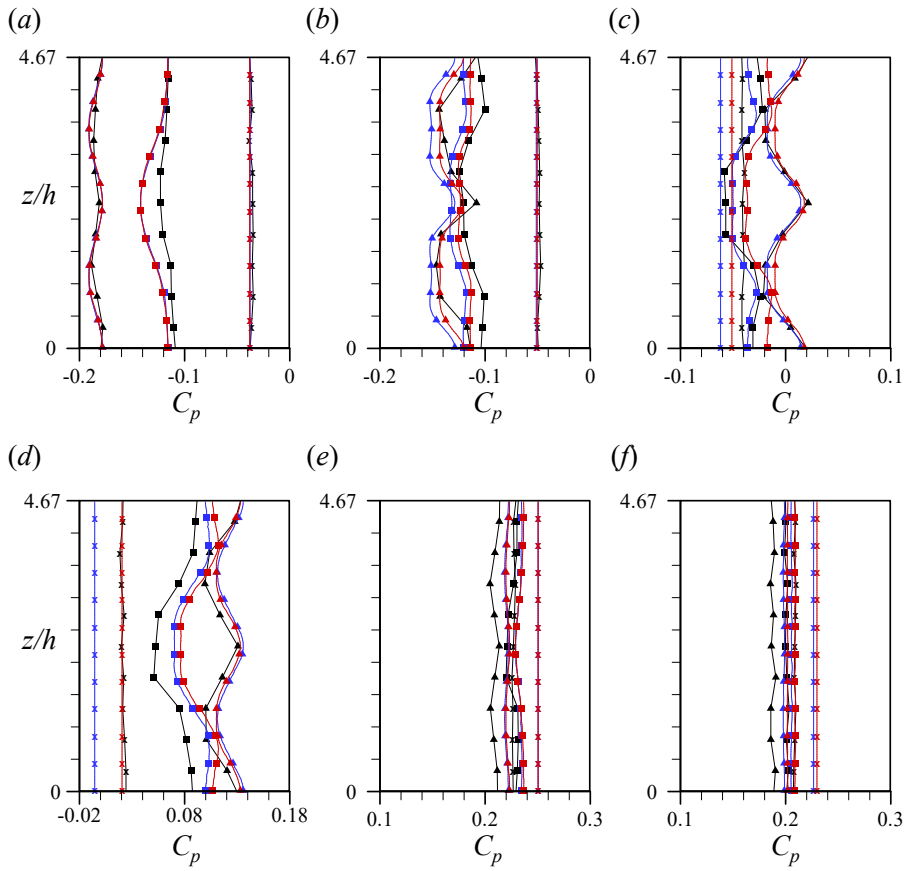

FIGURE 4.6. Spanwise distribution of the wall-pressure coefficient C_p with multiple taps at several streamwise locations: (*a*) $x/h = 1$; (*b*) $x/h = 2.5$; (*c*) $x/h = 3.5$; (*d*) $x/h = 4.5$; (*e*) $x/h = 8$; (*f*) $x/h = 12$. The lines with cross, square and triangle denote the uncontrolled flow, controlled flow with $\lambda = 4.67h$ and controlled flow with $\lambda = 2.335h$, respectively. The black, blue and red colors denote the experiment (Park *et al.* 2007), DSM and NN1, respectively.

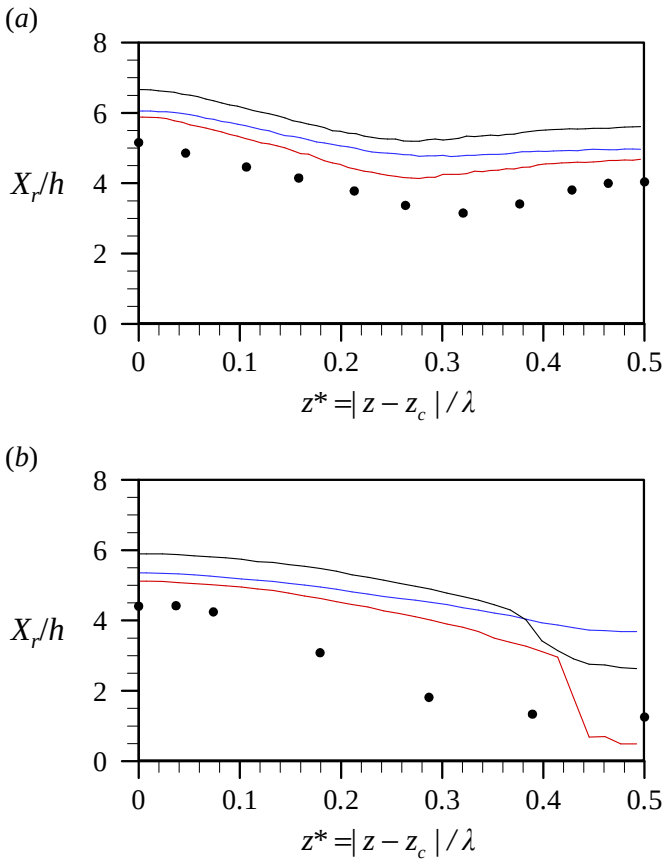

FIGURE 4.7. Spanwise variation of the reattachment length with multiple taps: (*a*) controlled flow with $\lambda = 4.67h$; (*b*) controlled flow with $\lambda = 2.335h$. ●, experiment (Park *et al.* 2007); —, noSGS; —, DSM; — NN1. Note that X_r's for the uncontrolled flow are $5.8h, 6.66h, 6.45h$ and $6.02h$ for the experiment, noSGS, DSM and NN1, respectively.

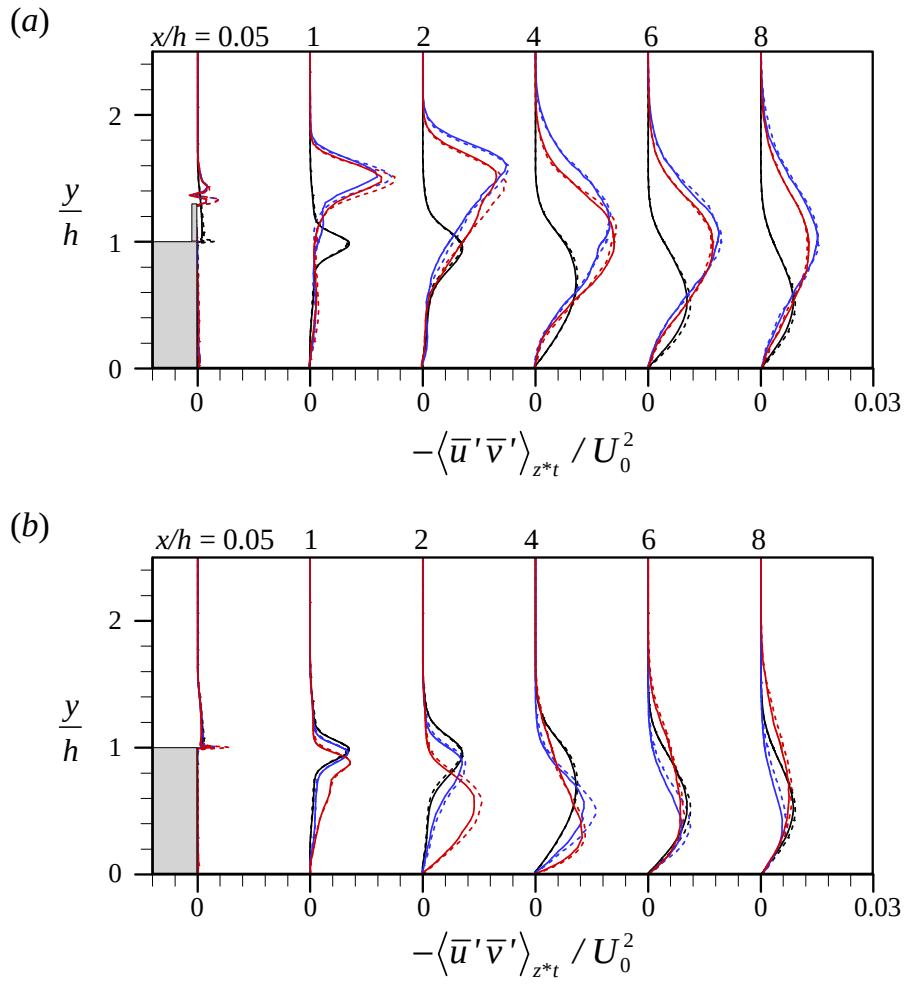

FIGURE 4.8. The Reynolds shear stress from the LES with DSM (dashed lines) and NN1 (solid lines): (*a*) at the center of the tab ($z^* = 0$); (*b*) at the middle of two adjacent tabs ($z^* = 0.5$). The black, blue and red colors denote the uncontrolled flow, controlled flow with $\lambda = 4.67h$ and controlled flow with $\lambda = 2.335h$, respectively.

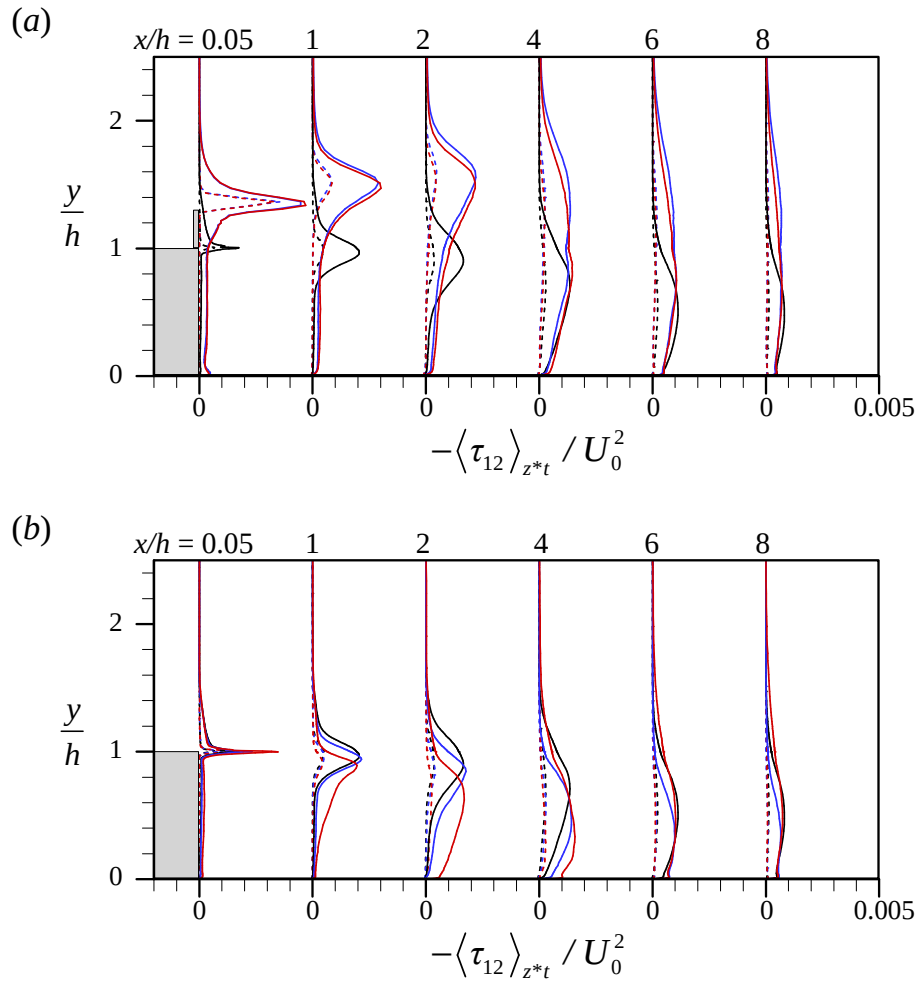

FIGURE 4.9. The SGS shear stress from the LES with DSM (dashed lines) and NN1 (solid lines): (*a*) at the center of the tab ($z^* = 0$); (*b*) at the middle of two adjacent tabs ($z^* = 0.5$). The black, blue and red colors denote the uncontrolled flow, controlled flow with $\lambda = 4.67h$ and controlled flow with $\lambda = 2.335h$, respectively.

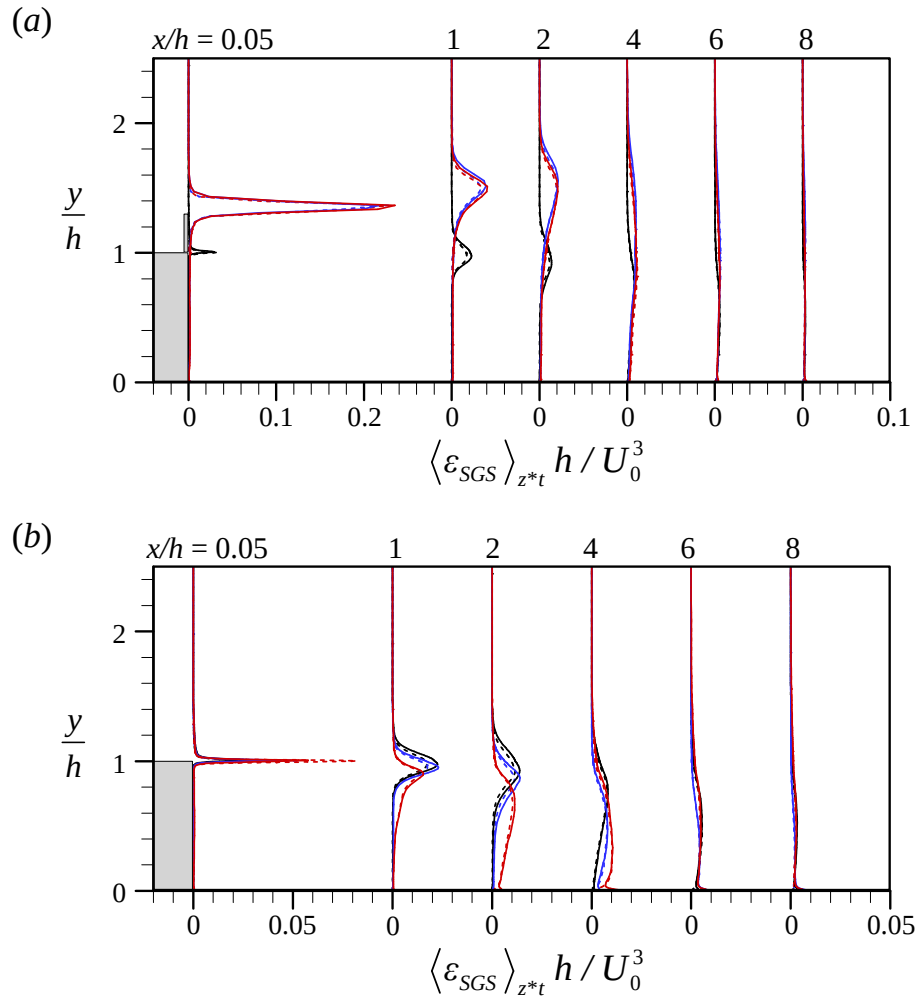

FIGURE 4.10. The SGS dissipation from the LES with DSM (dashed lines) and NN1 (solid lines): (*a*) at the center of the tab ($z^* = 0$); (*b*) at the middle of two adjacent tabs ($z^* = 0.5$). The black, blue and red colors denote the uncontrolled flow, controlled flow with $\lambda = 4.67h$ and controlled flow with $\lambda = 2.335h$, respectively.

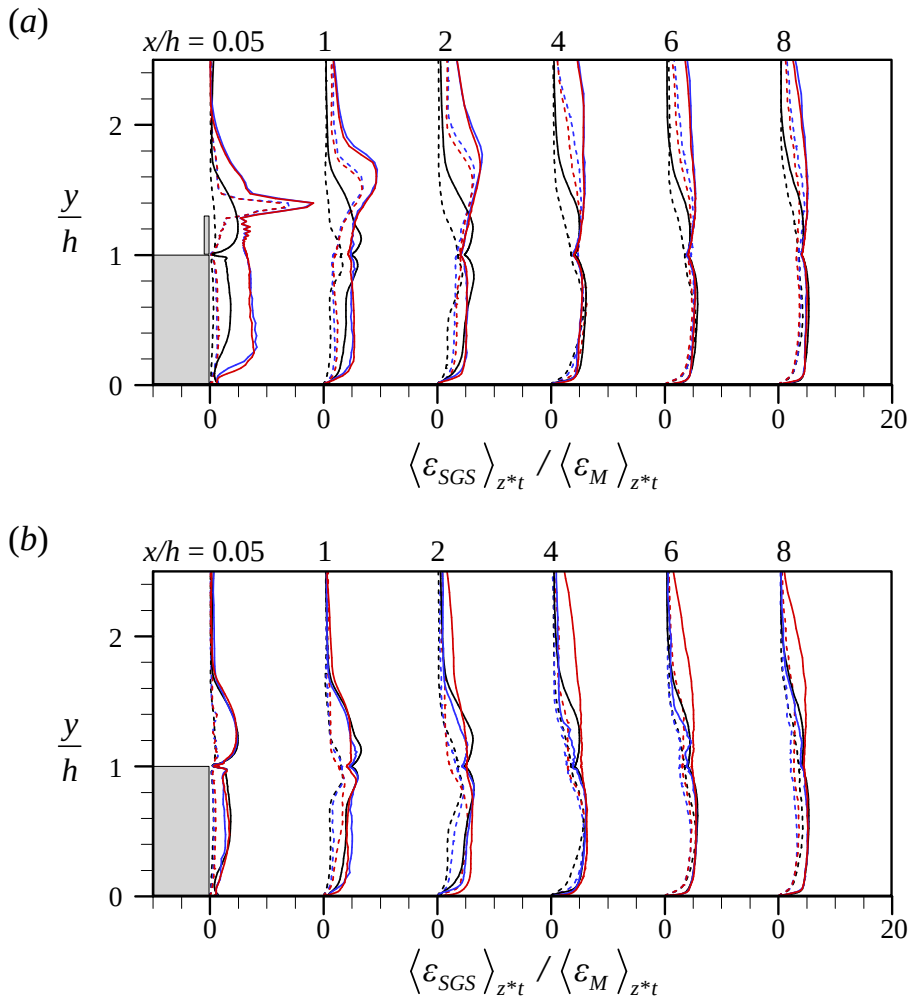

FIGURE 4.11. The ratio of SGS dissipation to molecular dissipation from the LES with DSM (dashed lines) and NN1(solid lines): (*a*) at the center of the tab ($z^* = 0$); (*b*) at the middle of two adjacent tabs ($z^* = 0.5$). The black, blue and red colors denote the uncontrolled flow, controlled flow with $\lambda = 4.67h$ and controlled flow with $\lambda = 2.335h$, respectively.

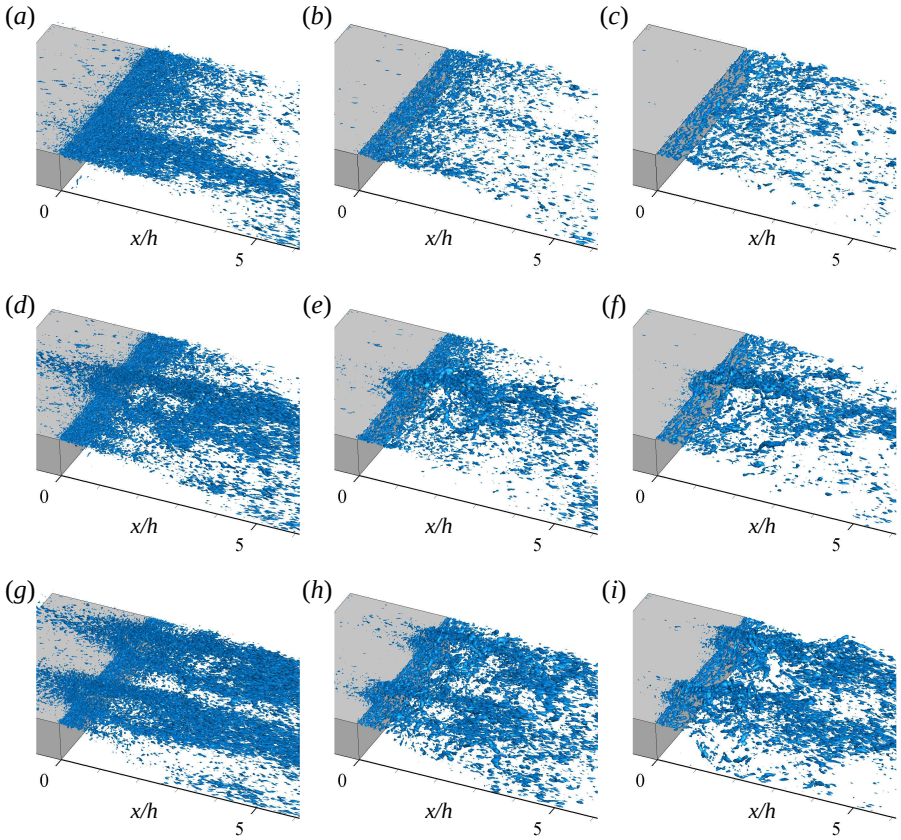

FIGURE 4.12. Instantaneous vortical structures from the LES with noSGS, DSM and NN1: $(a-c)$ uncontrolled flow; $(d-f)$ controlled flow with $\lambda = 4.67h$; $(g-i)$ controlled flow with $\lambda = 2.335h$. (a, d, g), (b, e, h) and (c, f, i) are the results of noSGS, DSM and NN1, respectively.

Chapter 5

Concluding remarks

In the present study, we applied a fully-connected neural network (NN) to the modeling of a subgrid-scale (SGS) stress for turbulent flow over a backward-facing step (BFS). Based on the NN-based SGS modeling conducted in the turbulent channel flow (Part I, Park & Choi 2021), two different NNs were trained with filtered DNS data at $Re_h = 5100$, where the input variables considered were the strain-rate and velocity-gradient tensors at single grid point (NN1 and NN2, respectively). The results in Part I indicated that the performance of NN for *a priori* test is not consistent with that for the actual large eddy simulation (LES), so we conducted *a priori* test only to check the convergence of the prediction performance of NN by varying its numbers of hidden layers and neurons. *A priori* test showed that two hidden layers with 32 neurons per layer were sufficient for both NN1 and NN2 to yield converged prediction performance for the mean SGS stress and SGS dissipation. These NN1 and NN2 were applied to the LES of BFS flow at $Re_h = 5100$, and showed good prediction performance for the reattachment length (X_r), where the NN1 and NN2 provided $X_r = 5.96h$ and $6.21h$, respectively ($X_r = 6.0h \pm 0.15h$ from the experiment by Jovic & Driver

1994 and $X_r = 6.17h$ from the present filtered DNS). The predictions for root-mean-square velocity fluctuation were also generally good as compared to those from LES with the dynamic Smagorinsky model (DSM). Then, we applied those NNs to the LES at $Re_h = 5100$ with a coarser grid resolution than that of the training data. The results were generally good as compared to those from LES with the DSM, where the NNs predicted the reattachment length better than the DSM. Meanwhile, we additionally trained the NNs with two different filtered DNS datasets together to improve the performance in the coarse-grid LES, as done in Part I. However, the improvement in this LES was not significant, and this might be because, unlike the turbulent channel flow, various filter sizes were already used to construct one fDNS dataset.

To assess the performance of the NN for a higher-Reynolds-number flow, we applied the NN1 trained at $Re_h = 5100$ to LES at $Re_h = 24000$. Although the Reynolds number and grid resolution were not the same as those of the training data, the LES on this Reynolds number provided fairly good results, compared to those from the experiment (Park *et al.* 2007) and LES with DSM. For example, the reattachment length was better predicted by the NN1 ($X_r = 6.02h$) than by the DSM ($X_r = 6.45h$) comparing to that of the experiment ($X_r = 5.8h \pm 0.25h$). Therefore, the NN trained at a lower-Reynolds-number BFS flow maintained its prediction performance for a high-Reynolds-number BFS flow. This might indicate that in the separated flows, the relation between the SGS stress and strain rate did not vary significantly by the Reynolds number. Finally, we applied the NN1 for the LES of controlled BFS flow by multiple taps installed at the step edge. At the Reynolds number of $Re_h = 24000$, we used taps having similar geometries to those of the experiment (Park *et al.* 2007), and the LES with NN1 could provide good results, where the amount of reduction of the reattachment length was better predicted by NN1 than by DSM.

In the present study, an NN-based SGS modeling was developed for turbulent channel (Part I) and backward-facing-step (Part II) flows and showed a promising LES resulting using the developed model. However, limitations of NN-based SGS modeling or NN-based LES was also clearly observed. So, let us discuss current limitations of NN-based LES and future research directions. Some limitations were also reported in Wollblad & Davidson (2008), Gamahara & Hattori (2017) and Zhou *et al.* (2019). First, the performance of NN-based SGS model depends on the input variables. In the present study, we considered the filtered strain-rate tensor $\bar{S}_{ij}$ and filtered velocity gradient tensor $\bar{\alpha}_{ij}$ as input variables, and showed that $\bar{S}_{ij}$ performs better than $\bar{\alpha}_{ij}$ in turbulent channel flow. Since the SGS stress tensor τ_{ij} is a symmetric tensor, one may also consider other combinations of $\bar{S}_{ij}$ and $\bar{R}_{ij}$ (filtered rotation rate tensor) as input variables, as described in §2.1. So, a further study in this direction is needed. Second, the results of *a priori* and *a posteriori* tests on NN-based SGS models are inconsistent with each other. Traditional physics-based SGS models have also the same inconsistency. That is, some traditional SGS models having a poor performance in *a priori* test perform very well in *a posteriori* test. However, this poor performance in *a priori* test does not mean the failure of such models, but indicates the fundamental limitation of *a priori* test itself (Park *et al.* 2005). The present NN-based SGS model is constructed using a database containing static (i.e., instantaneous) flow information, thus lacking dynamic (i.e., temporal) information of filtered flow variables which is important in actual LES (i.e., *a posteriori* test). Therefore, the present model is not free from the inconsistency observed in traditional SGS models, and a database containing more static information does not necessarily provide better output. In this regard, a different approach of constructing NN-based SGS models may be searched for. In traditional physics-based SGS modeling, Meneveau *et al.* (1996) proposed to accu-

mulate the flow information over flow pathlines and constructed a Lagrangian dynamic SGS model. Thus, a Lagrangian approach or reinforcement learning with a target statistics may be a way to overcome this inconsistency. To the best of our knowledge, there has been no attempt of constructing such an NN-based SGS model. This approach may provide an improved performance in NN-based LES. Third, an NN-based SGS model should be trained by databases containing different flow characteristics such as shear-driven, rotation-driven, and separated flow characteristics. The present SGS model was trained by a database of turbulent channel flow, and thus may not be applicable to other types of flows. Thus, more databases should be generated and used for training an NN. Here, we do not mean that almost all the flow databases should be trained for successful LES, but we suggest that some representative flow databases such as rotating channel flow, flow over a backward-facing step, flow over a circular cylinder and jet may be sufficient to build a successful NN for flow inside/over a complex geometry. However, how to combine different flow databases in an NN-based SGS model is still a difficult problem. The present NN-based SGS model was trained by the input and output variables normalized by wall units, but it may not be applicable to complex flow (e.g., a circular cylinder) because this flow cannot be scaled in wall units. To overcome this limitation, one should develop a universal non-dimensionalization of input and output variables for different flow types. This is an important task for the use of NN-based SGS model to flow inside/over a complex geometry.

References

ADAMS, E. W., JOHNSTON, J. P. & EATON, J. K. 1984 Experiments on the structure of turbulent reattaching flow. *Rep.* MD-43. Thermosciences Division, Department of Mechanical Engineering, Stanford University.

ADRIAN, R. J. 1990 Stochastic estimation of sub-grid scale motions. *Appl. Mech. Rev.* **43**, 214–218.

ADRIAN, R. J., JONES, B. G., CHUNG, M. K., HASSAN, Y., NITHIANANDAN, C. K. & TUNG, A. T.-C. 1989 Approximation of turbulent conditional averages by stochastic estimation. *Phys. Fluids* **1**, 992–998.

AIDER, J.-L., DANET, A. & LESIEUR, M. 2007 Large-eddy simulation applied to study the influence of upstream conditions on the time-dependant and averaged characteristics of a backward-facing step flow. *J. Turbul.* **8**, N51.

AKHAVAN, R., ANSARI, A., KANG, S. & MANGIAVACCHI, N. 2000 Subgrid-scale interactions in a numerically simulated planar turbulent jet and implications for modelling. *J. Fluid Mech.* **408**, 83–120.

AKSELVOLL, K. & MOIN, P. 1995 Large eddy simulation of turbulent confined coannular jets and turbulent flow over a backward facing step. *Rep.* TF-63. Thermosciences Division, Department of Mechanical Engineering, Stanford University.

ANDERSON, B. W. & DOMARADZKI, J. A. 2012 A subgrid-scale model for large-eddy simulation based on the physics of interscale energy transfer in turbulence. *Phys. Fluids* **24**, 065104.

AVANCHA, R. V. R. & PLETCHER, R. H. 2002 Large eddy simulation of the turbulent

flow past a backward-facing step with heat transfer and property variations. *Intl J. Heat Fluid Flow* **23**, 601–614.

BAE, H. J., LOZANO-DURÁN, A., BOSE, S. T. & MOIN, P. 2018 Turbulence intensities in large-eddy simulation of wall-bounded flows. *Phys. Rev. Fluids* **3**, 014610.

BARDINA, J., FERZIGER, J. H. & REYNOLDS, W. C. 1980 Improved subgrid scale models for large-eddy simulation. *AIAA Paper* 80-1357.

BECK, A., FLAD, D. & MUNZ, C. 2019 Deep neural networks for data-driven LES closure models. *J. Comput. Phys.* **398**, 108910.

BEDFORD, K. W. & YEO, W. K. 1993 Conjunctive filtering procedures in surface water flow and transport. In *Large eddy Simulation of Complex Engineering and Geophysical Flows* (ed. B. Galperin & S. A. Orszag), pp. 513–539. Cambridge University Press.

BHATTACHARJEE, S., SCHEELKE, B. & TROUTT, T. R. 1986 Modification of vortex interactions in a reattaching separated flow. *AIAA J.* **24**, 623–629.

CHEN, L., ASAI, K., NONOMURA, T., XI, G. & LIU, T. 2018 A review of backward-facing step (BFS) flow mechanisms, heat transfer and control. *Thermal Sci. Eng. Prog.* **6**, 194–216.

CHUN, K. B. & SUNG, H. J. 1996 Control of turbulent separated flow over a backward-facing step by local forcing. *Exp. Fluids* **21**, 417–426.

CLARK, R. A., FERZIGER, J. H. & REYNOLDS, W. C. 1979 Evaluation of subgrid-scale models using an accurately simulated turbulent flow. *J. Fluid Mech.* **91**, 1–16.

DOMARADZKI, J. A. & SAIKI, E. M. 1997 A subgrid-scale model based on the estimation of unresolved scales of turbulence. *Phys. Fluids* **9**, 2148–2164.

DURST, F. & SCHMITT, F. S. 1985 Experimental study of high Reynolds number backward-facing step flow. In *Proc. 5th symp. on turbulent shear flows*. Cornell University.

EATON, J. K. & JOHNSTON, J. P. 1980 Turbulent flow reattachment: An experimental study of the flow and structure behind a backward-facing step. *Rep.* MD-39. Thermosciences Division, Department of Mechanical Engineering, Stanford University.

EATON, J. K. & JOHNSTON, J. P. 1981 A review of research on subsonic turbulent flow reattachment. *AIAA J.* **19**, 1093–1100.

FOSS, J. K. & ZAMAN, K. B. M. Q. 1999 Large- and small-scale vortical motions in a shear layer perturbed by tabs. *J. Fluid Mech.* **382**, 307–329.

FRIEDRICH, R. & ARNAL, M. 1990 Analysing turbulent backward-facing step flow with the lowpass-filtered Navier-Stokes equations. *J. Wind Eng. Ind. Aerodyn.* **35**, 101–128.

GAI, S. L. & SHARMA, S. D. 1984 Subsonic turbulent flow over a rearward facing segmented step. *Phys Fluids* **27**, 544–546.

GAMAHARA, M. & HATTORI, Y. 2017 Searching for turbulence models by artificial neural network. *Phys. Rev. Fluids* **2**, 054604.

GAUTIER, N. & AIDER, J.-L. 2013 Control of the separated flow downstream of a backward-facing step using visual feedback. *Proc. R. Soc. A* **469**, 20130404.

GERMANO, M., PIOMELLI, U., MOIN, P. & CABOT, W. H. 1991 A dynamic subgrid-scale eddy viscosity model. *Phys. Fluids* **3**, 1760–1765.

GHOSAL, S., LUND, T. S., MOIN, P. & AKSELVOLL, K. 1995 A dynamic localization model for large-eddy simulation of turbulent flows. *J. Fluid Mech.* **286**, 229–255.

HÄRTEL, C., KLEISER, L., UNGER, F. & FRIEDRICH, R. 1994 Subgrid-scale energy transfer in the near-wall region of turbulent flows. *Phys. Fluids* **6**, 3130–3143.

HASAN, M. A. Z. & KHAN, A. S. 1992 On the instability characteristics of a reattaching shear layer with nonlaminar separation. *Intl J. Heat Fluid Flow* **13**, 224–231.

HASTIE, T., TIBSHIRANI, R. & FRIEDMAN, J. H. 2009 *The elements of statistical learning: Data mining, inference, and prediction.*, 2nd edn. Springer.

HORIUTI, K. 1997 A new dynamic two-parameter mixed model for large-eddy simulation. *Phys. Fluids* **9**, 3443–3464.

INAGAKI, M., KONDOH, T. & NAGANO, Y. 2005 A mixed-time-scale SGS model with fixed model-parameters for practical LES. *J. Fluids Eng.* **127**, 1–13.

IOFFE, S. & SZEGEDY, C. 2015 Batch normalization: Accelerating deep network training by reducing internal covariate shift. arXiv:1502.03167.

ISOMOTO, K. & HONAMI, S. 1989 The effect of inlet turbulence intensity on the reattachment process over a backward-facing step. *J. Fluids Eng.* **111**, 87–92.

JEONG, J. & HUSSAIN, F. 1995 On the identification of a vortex. *J. Fluid Mech.* **285**, 69–94.

JIMÉNEZ, J. & MOSER, R. D. 2000 Large-eddy simulations: Where are we and what can we expect? *AIAA J.* **38**, 605–612.

JOVIC, S. & DRIVER, D. M. 1994 Backward-facing step measurement at low Reynolds number, $Re_h = 5000$. *NASA Tech. Mem.* 108807.

KANG, S. & CHOI, H. 2002 Suboptimal feedback control of turbulent flow over a backward-facing step. *J. Fluid Mech.* **463**, 201–227.

KEATING, A., PIOMELLI, U., BREMHORST, K. & NEŠIĆ, S. 2004 Large-eddy simulation of heat transfer downstream of a backward-facing step. *J. Turbul.* **5**, N20.

KIM, B. N. & CHUNG, M. K. 1995 Experimental study of roughness effects on the separated flow over a backward-facing step. *AIAA J.* **33**, 159–161.

KIM, J., KIM, D. & CHOI, H. 2001 An immersed-boundary finite-volume method for simulations of flow in complex geometries. *J. Comput. Phys.* **171**, 132–150.

KIM, J., KLINE, S. J. & JOHNSTON, J. P. 1980 Investigation of a reattaching turbulent shear layer: Flow over a backward-facing step. *J. Fluids Eng.* **102**, 302–308.

KIM, J., MOIN, P. & MOSER, R. 1987 Turbulence statistics in fully developed channel flow at low Reynolds number. *J. Fluid Mech.* **177**, 133–166.

KINGMA, D. P. & BA, J. 2014 Adam: A method for stochastic optimization. arXiv:1412.6980.

KOBAYASHI, T., MORINISHI, Y. & OH, K.-J. 1992 Large eddy simulation of backward-facing step flow. *Commu. Appl. Num. Methods* **8**, 431–441.

LANGFORD, J. A. & MOSER, R. D. 1999 Optimal LES formulations for isotropic turbulence. *J. Fluid Mech.* **398**, 321–346.

LANGFORD, J. A. & MOSER, R. D. 2004 Optimal large-eddy simulation results for isotropic turbulence. *J. Fluid Mech.* **521**, 273–294.

LE, H. & MOIN, P. 1994 Direct numerical simulation of turbulent flow over a backward-

facing step. *Rep.* TF-58. Thermosciences Division, Department of Mechanical Engineering, Stanford University.

LE, H., MOIN, P. & KIM, J. 1997 Direct numerical simulation of turbulent flow over a backward-facing step. *J. Fluid Mech.* **330**, 349–374.

LECUN, Y., BENGIO, Y. & HINTON, G. E. 2015 Deep learning. *Nature* **521**, 436–444.

LEE, J., CHOI, H. & PARK, N. 2010 Dynamic global model for large eddy simulation of transient flow. *Phys. Fluids* **22**, 075106.

LEITH, C. E. 1968 Diffusion approximation for two-dimensional turbulence. *Phys. Fluids* **11**, 671–672.

LILLY, D. K. 1992 A proposed modification of the Germano subgrid-scale closure method. *Phys. Fluids* **4**, 633–635.

LIU, S., MENEVEAU, C. & KATZ, J. 1994 On the properties of similarity subgrid-scale models as deduced from measurements in a turbulent jet. *J. Fluid Mech.* **275**, 83–119.

LIU, S., MENEVEAU, C. & KATZ, J. 1995 Experimental study of similarity subgrid-scale models of turbulence in the far-field of a jet. *Appl. Sci. Res.* **54**, 177–190.

LUND, T. S. & NOVIKOV, E. A. 1992 Parameterization of subgrid-scale stress by the velocity gradient tensor. In *Annual Research Briefs, Center for Turbulence Research, Stanford University*, pp. 27–43.

LUND, T. S., WU, X. & SQUIRES, K. D. 1998 Generation of turbulent inflow data for spatially-developing boundary layer simulations. *J. Comput. Phys.* **140**, 233–258.

MAULIK, R. & SAN, O. 2017 A neural network approach for the blind deconvolution of turbulent flows. *J. Fluid Mech.* **831**, 151–181.

MAULIK, R., SAN, O., RASHEED, A. & VEDULA, P. 2018 Data-driven deconvolution for large eddy simulations of Kraichnan turbulence. *Phys. Fluids* **30**, 125109.

MAULIK, R., SAN, O., RASHEED, A. & VEDULA, P. 2019 Subgrid modelling for two-dimensional turbulence using neural networks. *J. Fluid Mech.* **858**, 122–144.

MENEVEAU, C. & KATZ, J. 2000 Scale-invariance and turbulence models for large-eddy simulation. *Annu. Rev. Fluid Mech.* **32**, 1–32.

MENEVEAU, C., LUND, T. S. & CABOT, W. H. 1996 A Lagrangian dynamic subgrid-scale model of turbulence. *J. Fluid Mech.* **319**, 353–385.

MERI, A. & WENGLE, H. 2002 DNS and LES of turbulent backward-facing step flow using 2nd- and 4th-order discretization. In *Advances in LES of Complex Flows* (ed. R. Friedrich & W. Rodi), pp. 99–114. Springer Netherlands.

MÉTAIS, O. & LESIEUR, M. 1992 Spectral large-eddy simulation of isotropic and stably stratified turbulence. *J. Fluid Mech.* **239**, 157–194.

MOSER, R. D., KIM, J. & MANSOUR, N. N. 1999 Direct numerical simulation of turbulent channel flow up to $Re_\tau = 590$. *Phys. Fluids* **11**, 943–945.

MOSER, R. D., MALAYA, N. P., CHANG, H., ZANDONADE, P. S., VEDULA, P., BHATTACHARYA, A. & HASELBACHER, A. 2009 Theoretically based optimal large-eddy simulation. *Phys. Fluids* **21**, 105104.

NAIR, V. & HINTON, G. E. 2010 Rectified linear units improve restricted Boltzmann machines. In *Proceedings of the 27th International Conference on Machine Learning* (ed. J. Fürnkranz & T. Joachims), pp. 807–814. Omnipress.

NETO, A. S., GRAND, D., MÉTAIS, O. & LESIEUR, M. 1993 A numerical investigation of the coherent vortices in turbulence behind a backward-facing step. *J. Fluid Mech.* **256**, 1–25.

NEUMANN, J. & WENGLE, H. 2003 DNS and LES of passively controlled turbulent backward-facing step flow. *Flow, Turbul. Combus.* **71**, 297–310.

NICOUD, F. & DUCROS, F. 1999 Subgrid-scale stress modelling based on the square of the velocity gradient tensor. *Flow Turb. Combust.* **62**, 183–200.

NICOUD, F., TODA, H. B., CABRIT, O., BOSE, S. & LEE, J. 2011 Using singular values to build a subgrid-scale model for large eddy simulations. *Phys. Fluids* **23**, 085106.

PAL, A. 2019 Deep learning parameterization of subgrid scales in wall-bounded turbulent flows. arXiv:1905.12765.

PANJWANI, B., ERTESVÅG, I. S., GRUBER, A. & RIAN, K. 2009 Large eddy simulation of backward facing step flow. In *5th National Conference on Computational Mechanics, MekIT09* (ed. B. Skallerud & H. I. Andersson), pp. 353–370.

PARK, H., JEON, W.-P., CHOI, H. & YOO, J. Y. 2007 Mixing enhancement behind a backward-facing step using tabs. *Phys. Fluids* **19**, 105103.

PARK, J. & CHOI, H. 2021 Toward neural-network-based large eddy simulation: Application to turbulent channel flow. *J. Fluid Mech.* **914**, A16.

PARK, N., LEE, S., LEE, J. & CHOI, H. 2006 A dynamic subgrid-scale eddy viscosity model with a global model coefficient. *Phys. Fluids* **18**, 125109.

PARK, N., YOO, J. Y. & CHOI, H. 2005 Toward improved consistency of *a priori* tests with *a posteriori* tests in large eddy simulation. *Phys. Fluids* **17**, 015103.

PASSALIS, N., TEFAS, A., KANNIAINEN, J., GABBOUJ, M. & IOSIFIDIS, A. 2019 Deep adaptive input normalization for time series forecasting. arXiv:1902.07892.

PAWAR, S., SAN, O., RASHEED, A. & VEDULA, P. 2020 *A priori* analysis on deep learning of subgrid-scale parameterizations for Kraichnan turbulence. *Theor. Comput. Fluid Dyn.* **40**, 120–132.

PIOMELLI, U., CABOT, W. H., MOIN, P. & LEE, S. 1991 Subgrid-scale backscatter in turbulent and transitional flows. *Phys. Fluids* **3**, 1766–1771.

PIOMELLI, U. & LIU, J. 1995 Large-eddy simulation of rotating channel flows using a localized dynamic model. *Phys. Fluids* **7**, 839–848.

PIOMELLI, U., YU, Y. & ADRIAN, R. J. 1996 Subgrid-scale energy transfer and near-wall turbulence structure. *Phys. Fluids* **8**, 215–224.

POPE, S. B. 2000 *Turbulent Flows*. Cambridge University Press.

RASTHOFER, U. & GRAVEMEIER, V. 2013 Multifractal subgrid-scale modeling within a variational multiscale method for large-eddy simulation of turbulent flow. *J. Comput. Phys.* **234**, 79–107.

ROOS, F. W. & KEGELMAN, J. T. 1986 Control of coherent structures in reattaching laminar and turbulent shear layers. *AIAA J.* **24**, 1956–1963.

ROZEMA, W., BAE, H. J., MOIN, P. & VERSTAPPEN, R. 2015 Minimum-dissipation models for large-eddy simulation. *Phys. Fluids* **27**, 085107.

RUMELHART, D. E., HINTON, G. E. & WILLIAMS, R. J. 1986 Learning representations by back-propagating errors. *Nature* **323**, 533–536.

SALVETTI, M. V. & BANERJEE, S. 1995 *A priori* tests of a new dynamic subgrid-scale model for finite-difference large-eddy simulations. *Phys. Fluids* **7**, 2831–2847.

SARGHINI, F., DE FELICE, G. & SANTINI, S. 2003 Neural networks based subgrid scale modeling in large eddy simulations. *Comput. Fluids* **32**, 97–108.

SARGHINI, F., PIOMELLI, U. & BALARAS, E. 1999 Scale-similar models for large-eddy simulations. *Phys. Fluids* **11**, 1596–1607.

SCHLATTER, P. & ÖRLÜ, R. 2010 Assessment of direct numerical simulation data of turbulent boundary layers. *J. Fluid Mech.* **659**, 116–126.

SCHMITT, F. G. 2007 About Boussinesq's turbulent viscosity hypothesis: Historical remarks and a direct evaluation of its validity. *Comptes Rendus Mécanique* **335**, 617–627.

SCHUMANN, U. 1975 Subgrid scale model for finite difference simulations of turbulent flows in plane channels and annuli. *J. Comput. Phys.* **18**, 376–404.

SELBY, G. V., LIN, J. C. & HOWARD, F. G. 1990 Turbulent flow separation control over a backward-facing ramp via transverse and swept grooves. *J. Fluids Eng.* **112**, 238–240.

SILVIS, M. H., BAE, H. J., TRIAS, F. X., ABKAR, M. & VERSTAPPEN, R. 2019 A nonlinear subgrid-scale model for large-eddy simulations of rotating turbulent flows. arXiv:1904.12748.

SILVIS, M. H., REMMERSWAAL, R. A. & VERSTAPPEN, R. 2017 Physical consistency of subgrid-scale models for large-eddy simulation of incompressible turbulent flows. *Phys. Fluids* **29**, 015105.

SIMONS, E., MANNA, M. & BENOCCI, C. 2002 Parallel multi-domain large-eddy simulation of the flow over a backward-facing step at $Re = 5100$. In *Advances in LES of Complex Flows* (ed. R. Friedrich & W. Rodi), pp. 115–130. Springer Netherlands.

SMAGORINSKY, J. 1963 General circulation experiments with the primitive equations. *Monthly Weather Review* **91**, 99–164.

SPALART, P. R., DECK, S., SHUR, M. L., SQUIRES, K. D., STRELETS, M. KH. &

TRAVIN, A. 2006 A new version of detached-eddy simulation, resistant to ambiguous grid densities. *Theor. Comput. Fluid Dyn.* **20**, 181–195.

STOFFER, R., VAN LEEUWEN, C. M., PODAREANU, D., CODREANU, V., VEERMAN, M. A., JANSSENS, M., HARTOGENSIS, O. K. & VAN HEERWAARDEN, C. C. 2020 Development of a large-eddy simulation subgrid model based on artificial neural networks: A case study of turbulent channel flow. *Geosci. Model Dev. Discuss. (preprint)* **2020**, 1–29.

STOLZ, S. & ADAMS, N. A. 1999 An approximate deconvolution procedure for large-eddy simulation. *Phys. Fluids* **11**, 1699–1701.

THIRY, O. & WINCKELMANS, G. 2016 A mixed multiscale model better accounting for the cross term of the subgrid-scale stress and for backscatter. *Phys. Fluids* **28**, 025111.

TOSCHI, F., KOBAYASHI, H., PIOMELLI, U. & IACCARINO, G. 2006 Backward-facing step calculations using the shear improved Smagorinsky model. In *Proceedings of the Summer Program 2006 (Center for Turbulence Research, Stanford University)*, pp. 87–97.

TRIAS, F. X., FOLCH, D., GOROBETS, A. & OLIVA, A. 2015 Building proper invariants for eddy-viscosity subgrid-scale models. *Phys. Fluids* **27**, 065103.

TROPEA, C. 1982 Die turbulente Strömung in Flachkanälen und offenen Gerinen. *Dissertation, University of Karlsruhe* .

VERSTAPPEN, R. 2011 When does eddy viscosity damp subfilter scales sufficiently? *J. Sci. Comput* **49**, 94–110.

VERSTAPPEN, R.W.C.P., BOSE, S. T., LEE, J., CHOI, H. & MOIN, P. 2010 A dynamic eddy-viscosity model based on the invariants of the rate-of-strain. In *Proceedings of the Summer Program 2010 (Center for Turbulence Research, Stanford University)*, pp. 183–192.

VOGEL, J. C. & EATON, J. K. 1985 Combined heat transfer and fluid dynamic measurements downstream of a backward-facing step. *J. Heat Trans.* **107**, 922–929.

VÖLKER, S., MOSER, R. D. & VENUGOPAL, P. 2002 Optimal large eddy simulation

of turbulent channel flow based on direct numerical simulation statistical data. *Phys. Fluids* **14**, 3675–3691.

VOLLANT, A., BALARAC, G. & CORRE, C. 2017 Subgrid-scale scalar flux modelling based on optimal estimation theory and machine-learning procedure. *J. Turbulence* **18**, 854–878.

VREMAN, A. W. 2004 An eddy-viscosity subgrid-scale model for turbulent shear flow: Algebraic theory and applications. *Phys. Fluids* **16**, 3670–3681.

VREMAN, B., GEURTS, B. & KUERTEN, H. 1994 On the formulation of the dynamic mixed subgrid-scale model. *Phys. Fluids* **6**, 4057–4059.

VREMAN, B., GEURTS, B. & KUERTEN, H. 1997 Large-eddy simulation of the turbulent mixing layer. *J. Fluid Mech.* **339**, 357–390.

WANG, Z., LUO, K., LI, D., TAN, J. & FAN, J. 2018 Investigations of data-driven closure for subgrid-scale stress in large-eddy simulation. *Phys. Fluids* **30**, 125101.

WOLLBLAD, C. & DAVIDSON, L. 2008 POD based reconstruction of subgrid stresses for wall bounded flows using neural networks. *Flow Turb. Combust.* **81**, 77–96.

XIE, C., LI, K., MA, C. & WANG, J. 2019*a* Modeling subgrid-scale force and divergence of heat flux of compressible isotropic turbulence by artificial neural network. *Phys. Rev. Fluids* **4**, 104605.

XIE, C., WANG, J. & E, W. 2020*a* Modeling subgrid-scale forces by spatial artificial neural networks in large eddy simulation of turbulence. *Phys. Rev. Fluids* **5**, 054606.

XIE, C., WANG, J., LI, H., WAN, M. & CHEN, S. 2019*b* Artificial neural network mixed model for large eddy simulation of compressible isotropic turbulence. *Phys. Fluids* **31**, 085112.

XIE, C., WANG, J., LI, H., WAN, M. & CHEN, S. 2020*b* Spatial artificial neural network model for subgrid-scale stress and heat flux of compressible turbulence. *Theoret. Appl. Mech. Letters* **10**, 27–32.

XIE, C., WANG, J., LI, H., WAN, M. & CHEN, S. 2020*c* Spatially multi-scale artificial neural network model for large eddy simulation of compressible isotropic turbulence. *AIP Advances* **10**, 015044.

XIE, C., WANG, J., LI, K. & MA, C. 2019*c* Artificial neural network approach to large-eddy simulation of compressible isotropic turbulence. *Phys. Rev. E* **99**, 053113.

YANG, D., HE, S., SHEN, L. & LUO, X. 2020 Large eddy simulation coupled with immersed boundary method for turbulent flows over a backward facing step. In *Proc. Institution of Mech. Eng., Part C: J. Mech. Eng. Sci.*, p. 0954406220954892. IMECHE.

YOU, D. & MOIN, P. 2007 A dynamic global-coefficient subgrid-scale eddy-viscosity model for large-eddy simulation in complex geometries. *Phys. Fluids* **19**, 065110.

ZAMAN, K. B. M. Q., REEDER, M. F. & SAMIMY, M. 1994 Control of an axisymmetric jet using vortex generators. *Phys. Fluids* **6**, 778–793.

ZANDONADE, P. S., LANGFORD, J. A. & MOSER, R. D. 2004 Finite-volume optimal large-eddy simulation of isotropic turbulence. *Phys. Fluids* **16**, 2255–2271.

ZANG, Y., STREET, R. L. & KOSEFF, J. R. 1993 A dynamic mixed subgrid-scale model and its application to turbulent recirculating flows. *Phys. Fluids* **5**, 3186–3196.

ZHOU, Z., HE, G., WANG, S. & JIN, G. 2019 Subgrid-scale model for large-eddy simulation of isotropic turbulent flows using an artificial neural network. *Comput. Fluids* **195**, 104319.

Appendix A

Parametric study on the neural-network-based SGS model in turbulent channel flow

In the present appendix, results of several parametric studies on the neural network (NN) are presented, where the NN is trained with fDNS database of the turbulent channel flow at $Re_\tau = 178$. Details of fDNS database are presented in Part I §2.2. For five NNs trained with different input variables listed in Part I table 2.1, we first test the prediction performance of those NNs by varying the numbers of training data and hidden layers. Here, the number of neurons per hidden layer is fixed at 128, which are comparable or larger than those used in the previous NN-based SGS modeling in turbulent channel flow (Gamahara & Hattori 2017; Stoffer *et al.* 2020). Figure A.1 shows the mean SGS shear stress $\langle \tau_{xy} \rangle$ predicted by NNs from *a priori* test, where those NNs have two hidden layers. Here, N_{fDNS} is the number of instantaneous fDNS flow fields used for collecting training data, and one fDNS field contains 6,208 training data. For NN1 and NN2, $N_{\mathrm{fDNS}} = 50$ is sufficient, but $N_{\mathrm{fDNS}} = 200$ is required for NN3. Figure A.2 shows $\langle \tau_{xy} \rangle$ predicted by NN1 - NN5 from *a priori* test, where four different number of hidden layers ($N_{hl} = 1, 2, 3, 4$) are considered. A single hid-

den layer is sufficient for NN1 and NN2, but more than one hidden layer seems to be required for NN3 and NN5. Finally, we test the performance of NN1 - NN5 by varying both N_{fDNS} and N_{hl}, where $N_{\mathrm{fDNS}} = 200, 500$ and $N_{hl} = 2, 3, 4$ are considered. Figure A.3 shows $\langle \tau_{xy} \rangle$ from *a priori* test, and figures A.4 and A.5 show the mean velocity and Reynolds shear stress from *a posteriori* test. Computational details for *a posteriori* test are the same as those for LES178 case in Part I §3.2. The backscatter clipping by eq. (3.1) in Part I is used for LES with NN3 - NN5, because more hidden layers and training data do not reduce the backscatter produced by NN3 - NN5. For all NNs considered, two hidden layers and 200 fDNS fields are sufficient for showing converged prediction performance for the statistics considered. Therefore, $N_{hl} = 2$ and $N_{\mathrm{fDNS}} = 200$ are taken for the present study for all NNs considered in turbulent channel flow.

For NN3 - NN5, the numbers of input grid points in x and z directions, n_x and n_z respectively, have an effect on the prediction performance for the SGS stresses. Therefore, we test NN3 - NN5 for four different numbers of the input grid points $n_x = n_z = 3, 5, 7, 9$. Here, we also test two additional NNs (NN6 and NN7 hereafter) which have different input variables from those of NN3 - NN5, where NN6 and NN7 use only velocity components $\bar{u}_i$ at $n_x \times n_z$ and $n_x \times 3(y) \times n_z$ input grid points, respectively. Like NN3 - NN5, NN6 and NN7 predict six components of the SGS stress tensor, which is located at the center of input grid points considered. Figures A.6-A.8 show the results of *a priori* and *a posteriori* tests for NN3 - NN7 with different $n_x (= n_z)$. Here, the backscatter clipping is used for LES with those NNs because more input grid points for NN3 - NN7 do not make LES with these NNs stable. For NN3 - NN7 except NN6, $n_x = 3$ provides fairly good predictions for $\langle \tau_{xy} \rangle$ in *a priori* test. In the actual LES, $n_x = 3$ is sufficient for showing good prediction performance for the mean velocity and Reynolds shear stress for all NNs considered. Therefore, we determine to

use $n_x(=n_z)=3$ for NNs which use multiple input grid points, and the use of $n_x(=n_z)=3$ for NN3-NN5 is enough to compare their prediction performance to those of NN1-NN2 in Part I.

We have investigated the effects of bias, activation function, and differently initialized weights on the performance of the NN-based SGS model. For NN1 - NN5, we test three different usages of bias: 1) using bias at both hidden and output layers (Casebs1), 2) no bias at all layers (Casebs2), 3) using bias only at hidden layers (Casebs3). Figures A.9 and A.10 show the effect of bias on the mean SGS and Reynolds shear stresses from *a priori* and *a posteriori* tests, respectively. For all NNs considered, the bias has little effect on the prediction performance for those statistics. Figures A.11 and A.12 show the effect of activation function f_N on the mean SGS and Reynolds shear stresses from *a priori* and *a posteriori* tests, respectively, where ReLU, sigmoid and hyperbolic tangent functions are used. For all NNs considered, the prediction performance of NNs by different activation functions is almost similar. However, figure A.13 shows that the convergence of the loss function for the test dataset is faster using ReLU than using other functions, where the loss function is defined as eq. (2.4) in Part I. Therefore, we use ReLU as the activation function for all NNs considered. Figures A.14 and A.15 show the mean SGS and Reynolds shear stresses from *a priori* and *a posteriori* tests, respectively, where four different random seeds are used for the random initialization of trainable weights in NNs.

The output of NNs in Part I is six components of the SGS stress tensor τ_{ij}. It is also possible to train six NNs separately for predicting each component of SGS stress tensor, as done in previous study (Gamahara & Hattori 2017). Figure A.16 shows the effect of the different number of output components on the prediction performance of NN1 and NN2 for the $\langle\tau_{xy}\rangle$ and $\langle\varepsilon_{SGS}\rangle$ in *a priori* test. For those NNs, Case6o denotes the NN whose output is six components of

τ_{ij}, whereas Case1o denotes the NN whose output is one component of τ_{ij}. Note that to predict six components of τ_{ij}, Case1o requires six NNs, resulting in more computational time for the prediction of τ_{ij} than with Case6o. Figure A.17 shows the correlation coefficients between true and predicted τ_{ij} and ϵ_{SGS} from Case1o and Case6o. Overall, the correlation coefficients from Case6o are slightly lower than those from Case1o, but both cases have similar prediction performance for the mean SGS statistics. So, considering the computational cost in LES, we train NNs to predict six components of τ_{ij} at once.

The performance of an NN depends on the loss function to be minimized. We test several loss functions, which are defined as follows:

$$\mathrm{LFr} = \frac{1}{2N}\frac{1}{6}\sum^{N}\sum_{i\leq j}^{3}\left(\tau_{ij}^{\mathrm{fDNS}} - \tau_{ij}^{\mathrm{M}}\right)^2; \tag{A.1}$$

$$\mathrm{LF1} = \frac{1}{2N}\frac{1}{6}\sum^{N}\sum_{i\leq j}^{3}\left|\tau_{ij}^{\mathrm{fDNS}} - \tau_{ij}^{\mathrm{M}}\right|; \tag{A.2}$$

$$\mathrm{LF2} = \frac{1}{2N}\sum^{N}\left(\epsilon_{SGS}^{\mathrm{fDNS}} - \epsilon_{SGS}^{\mathrm{M}}\right)^2; \tag{A.3}$$

$$\mathrm{LF3} = \mathrm{LFr} + \mathrm{LF2}; \tag{A.4}$$

$$\mathrm{LF4} = \frac{1}{2N}\sum^{N}\left[0.5\left(\epsilon_{SGS}^{\mathrm{fDNS}} + \left|\epsilon_{SGS}^{\mathrm{fDNS}}\right|\right) - \epsilon_{SGS}^{\mathrm{M}}\right]^2; \tag{A.5}$$

$$\mathrm{LF5} = \mathrm{LFr} + \mathrm{LF4}, \tag{A.6}$$

where LFr is the reference loss function used in Part I, N is the number of mini-batch data. Here, the L2 norm regularization term of weights is used for all loss functions tested, but this term is omitted in above equations for clarity. Figures A.18-A.20 show the results of *a priori* test, showing the effect of different loss functions on the performance. The NNs trained with LF1 and LF3 do not show a significant difference in prediction performance from that with LFr. On the other hand, NNs with LF2 predict well the SGS dissipation, but show poor predictions

for the SGS shear stress. For NNs with LF4 and LF5, the backscatter is reduced, whereas the prediction performance for the SGS shear stress and dissipation is worse than that with LFr. In the actual LES, NNs with LF1 and LF3 provide almost similar results to those from NNs with LFr. For LF2, LES with NN1 and NN2 shows numerical instability which does not occur with LFr. Figure A.21 shows the mean velocity profile and Reynolds shear stress from LES with NNs trained by LFr, LF4 and LF5. In the case of LF4, all LES with NN1-NN5 do not diverge without backscatter clipping, but LESs with NN1 and NN2 provide very poor predictions for the mean velocity. In the case of LF5, LESs with NN3-NN5 diverge unless the backscatter clipping is used, and the LES results with LF5 are similar to those with LFr. Overall, NNs trained with loss functions of LF1-LF5 do not show better prediction performance in LES than those with LFr.

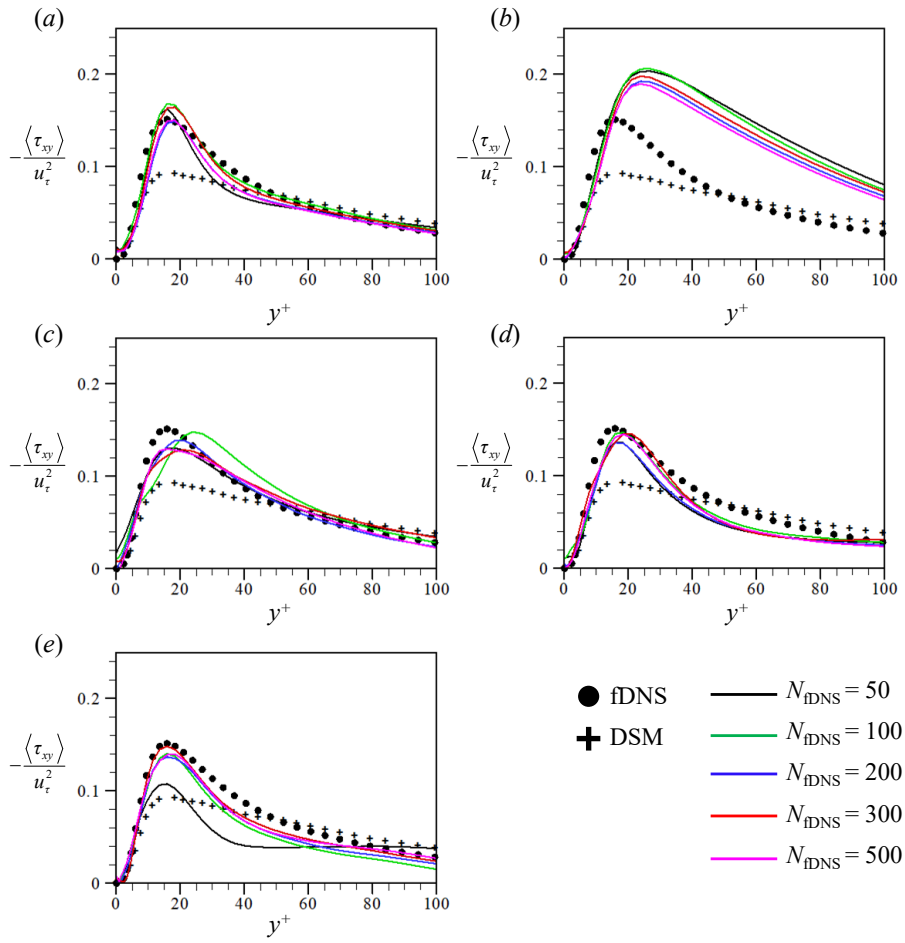

FIGURE A.1. Mean SGS shear stress predicted by NN1 - NN5 with different N_{fDNS} (*a priori* test at $Re_\tau = 178$): (*a*) NN1; (*b*) NN2; (*c*) NN3; (*d*) NN4; (*e*) NN5.

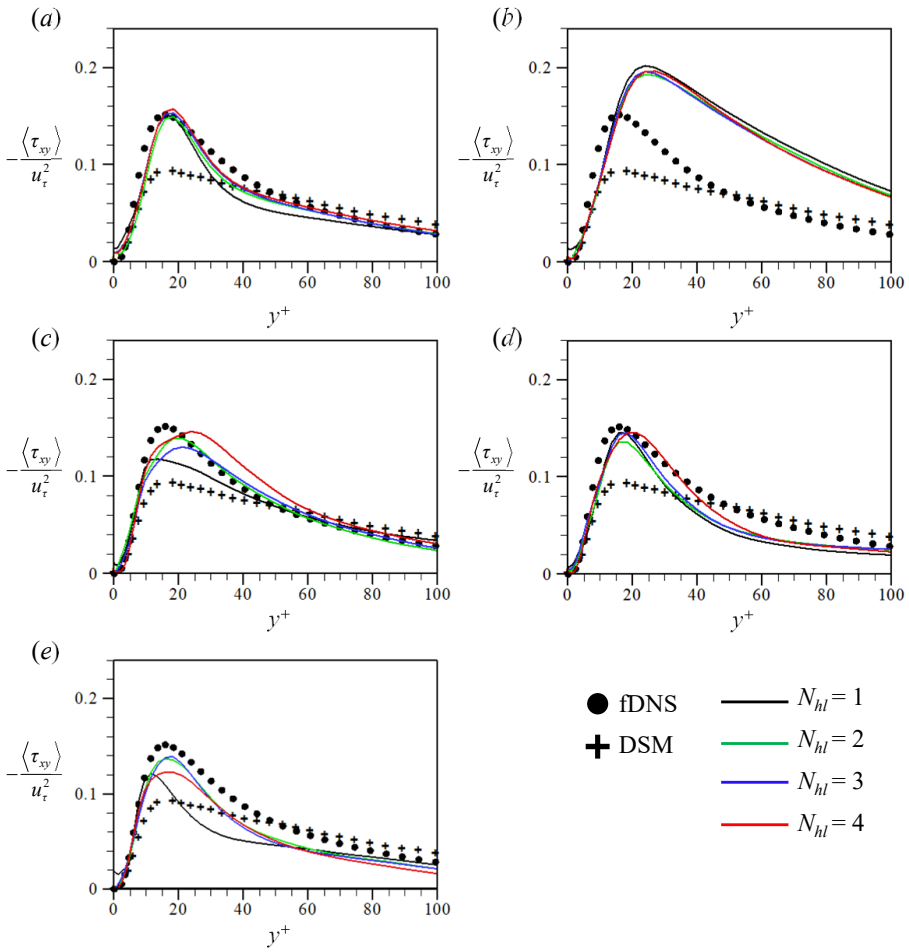

FIGURE A.2. Mean SGS shear stress predicted by NN1 - NN5 with different N_{hl} (*a priori* test at $Re_\tau = 178$): (*a*) NN1; (*b*) NN2; (*c*) NN3; (*d*) NN4; (*e*) NN5.

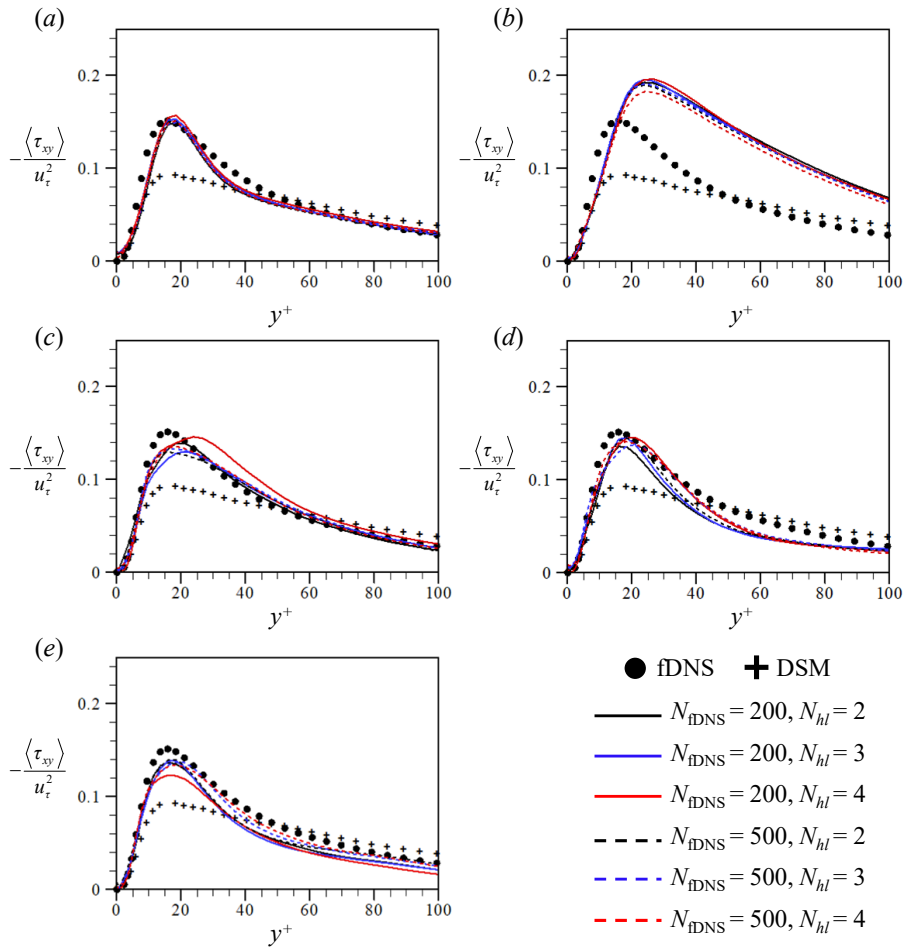

FIGURE A.3. Mean SGS shear stress predicted by NN1 - NN5 with different N_{fDNS} and N_{hl} (*a priori* test at $Re_\tau = 178$): (*a*) NN1; (*b*) NN2; (*c*) NN3; (*d*) NN4; (*e*) NN5.

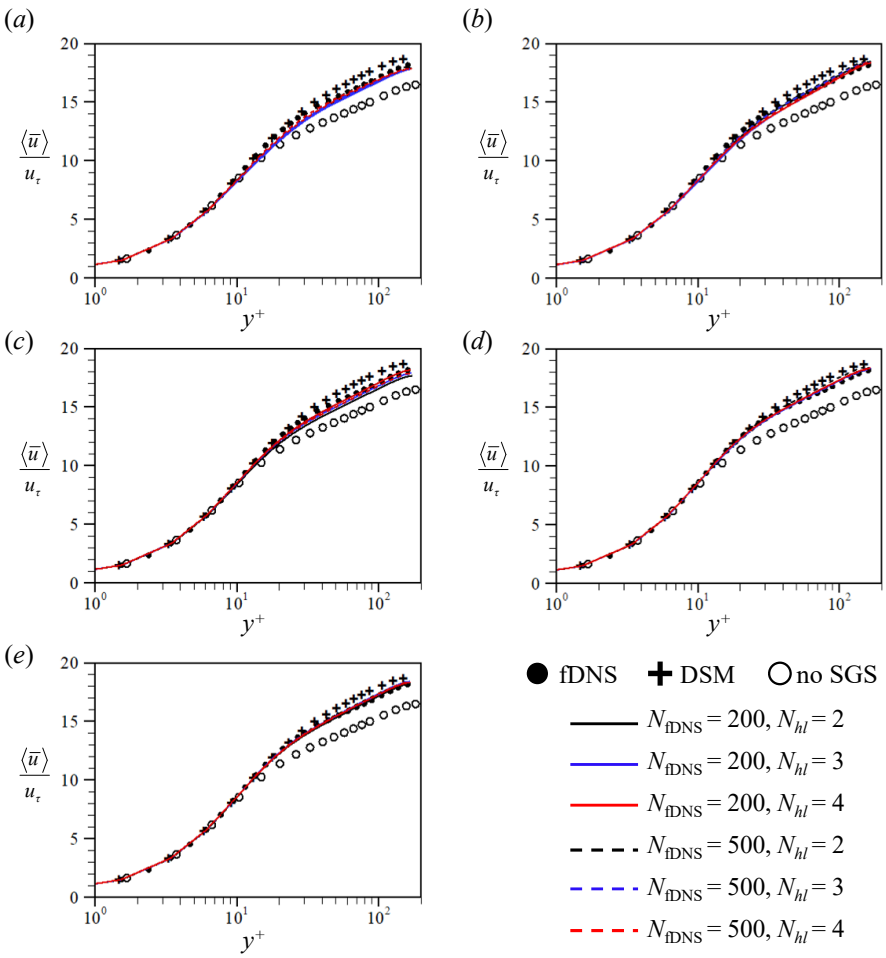

FIGURE A.4. Mean velocity profile from LES at $Re_\tau = 178$ with NN1 - NN5 having different N_{fDNS} and N_{hl}: (*a*) NN1; (*b*) NN2; (*c*) NN3; (*d*) NN4; (*e*) NN5.

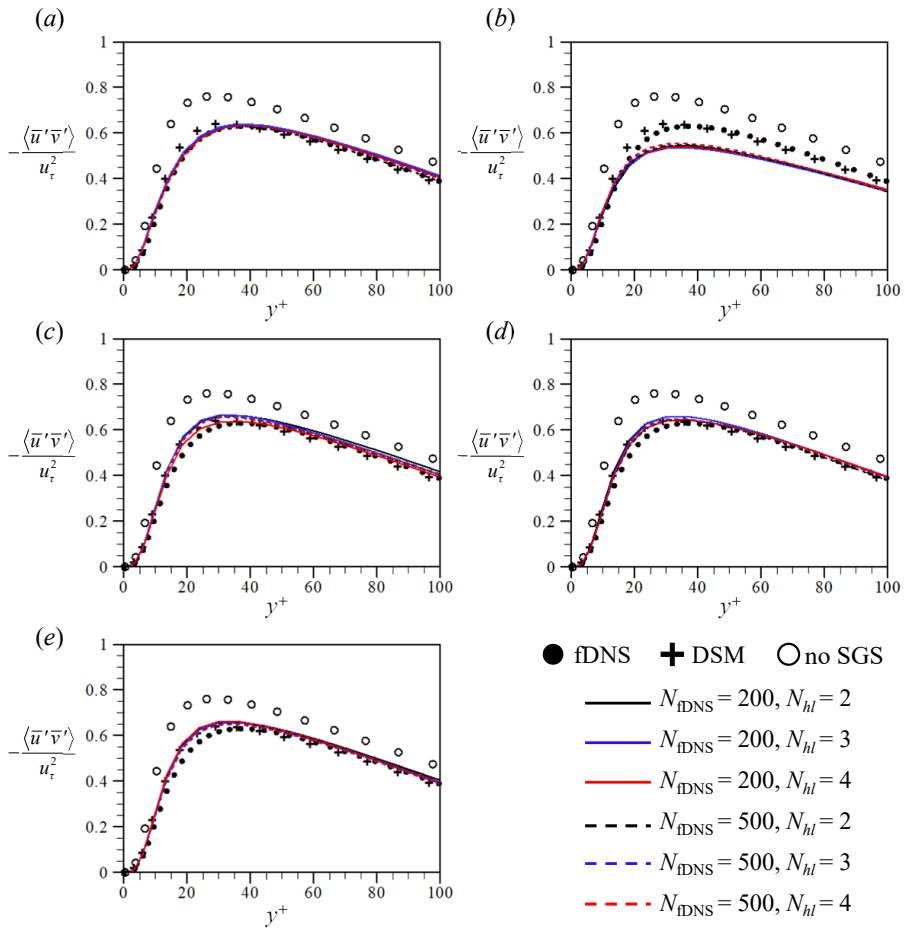

FIGURE A.5. The Reynolds shear stress from LES at $Re_\tau = 178$ with NN1 - NN5 having different N_{fDNS} and N_{hl}: (*a*) NN1; (*b*) NN2; (*c*) NN3; (*d*) NN4; (*e*) NN5.

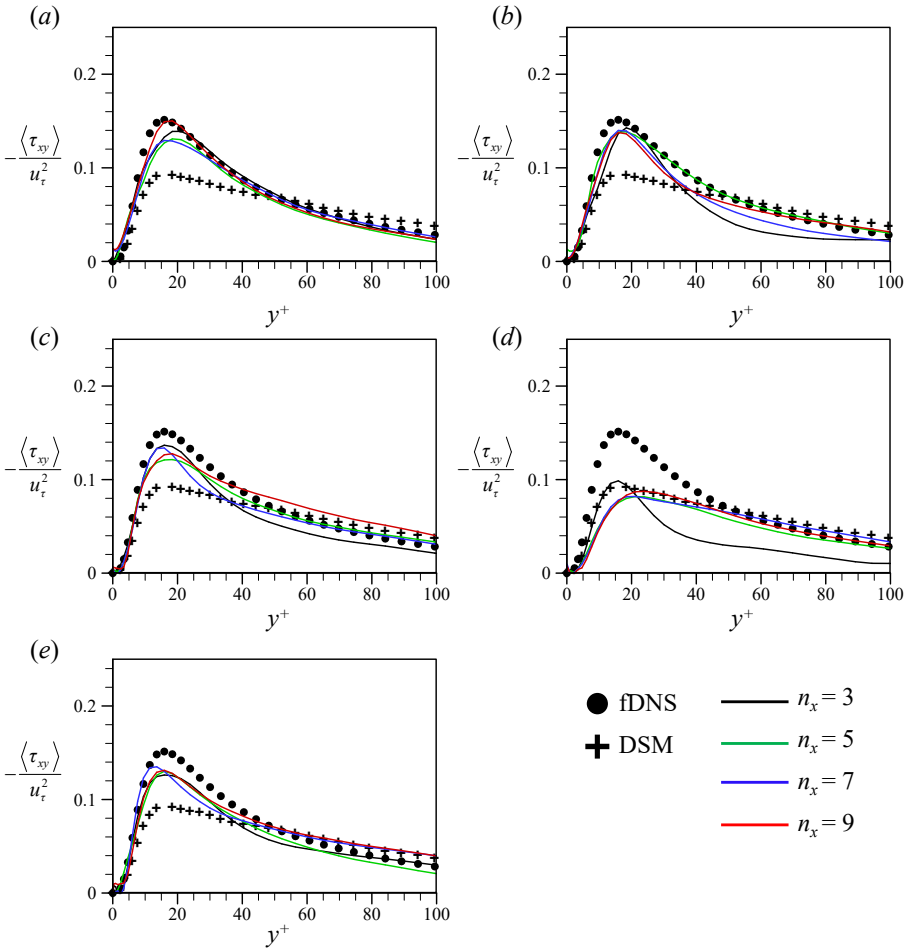

FIGURE A.6. Mean SGS shear stress predicted by NN3 - NN7 with different $n_x (= n_z)$ (*a priori* test at $Re_\tau = 178$): (*a*) NN3; (*b*) NN4; (*c*) NN5; (*d*) NN6; (*e*) NN7.

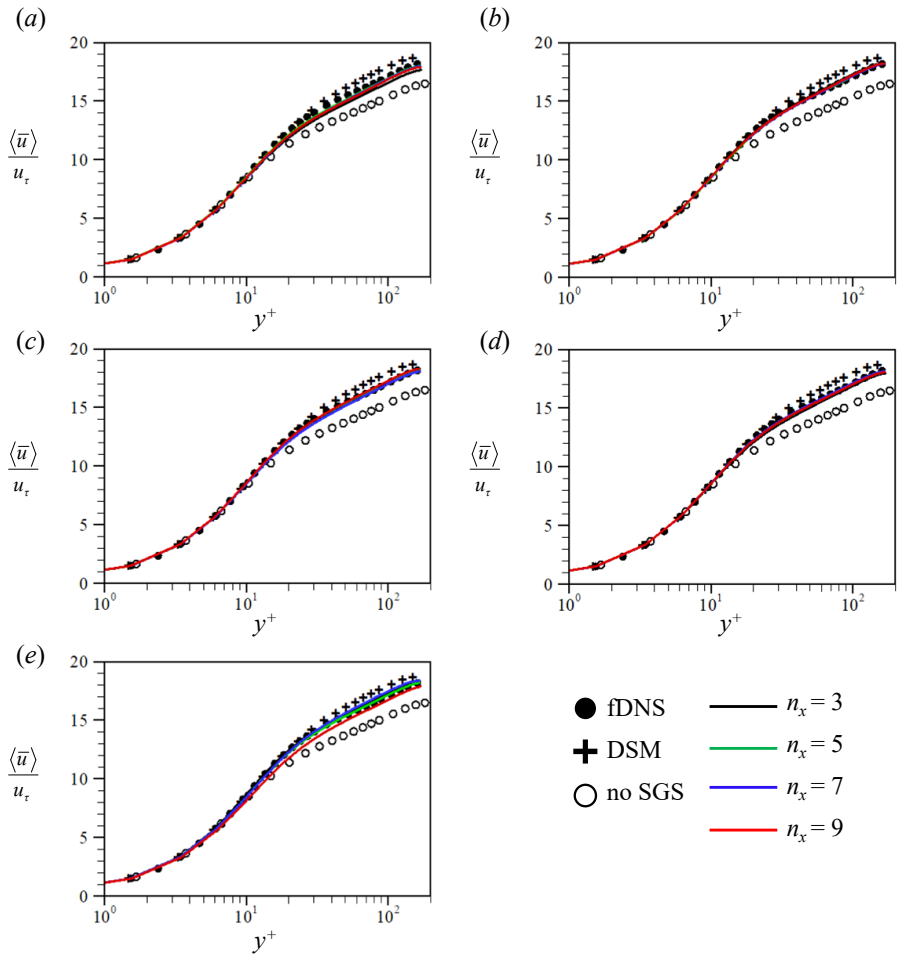

FIGURE A.7. Mean velocity profile from LES at $Re_\tau = 178$ with NN3 - NN7 having different $n_x (= n_z)$: (*a*) NN3; (*b*) NN4; (*c*) NN5; (*d*) NN6; (*e*) NN7.

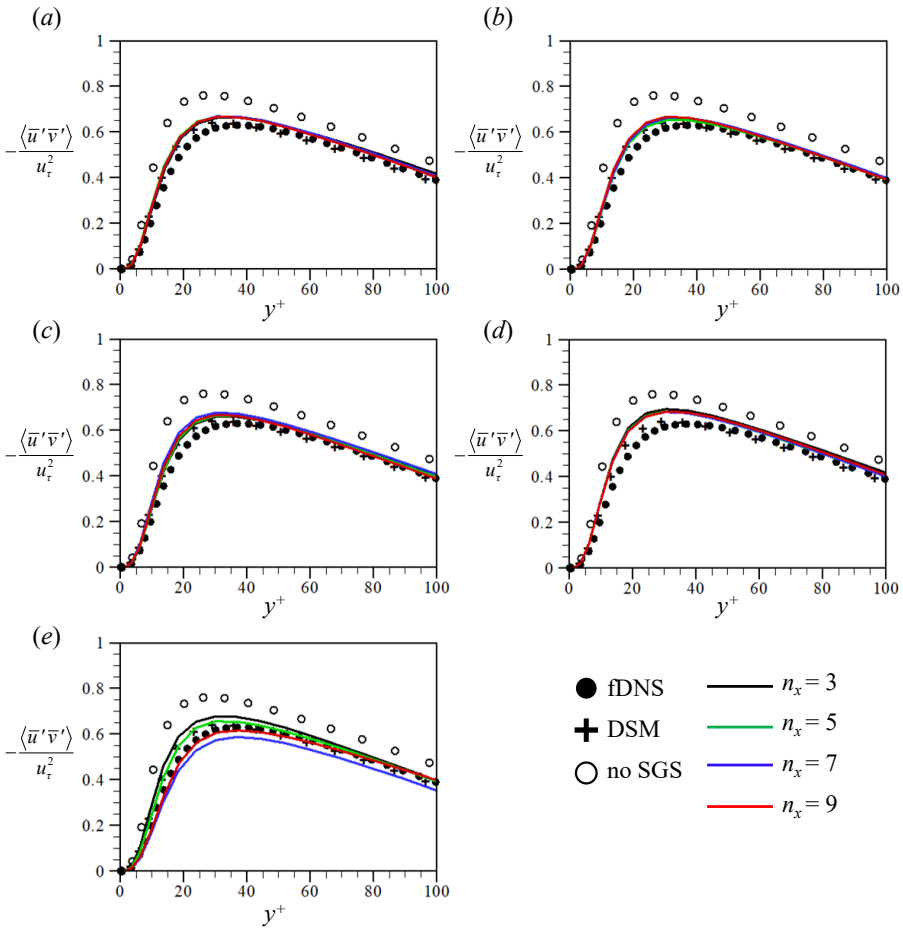

FIGURE A.8. The Reynolds shear stress from LES at $Re_\tau = 178$ with NN3 - NN7 having different $n_x (= n_z)$: (*a*) NN3; (*b*) NN4; (*c*) NN5; (*d*) NN6; (*e*) NN7.

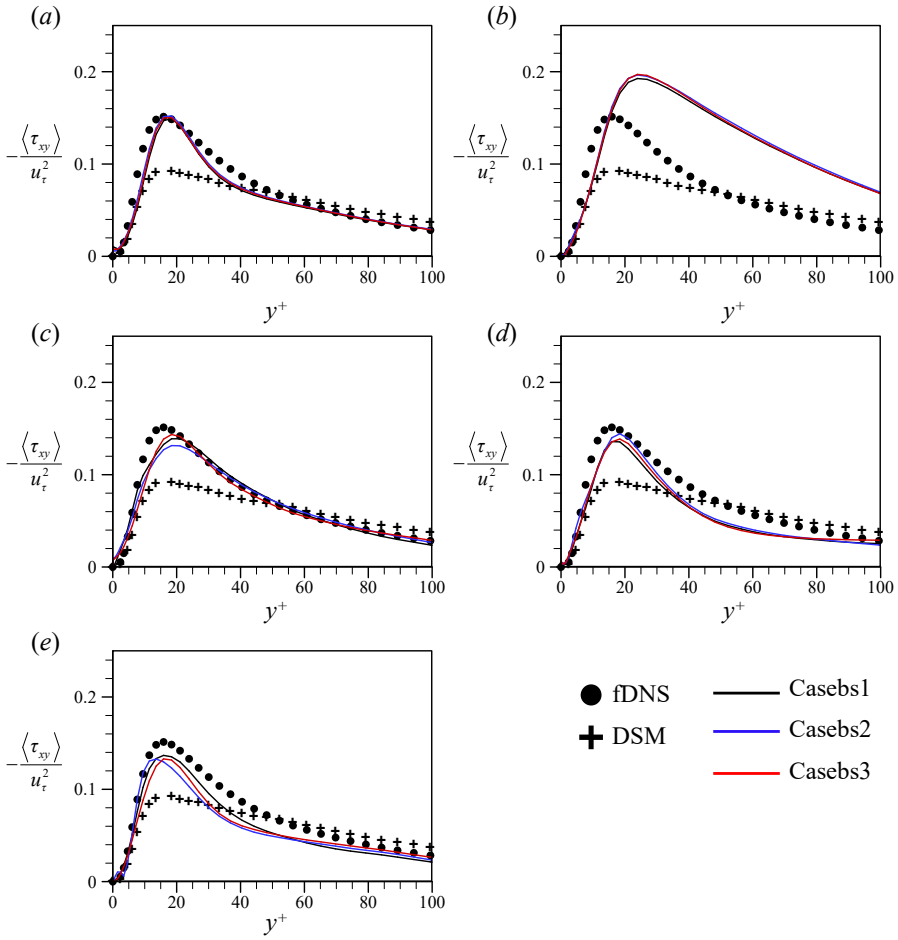

FIGURE A.9. Mean SGS shear stress predicted by NN1 - NN5 with different use of bias (*a priori* test at $Re_\tau = 178$): (*a*) NN1; (*b*) NN2; (*c*) NN3; (*d*) NN4; (*e*) NN5.

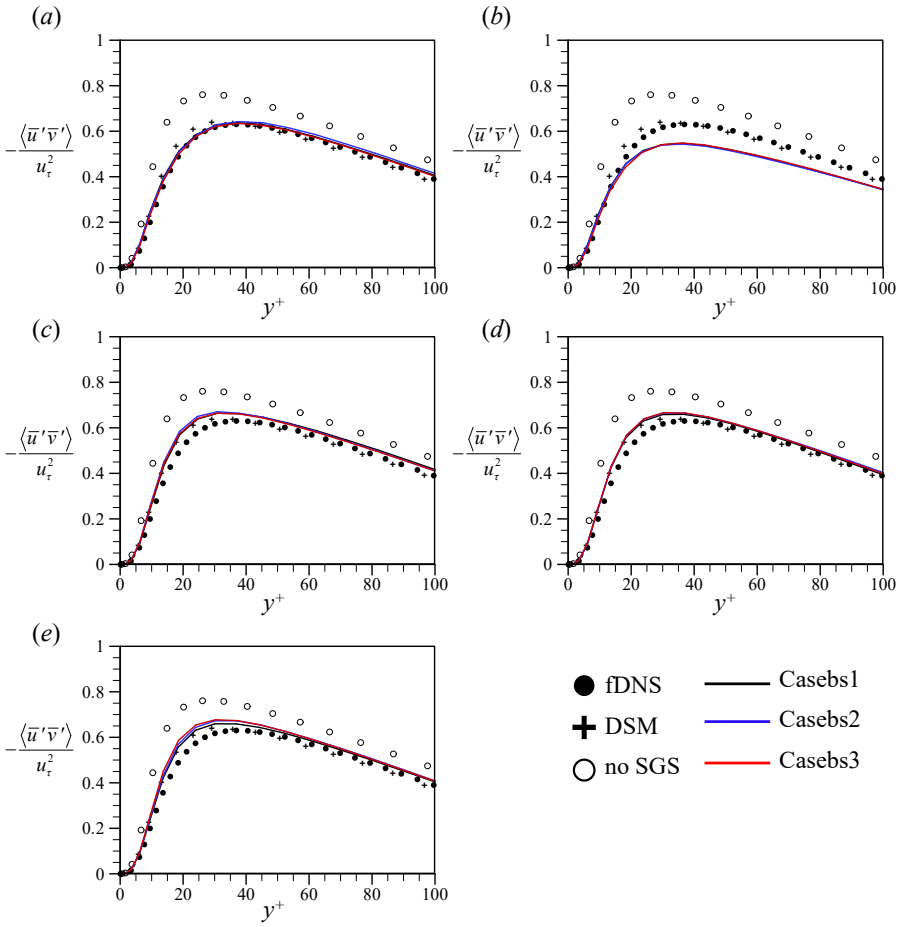

FIGURE A.10. The Reynolds shear stress from LES at $Re_\tau = 178$ with NN1 - NN5 having different usages of bias: (*a*) NN1; (*b*) NN2; (*c*) NN3; (*d*) NN4; (*e*) NN5.

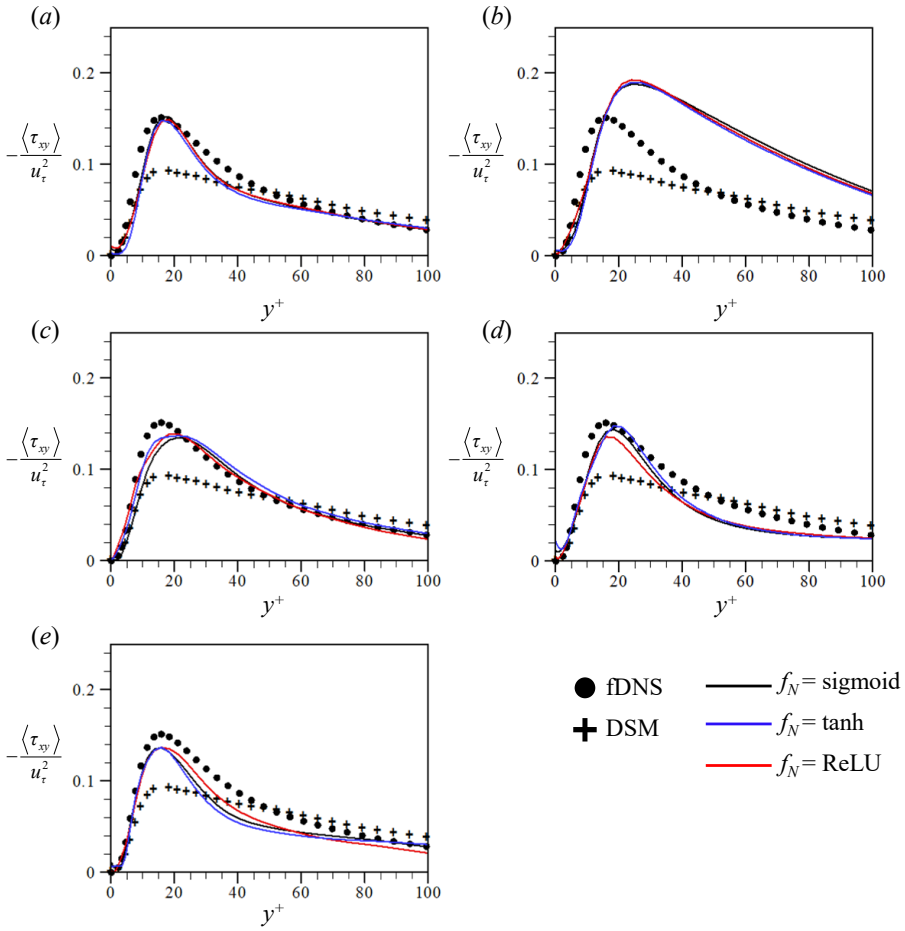

FIGURE A.11. Mean SGS shear stress predicted by NN1 - NN5 with different activation function f_N (*a priori* test at $Re_\tau = 178$): (*a*) NN1; (*b*) NN2; (*c*) NN3; (*d*) NN4; (*e*) NN5.

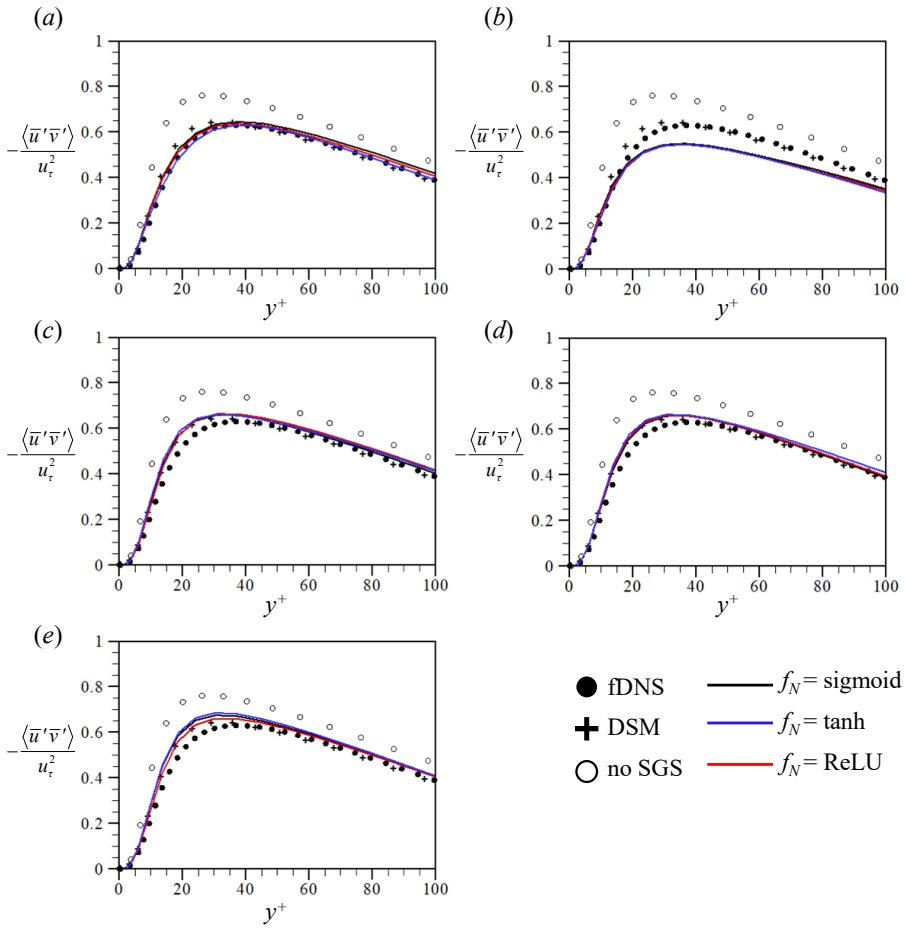

FIGURE A.12. The Reynolds shear stress from LES at $Re_\tau = 178$ with NN1 - NN5 having different activation function: (*a*) NN1; (*b*) NN2; (*c*) NN3; (*d*) NN4; (*e*) NN5.

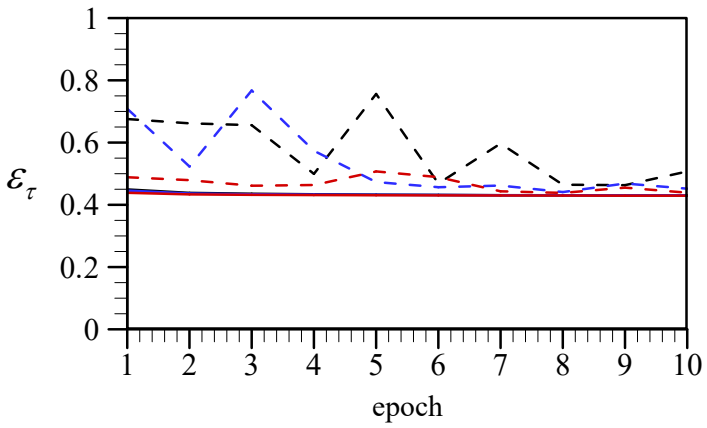

FIGURE A.13. The loss functions for training (solid lines) and test (dashed lines) datasets by different activation functions used in NN1. Black, blue and red lines denote sigmoid, hyperbolic tangent, and ReLU for the activation functions.

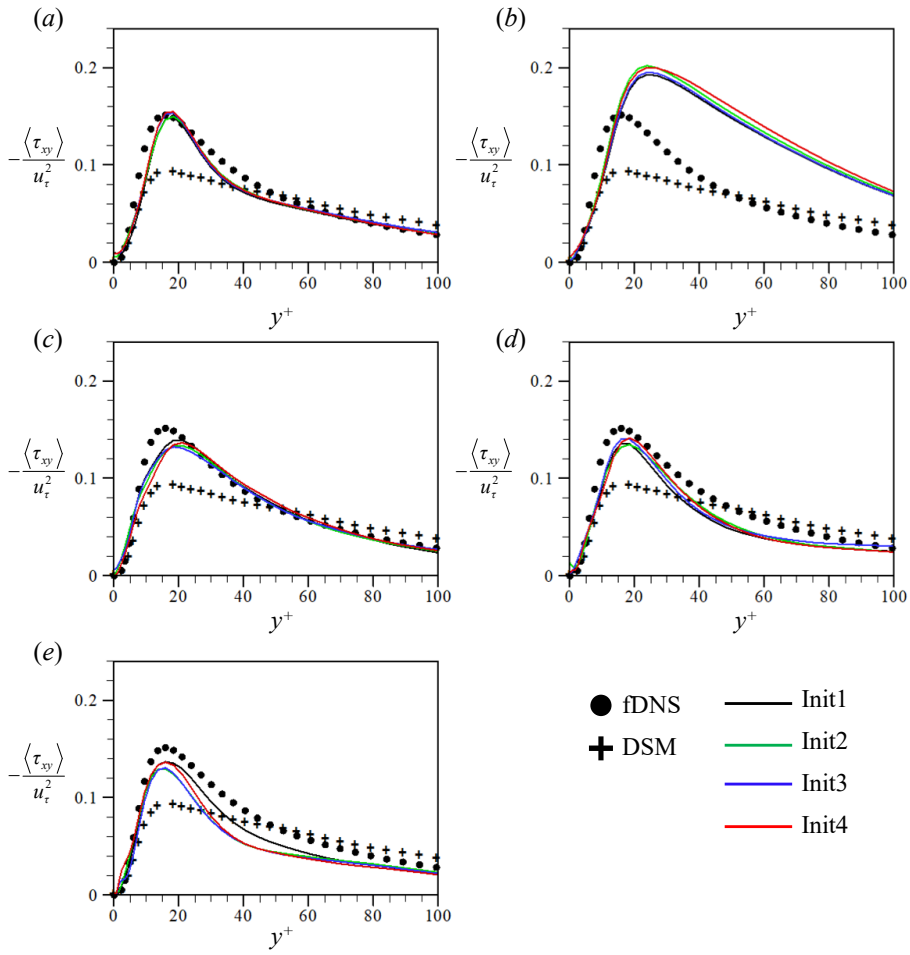

FIGURE A.14. Mean SGS shear stress predicted by NN1 - NN5 with different random seeds for weight initialization (*a priori* test at $Re_\tau = 178$): (*a*) NN1; (*b*) NN2; (*c*) NN3; (*d*) NN4; (*e*) NN5.

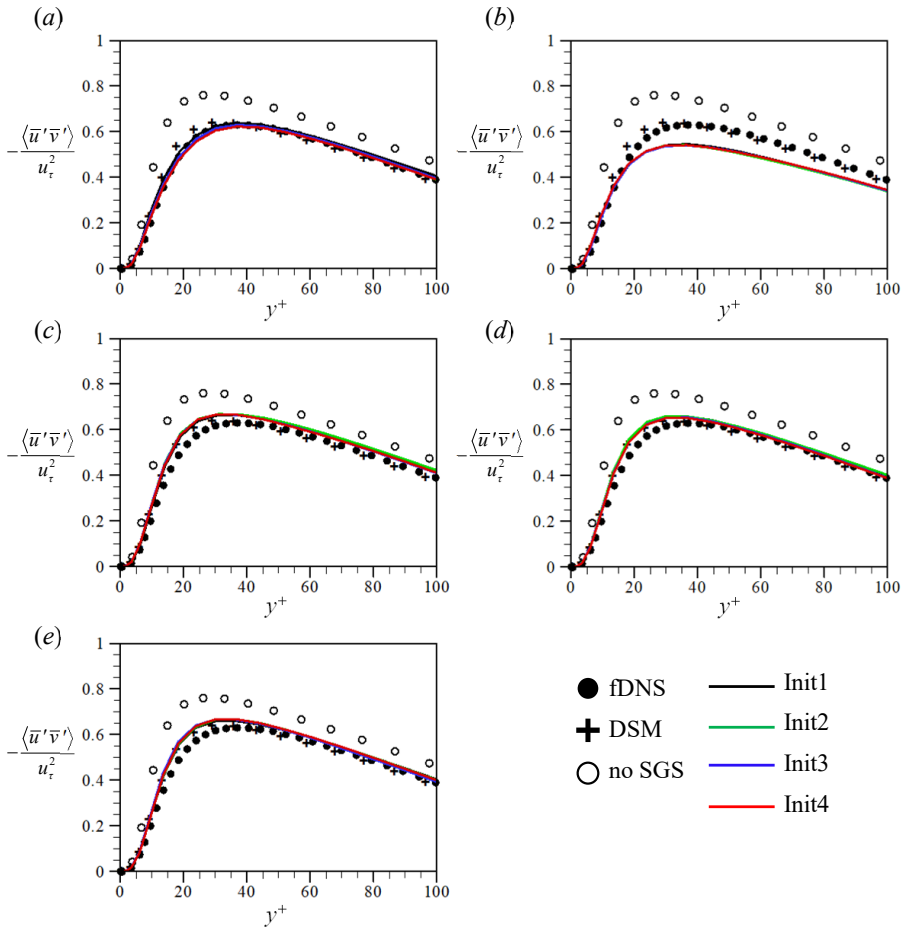

FIGURE A.15. The Reynolds shear stress from LES at $Re_\tau = 178$ with NN1 - NN5 having different random seeds for weight initialization: (*a*) NN1; (*b*) NN2; (*c*) NN3; (*d*) NN4; (*e*) NN5.

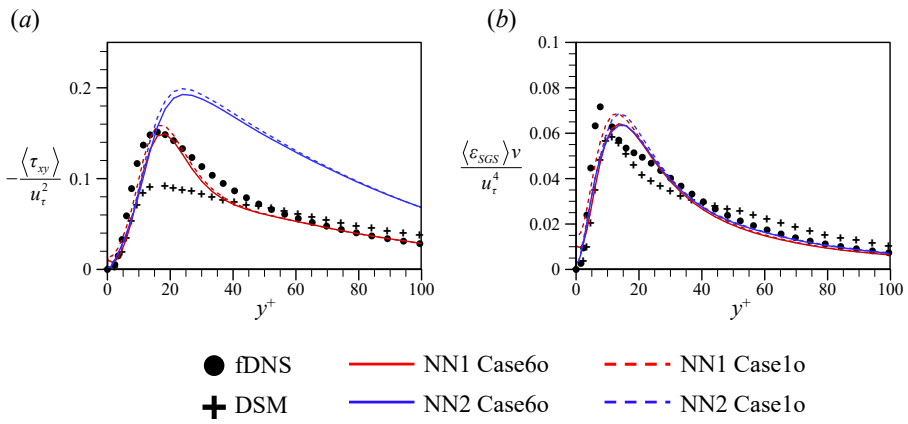

FIGURE A.16. Mean SGS shear stress and dissipation predicted by NN1 and NN2 with different number of output components (*a priori* test at $Re_\tau = 178$)

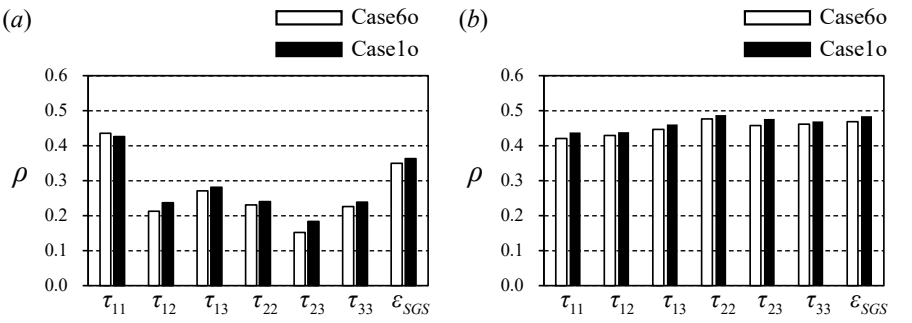

FIGURE A.17. Correlation coefficients between the true and predicted τ_{ij} and ϵ_{SGS}: (*a*) NN1; (*b*) NN2.

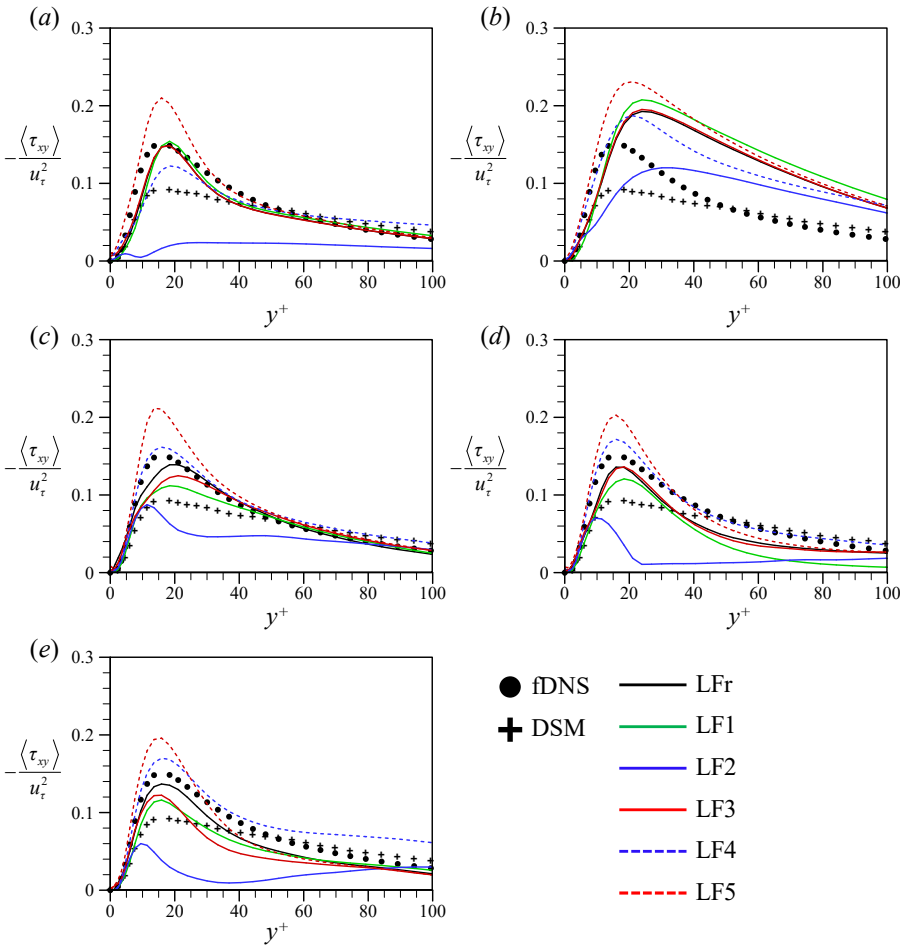

FIGURE A.18. Mean SGS shear stress predicted by NN1 - NN5 with different loss functions (*a priori* test at $Re_\tau = 178$): (*a*) NN1; (*b*) NN2; (*c*) NN3; (*d*) NN4; (*e*) NN5.

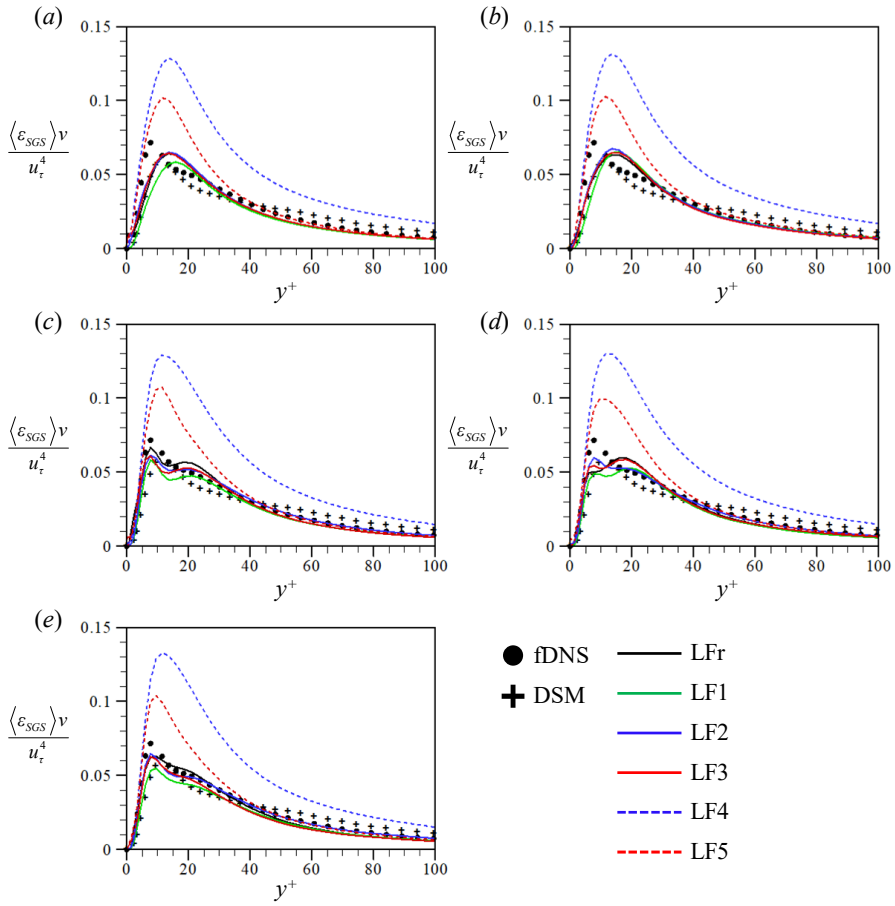

FIGURE A.19. Mean SGS dissipation predicted by NN1 - NN5 with different loss functions (*a priori* test at $Re_\tau = 178$): (*a*) NN1; (*b*) NN2; (*c*) NN3; (*d*) NN4; (*e*) NN5.

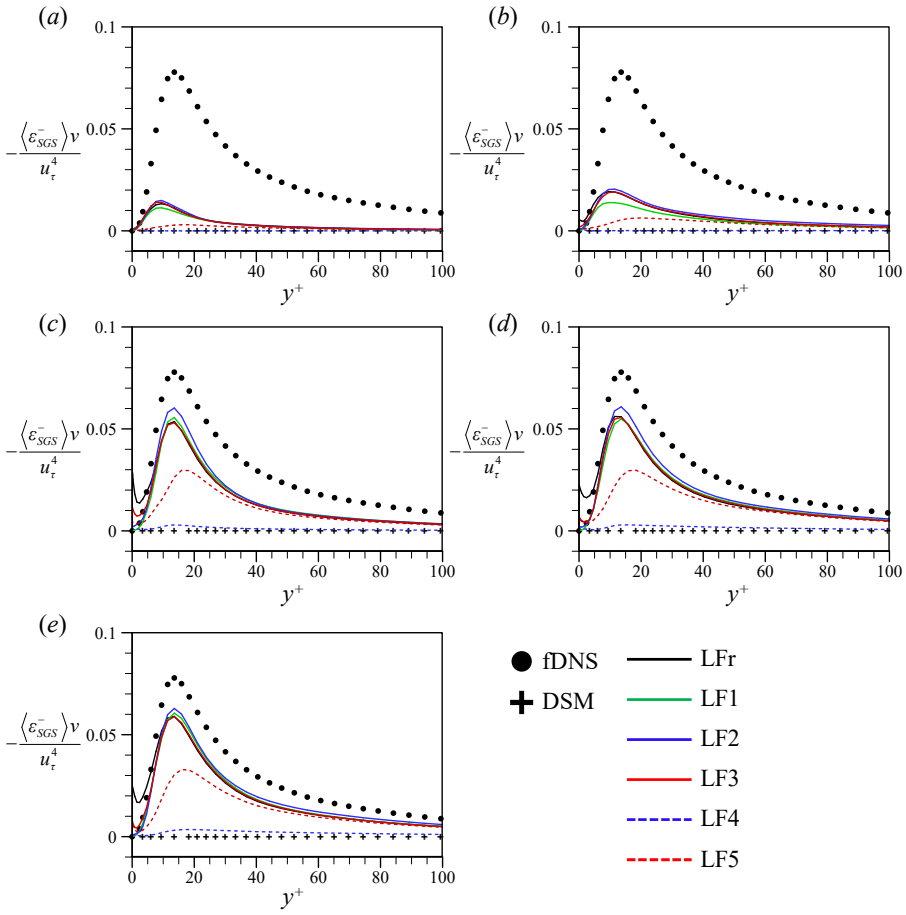

FIGURE A.20. Mean backscatter predicted by NN1 - NN5 with different loss functions (*a priori* test at $Re_\tau = 178$): (*a*) NN1; (*b*) NN2; (*c*) NN3; (*d*) NN4; (*e*) NN5.

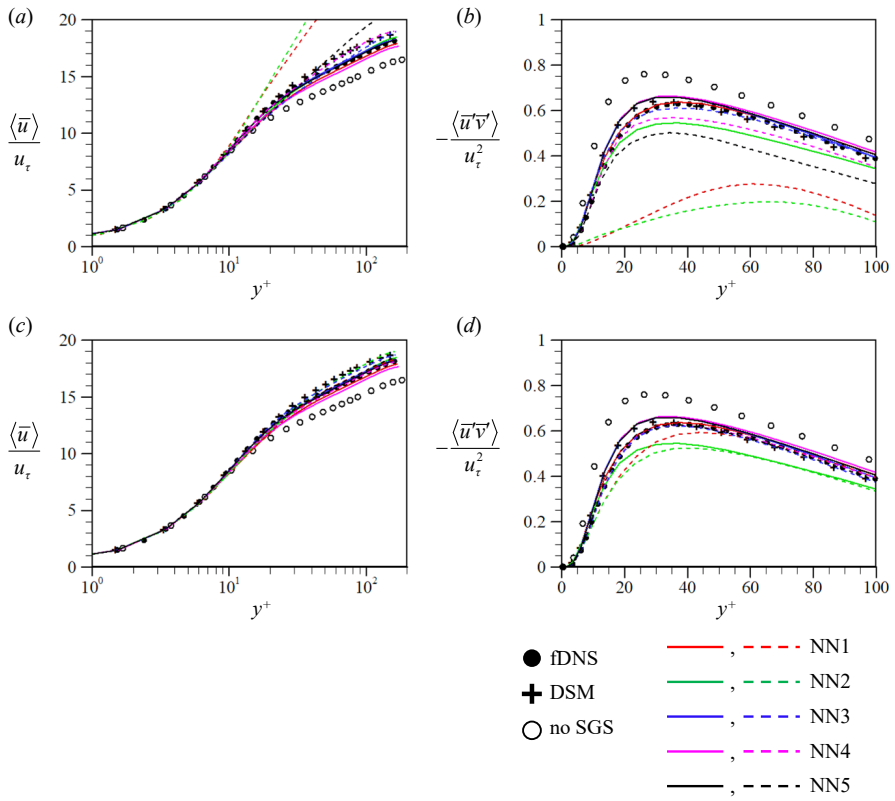

FIGURE A.21. The mean velocity (a, c) and Reynolds shear stress (b, d) from LES at $Re_\tau = 178$ with NN1 - NN5 trained with different loss functions. Solid lines in $(a - d)$ are LFr, dashed lines in (a, b) are LF4, and dashed lines in (c, d) are LF5, respectively.

Appendix B

Normalization method based on a resolved-scale dissipation toward a universal NN-based SGS model

In Part I, we use the wall unit normalization for the input and output variables of the NN in TCF, so this NN cannot be applied to other flows such as homogeneous isotropic turbulence (HIT). Therefore, to overcome this limitation, the normalization (or non-dimensionalization) of input and output variables shall be important, and a universal normalization method should be developed for the general application of an NN-based SGS model to LES of flows different from trained data. In this appendix, a normalization method based on the resolved-scale viscous dissipation is described, and using this normalization, an NN-based SGS model trained with TCF (HIT) database is applied to the LES of HIT (TCF).

Figure B.1 shows the invariants η_b and ξ_b of the Reynolds-stress anisotropy tensor b_{ij}^{Rey} from DNS of TCF at $Re_\tau = 178$ and the SGS-stress anisotropy tensor b_{ij}^{SGS} from fDNS of TCF, together with the Lumley triangle (Pope 2000), where $b_{ij}^{\mathrm{Rey}} = \frac{\langle u_i' u_j' \rangle_{xzt}}{\langle u_k' u_k' \rangle_{xzt}} - \frac{1}{3}\delta_{ij}$, $b_{ij}^{\mathrm{SGS}} = \frac{\langle \tau_{ij} \rangle_{xzt}}{\langle \tau_{kk} \rangle_{xzt}} - \frac{1}{3}\delta_{ij}$. Unless otherwise mentions, the fDNS of TCF are obtained with the same filter sizes as those described in Part I §2.2. The invariants η_b and ξ_b of an anisotropy tensor b_{ij} are defined as $3\eta_b^2 =$

$-\lambda_b^{(1)}\lambda_b^{(2)} - \lambda_b^{(2)}\lambda_b^{(3)} - \lambda_b^{(3)}\lambda_b^{(1)}$, $2\xi_b^3 = \lambda_b^{(1)}\lambda_b^{(2)}\lambda_b^{(3)}$, where $\lambda_b^{(i)}$'s are eigenvalues of tensor b_{ij}. The invariants of isotropic turbulence are $(\eta_b, \xi_b) = (0, 0)$, and further details for the state of turbulence by η_b and ξ_b are described in Pope (2000). Figure B.1 indicates that the state of turbulence near the channel center is close to isotropic for not only b_{ij}^{Rey} but also b_{ij}^{SGS}. This may indicate that an NN trained with TCF database can be applied to LES of HIT with a proper normalization method. On the other hand, an NN trained with HIT database may work for LES of TCF by using a wall-damping function, considering that the Smagorinsky model works well for HIT but the wall-damping function is required for this model in LES of TCF.

For the normalization (non-dimensionalization) method which is applicable to both HIT and TCF flows, the length and velocity scales used in the normalization must be able to be calculated from both HIT and TCF flows. Among various scales for turbulent flows, the Kolmogorov scales represent the smallest turbulent scales, and the Kolmogorov scales can be calculated in any turbulent flow regardless of the geometry around the flow. Inspired by the universality of the Kolmogorov scales, but using only information of the resolved flow in LES, a resolved-dissipation length and velocity scales, l_{rd} and u_{rd}, respectively, are defined as follows: $l_{\mathrm{rd}} = \left(\nu^3/\bar{\varepsilon}\right)^{0.25}$, $u_{\mathrm{rd}} = (\nu\bar{\varepsilon})^{0.25}$, ν is kinematic viscosity, and $\bar{\varepsilon} = 2\nu\langle\bar{S}'_{ij}\bar{S}'_{ij}\rangle$. These definitions are similar to those of the Kolmogorov length and velocity scales, but unlike the Kolmogorov scales, the filtered strain rate fluctuation $\bar{S}'_{ij}$ is used to represent the dissipation of the resolved flows.

Figure B.2 shows l_{rd} and u_{rd} from DNS and fDNS of TCF, normalized by characteristics grid size Δ_c and resolved turbulent kinetic energy k_e, respectively, where $\Delta_c = (\Delta x \Delta y \Delta z)^{1/3}$ and $k_e = 1/3(\bar{u}_{rms} + \bar{v}_{rms} + \bar{w}_{rms})$. Note that l_{rd} and u_{rd} of DNS are the same as Kolmogorov length and velocity scales. The $l_{\mathrm{rd}}/\Delta_{\mathrm{HIT}}$ and $u_{\mathrm{rd}}/\sqrt{k_e}$ from DNS of forced HIT at the Reynolds number of

$Re_\lambda = u'\lambda/\nu = 73$ are about 0.48 and 0.19, respectively, where 128^3 grid points are used for the DNS, u' is the rms velocity fluctuation, λ is the Taylor micro scale, and Δ_{HIT} is the grid size of the DNS. Computational details for the DNS of HIT is given in appendix C. In the case of fDNS of HIT, $\left(l_{\mathrm{rd}}/\Delta_{\mathrm{HIT}}, u_{\mathrm{rd}}/\sqrt{k_e}\right) = (0.13, 0.17),\ (0.11, 0.18),\ (0.08, 0.18)$ for the fDNS with grid points of 32^3, 24^3, 16^3, respectively, where the spectral cutoff filter is applied to DNS flow fields to obtain fDNS. Although l_{rd} and u_{rd} are varied in wall-normal direction in TCF, their order of magnitude are similar to those in HIT for both DNS and fDNS considered.

We first apply an NN trained with fDNS of TCF to LES of forced HIT whose grid points are 24^3 or 32^3. The NN has the input of filtered strain rate tensor at a single grid point, and the output is six components of SGS stress tensor. All flow variables used for training this NN are non-dimensionalized by l_{rd} and u_{rd} obtained from fDNS of TCF. During LES of HIT, the input and output of this NN are re-normalized using l_{rd} and u_{rd} from fDNS of HIT having the same grid points as those of LES. Figure B.3 shows the three-dimensional energy spectrum from LES of HIT. For the LES, we do not use any special treatment such as backscatter clipping. The NN model trained with fDNS of TCF shows good prediction for the energy spectrum, indicating that the normalization based on l_{rd} and u_{rd} works well.

Then, we test an NN trained with fDNS of HIT in LES of TCF whose grid points are $16(x) \times 49(y) \times 16(z)$. The NN has the input of filtered strain rate tensor at a single grid point, and the output is six components of SGS stress tensor. We apply two NNs to the LES of TCF, where one is trained with TCF flow using wall unit normalization, and the other is trained with HIT flow using the normalization based on l_{rd} and u_{rd}. The former NN (TCFNN hereafter) is the same NN1 in Part I. For the latter NN (HITNN hereafter), the input and output

variables are re-normalized using l_{rd} and u_{rd} from fDNS of TCF, and the wall damping function of $1 - \exp^{-(y^+/25)^3}$ is multipled to the predicted SGS stress by the NN. Figure B.4 shows the statistics of various turbulence quantities from LES of TCF with TCFNN and HITNN. The LES with HITNN shows an excellent prediction for the mean velocity, and good predictions for the turbulence statistics. For the mean SGS shear stress, the HITNN underpredict it ,but the y^+ location of its maximum value is captured. Therefore, the NN model trained with fDNS of HIT can be applied to the TCF with the normalization based on l_{rd} and u_{rd}, showing fairly successful predictions for the mean velocity and turbulence statistics. The present results suggest that a general normalization of flow variables for different types of turbulent flow may be possible, and this important subject should be further investigated in the near future.

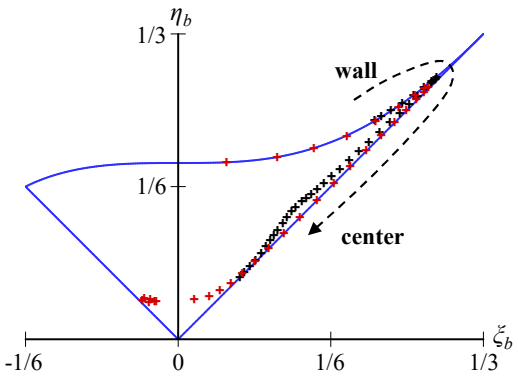

FIGURE B.1. The invariants η and ξ of the Reynolds-stress and SGS-stress anisotropy tensors from DNS and fDNS of TCF at $Re_\tau = 178$. —, Lumley triangle; +, b_{ij}^{Rey} from DNS; +, b_{ij}^{SGS} from fDNS.

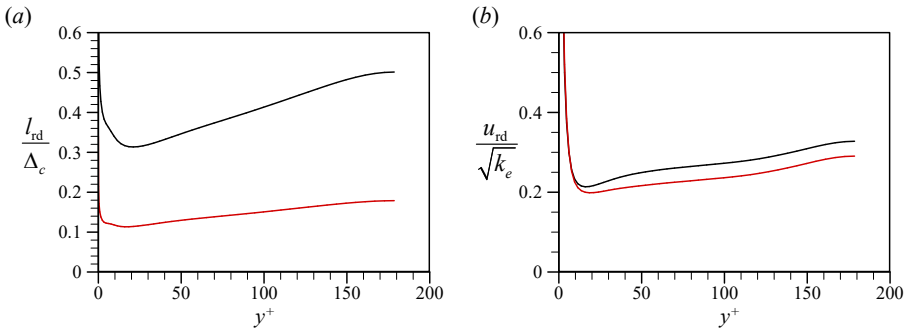

FIGURE B.2. The resolved-dissipation length and velocity scales of TCF at $Re_\tau = 178$: (*a*) l_{rd}; (*b*) u_{rd}. —, DNS; —, fDNS. The u_{rd} at $y^+ = 0$ is approximately 20 for both DNS and fDNS.

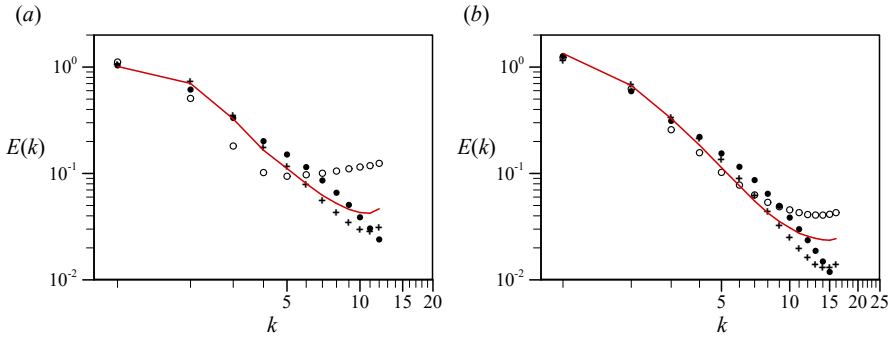

FIGURE B.3. Three-dimensional energy spectrum from LES of HIT at $Re_\lambda = 73$: (*a*) 24^3 resolution; (*b*) 32^3 resolution. ●, fDNS; +, DSM; ○, no SGS model; —, NN model trained with TCF.

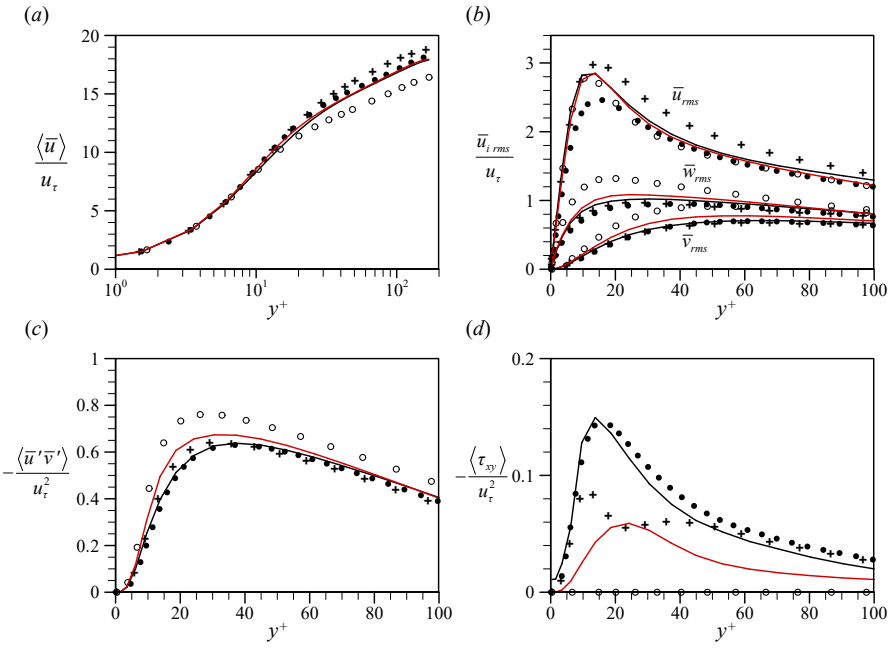

FIGURE B.4. Turbulence statistics from LES178 (*a posteriori* test): (*a*) mean velocity; (*b*) rms velocity fluctuations; (*c*) Reynolds shear stress; (*d*) mean SGS shear stress. ●, fDNS; +, DSM; ○, no SGS model; —, TCFNN; —, HITNN.

Appendix C

Computational details for DNS of a forced homogeneous isotropic turbulence

DNS database of a forced homogeneous isotropic turbulence (HIT) is required to train an NN in appendix B, so we performance DNS of HIT using the dealiased pseudo-spectral method. The numbers of grid points used are 128^3 on a periodic box whose sizes are $\left(2\pi L_{ref}\right)^3$. The spatial resolution parameter $k_{max}\eta$ is 1.5 which is good resolution for the smallest scales (Pope 2000), where k_{max} is the maximum wavenumber and η is the Kolmogorov length scale. For the time integration, third-order Runge-Kutta and second-order Crank-Nicolson schemes are applied to the convection and viscous terms, respectively. The simulation starts with a random-phase Gaussian field that satisfies the $k^{-5/3}$ energy spectrum. The large-scale forcing f_i at a low wavenumber ($k \leq 2$) is added to the momentum equations to retain statistically stationary HIT. The f_i is defined as

$$\hat{f}_i(k) = \varepsilon_f \frac{\hat{u}_i(k)}{\sum_{k\leq 2} \left|\hat{u}_i(k)\right|^2}, \tag{C.1}$$

where $\hat{x}$ is a Fourier coefficient of a physical variable x, and ε_f is the prescribed dissipation rate. The Reynolds number $Re_\lambda = u'\lambda/\nu$ is approximately 73, where

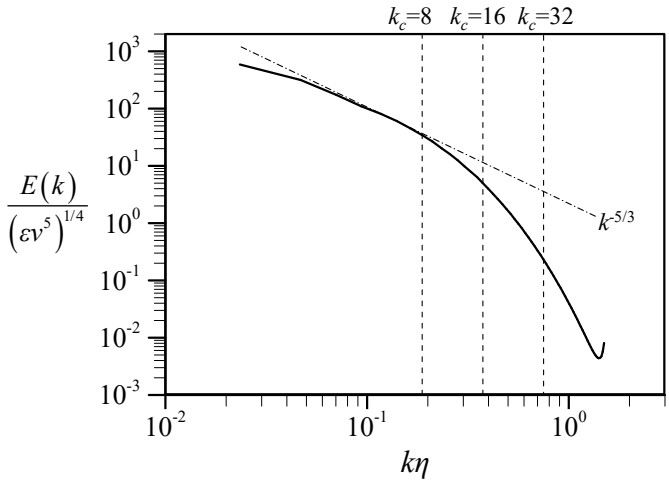

FIGURE C.1. Three dimensional energy spectrum from DNS of a forced HIT (solid line). Vertical dashed lines indicate cutoff wavenumbers for filtering.

u' is the rms velocity fluctuation, λ is the Taylor micro scale. The integral length scale L_I is $1.02L_{ref}$ and u' is $1.24u_{ref}$. The Taylor micro and Kolmogorov scales are $\lambda = 0.39L_{ref}$ and $\eta = 0.02L_{ref}$, respectively. The dissipation rate ε_f is set to 1 non-dimensionalized by L_{ref} and u_{ref}.

Figure C.1 shows energy spectrum normalized by the Kolmogorov scales, together with three cutoff wavenumbers k_c normalized by L_{ref}. The $k_c = 32$ is within the dissipation range, so LES with this cutoff wavenumber is a well-resolved LES. Since LES with coarse grid resolution shows the performance of the SGS model more clearly than LES with fine grid resolution, we preform LES of HIT with maximum wavenumber smaller than $k_c = 32$ in appendix B.

Appendix D

SGS stress from NN model in laminar shear flow

The SGS stress is theoretically zero in laminar shear flow. To investigate whether the NN-based SGS model provides zero SGS stress in laminar shear flow or not, we conduct a numerical experiment using a prescribed velocity profile. The experiment is conducted with the NN model trained with BFS flow at $Re_h = 5100$, where the input is the strain-rate tensor (see Part II §2.3 for details about this NN model). The velocity profile used is the mean streamwise velocity profile at the inlet of BFS flow at $Re_h = 5100$, and the wall-normal and spanwise velocities are zero. Figure D.1(a) shows the prescribed velocity profile, and figures D.1(b) shows the SGS shear stresses predicted by DSM, CSM, and NN model, where CSM is the Smagorinsky model with $C_s = 0.1$. The SGS shear stress is exactly zero from DSM along y direction, whereas the stress does not vanish with CSM. The SGS shear stress from NN model is close to zero, but the stress is not exactly zero, as shown in figure D.1(c). This is one of the limitations of NN model to be overcome, and special treatments should be developed so that the SGS stresses are predicted to be exactly zero for certain input variables such as laminar shear flow.

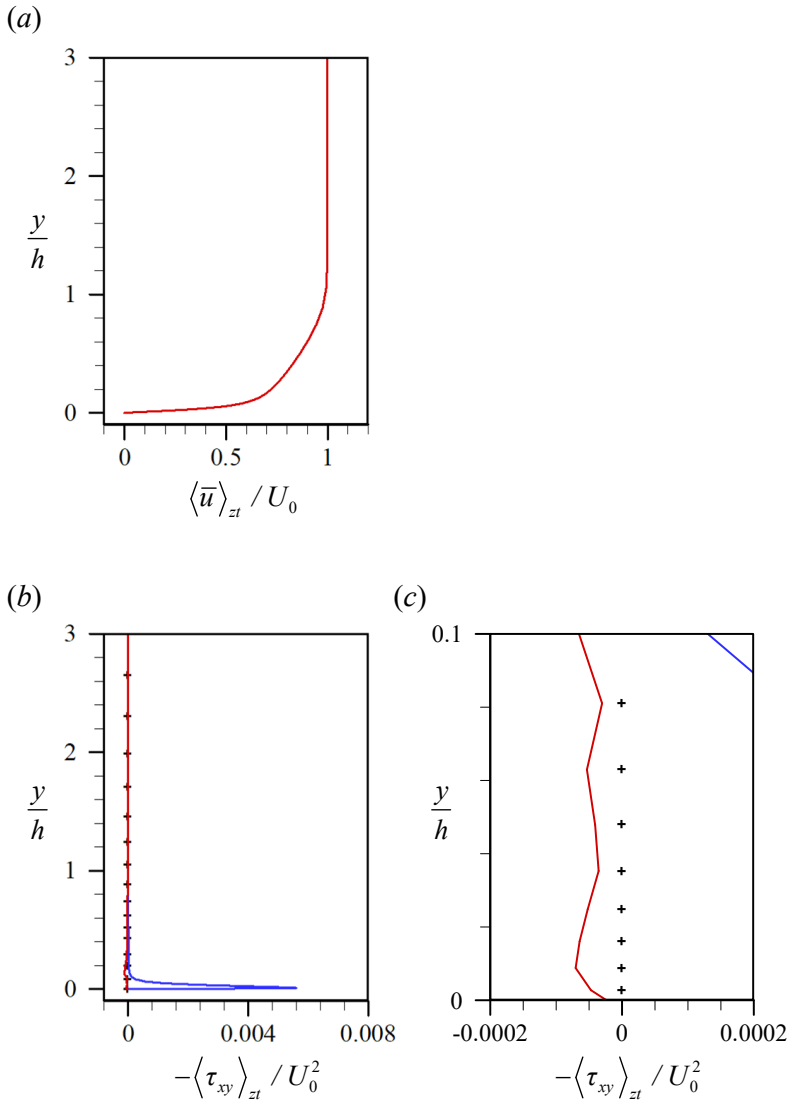

FIGURE D.1. Numerical experiment with prescribed velocity: (*a*) velocity profile; (*b*, *c*) SGS shear stresses predicted by DSM (+), CSM (—), NN (—).

인공신경망을 이용한 아격자스케일 응력 모델링과 난류 채널 및 후향 계단 유동에의 적용

서울대학교 대학원
기계항공공학부
박 종 환

요 약

본 연구에서는 난류 채널 유동과 후향 계단 주위 난류 유동에 대해, 필터링 된 유동변수를 입력변수로 하여 아격자스케일 (subgrid scale, SGS) 응력을 예측하는 인공신경망 기반 SGS 모델을 개발하였다.

난류 채널 유동의 경우, 필터링 된 직접수치모사 데이터베이스($Re_\tau = 178$)를 사용하여 인공신경망 기반 SGS 모델을 개발하고, 본 모델의 성능을 평가하기 위해 사전 및 사후 테스트를 수행하였다. 사전 테스트에서, 여러 격자점에 있는 필터링 된 속도기울기 또는 속도변형률 텐서를 입력변수로 하는 인공신경망 모델은 실제 SGS 응력과 높은 상관계수를 보이는 SGS 응력을 예측하였다. 그러나 이 모델은 사후 테스트에서 불안정한 수치계산 결과를 보여주었고, LES 솔루션을 얻기 위해서는 후방 산란(backscatter)을 강제적으로 없애는 등의 임의적인 처리를 필요로 했다. 반면, 단일 격자점에서의 필터링 된 속도변형률 텐서를 입력변수로 한 인공신경망 모델은, 사전 테스트에서 실제값과 낮은 상관계수를 보이는 SGS 응력을 예측하였으나, 사후 테스트에서 평균 속도 프로파일과 Reynolds 전

단 응력에 대해 우수한 예측 성능을 보였다. 더 높은 Reynolds 수에서 인공신경망 모델의 성능을 확인하기 위하여, $Re_\tau = 178$에서 훈련된 인공신경망 기반 SGS 모델(입력변수: 단일 격자점의 필터링 된 속도변형률 텐서)을, $Re_\tau = 723$의 큰 에디 모사에 적용하였다. 벽 단위 격자 크기를 학습데이터의 것과 같도록 설정한 경우, 인공신경망 모델의 큰 에디 모사는 필터링 된 직접수치모사의 솔루션과 상당히 잘 일치하였다. 한편, 벽 단위 격자 크기가 훈련데이터의 것과 다른 경우, 인공신경망 모델의 성능이 저하되었으나, 큰 에디 모사의 격자 크기보다 격자 크기가 큰 그리고 작은 학습데이터를 한꺼번에 인공신경망 학습에 사용하게 되면 좋은 성능을 보여주었다.

후향 계단 주위 난류 유동의 경우, $Re_h = 5100$의 필터링 된 직접수치모사 데이터베이스를 사용하여 인공신경망 기반 SGS 모델을 개발하였다. 인공신경망의 입력변수로는, 난류 채널 유동의 큰 에디 모사에서 안정적이고 좋은 성능을 보여준, 단일 격자점의 필터링 된 속도기울기 그리고 속도변형률을 각각 시험해 보았다. $Re_h = 5100$에서 큰 에디 모사를 수행한 결과, 두 개의 입력변수로 각각 학습된 인공신경망 모델 모두 재부착 길이 및 난류 섭동량에 대해서, 가장 널리 사용되는 동적 Smagorinksy 모델(DSM)과 비교하여 좋은 예측 성능을 보였다. 속도변형률을 입력변수로 하는 인공신경망 모델을 $Re_h = 24000$의 큰 에디 모사에 적용한 결과, DSM을 사용한 큰 에디 모사와 비교하여 여전히 좋은 결과를 보여주었다. 마지막으로, 후향 계단 모서리에 탭이 설치된 유동에 대한 큰 에디 모사를 수행하였다. 그 결과, SGS 모델을 사용하지 않은 경우에는, 평균속도와 난류섭동량에 대해 기존 실험결과 및 DSM을 사용한 LES와 매우 큰 차이를 보였으나, 인공신경망 모델은 DSM과 유사한 유동예측 성능을 보여주었으며, 재부착 길이 감소량의 경우, 인공신경망 모델이 DSM보다 실험값과 더 잘 일치하였다.

주요어: 큰 에디 모사, 아격자스케일 모델링, 기계학습, 머신러닝, 인공신경망, 난류 채널 유동, 후향 계단 유동

학 번: 2015-20699